POLITECNICO DI MILANO
INDUSTRIAL ENGINEERING FACULTY

MASTER'S DEGREE IN SPACE ENGINEERING

Large Space Structures Dynamics in a Multi-Body Gravitational Environment

Advisor:
Prof. Michèle LAVAGNA

Co-advisors:
Prof. Kathleen C. HOWELL
Prof. Lorenzo CASALINO

Graduation Thesis of:
Davide GUZZETTI
751069

ACADEMIC YEAR 2011-2012

To my parents and my brother Dario.

Sommario

Il futuro dell'esplorazione spaziale è legato alla capacità di collocare grandi strutture spaziali in punti strategici del campo gravitazionale in sistemi multi-corpo. In questa tesi viene sviluppato e studiato il modello dinamico del problema circolare ristretto dei tre corpi, includendo le peculiarità di queste architetture: estesa distribuzione di massa, grandi superfici esposte alla radiazione solare, maggior livello di flessibilità. In particolare, l'analisi è ristretta nel piano orbitale dei due attrattori, lungo le orbite di Lyapunov. Innanzitutto, si è sviluppato un accurato modello che includesse l'accoppiamento tra la meccanica orbitale e quella di assetto, attraverso l'azione del gradiente di gravità sulla distribuzione di massa. Ne compare un quadro nuovo e inatteso della dinamica, che offre svariati spunti per un più efficace progetto delle grandi strutture spaziali destinate ad uno scenario gravitazionale multi-corpo. Successivamente, la perturbazione ambientale dominante nelle regioni di interesse, ovvero la pressione di radiazione solare, è incorporata nella formulazione del moto. Si dimostra che è possibile ammaestrare la dinamica accoppiata per avanzare astute strategie di missione. I benefici di queste soluzioni sono chiaramente mostrati, senza tralasciare di verificarne la robustezza rispetto alle variabili di progetto. In questo contesto è stato anche identificato un disturbo esterno particolarmente critico, che sarà battezzato anomalia del secondario. Infine, anche la dinamica elastica della struttura è aggiunta alle equazioni di moto. Dopo un prima discussione degli effetti nell'ambito di un problema multi-corpo, l'analisi della dinamica naturale suggerisce nuove possibilità di controllo e manovra di architetture distribuite attraverso variazioni di geometria della configurazione stessa.

Parole Chiave: Grandi Strutture Spaziali, Problema Ristretto dei Tre Corpi, Dinamica Accoppiata, Pressione di Radiazione Solare, Strutture Spaziali Flessibili.

Abstract

The ability to place large space structures in strategic points of the gravitational field of multi-body systems represents the future of space exploration. In the present thesis, a dynamical model of the circular restricted three body problem is developed to include the special features of these architectures: an extended mass distribution, a larger surface exposed to solar radiation, a higher level of flexibility. In particular, the analysis is restricted to the orbital plan of the two attractors along Lyapunov periodic orbits. Firstly, an accurate model is developed by the inclusion of the action exerted by the gravity gradient over the mass distribution. A novel and unexpected portrait of the dynamics appears, which offers several suggestions for a more effective design of large space structures intended for a multi-body gravitational scenario. Subsequently, the dominant environmental disturbance of the regions concerned, i.e. the solar radiation pressure, is incorporated in the formulation of motion. Then, it is demonstrated that the coupled dynamics can be mastered to advance smart mission strategies. The benefits of these solutions are clearly displayed without forgetting to verify their robustness with respect to design variables. In this context, an external critical disturbance is also identified and is addressed as secondary anomaly. Finally, the elastic dynamics of the structure are added to the equations of motion. Following a preliminary discussion of its effects in the multi-body problem, the analysis of the natural response suggests new chances to control and maneuver distributed architectures via geometry changes of the configuration itself.

Key Words: Large Space Structures, Restricted Three-Body Problem, Fully-Coupled Dynamics, Solar Radiation Pressure, Flexible Spacecrafts.

Estratto in Lingua Italiana

Molte delle future missioni per avanzare le frontiere dell'esplorazione spaziale sono proposte in punti di equilibrio del campo gravitazionale generato da più attrattori. In particolare, c'è grande attenzione ai sistemi Terra-Luna e Sole-Terra. Il punto di svolta consisterebbe nella capacità di collocare avamposti di grandi dimensioni e lunga vita operativa in prossimità di tali punti. Si tratterebbe di strutture destinate all'osservazione del nostro universo, così come a servire da spazioporto per missioni in tutto il Sistema Solare. E' ben nota l'esistenza di orbite periodiche, che ben risponderebbero allo scopo, attorno ai punti di interesse, ma purtroppo la dinamica in un problema multi-corpo è caratterizzata dal caos. Più correttamente, si parla di alta sensitività alle condizioni iniziali; ciò implica anche che piccole perturbazioni possono facilmente distruggere la traiettoria nominale. Inoltre, il problema non concerne solo la meccanica orbitale, ma anche quella di assetto non è ancora stata completamente e sistematicamente caratterizzata in questo ambiente. Pertanto, una più profonda comprensione delle dinamiche naturali può sicuramente migliorare la progettazione delle sopraddette missioni; in ultima istanza, sarà anche in grado di suggerire nuove modalità, di progetto prima, di controllo poi. Le grandi strutture spaziali sono per definizione architetture di considerevole estensione. È quindi lecito chiedersi quali siano gli effetti del gradiente di gravità sulla distribuzione di massa. Quindi, rinunciando all'ipotesi, comunemente adottata nella meccanica orbitale, di corpo puntiforme, in questa tesi viene sviluppata una formulazione dinamica che includa gli effetti del gradiente di gravità sull'estensione del velivolo. Normalmente studiate separatamente, la dinamica orbitale e di assetto risultano ora accoppiate. Analogamente, le grandi strutture spaziali esporranno una superficie maggiore alla pressione di radiazione solare rispetto a satelliti classici. Quindi, anche questo disturbo è aggiunto al modello. Normalmente questa perturbazione è sufficiente a far perdere la traiettoria nominale in un'intervallo temporale relativamente piccolo; tuttavia, in questo lavoro sono proposte astute contromisure, completamente basate sulla dinamica naturale del sistema. Queste soluzioni permettono una notevole riduzione del controllo richiesto su entrambi i moti orbitale e di assetto, all'estremo che potrebbe anche non essere necessario. Infine, grandi strutture spaziali possiedono verosimilmente un maggiore livello di flessibilità, sia come struttura nel complesso o a causa di alcune sue componenti. Perciò la dinamica elastica entra a far parte delle equazioni di moto. Nonostante ciò, la sollecitazione provocata dal gradiente di gravità è minima nelle regioni interplanetarie di interesse, con la conseguenza che, per classiche architetture spaziali, le deformazioni

sono piccole e incapaci di alterare la dinamica di corpo rigido. Tuttavia, configurazioni elementari con un più elevato grado di deformabilità possono essere utilizzate per esplorare questo scenario. Tali modelli possono rappresentare facilmente anche formazioni di volo o sistemi intreconnessi da giunti elastici. I risultati mostrano interazioni inaspettate tra moto orbitale, di assetto ed elastico; suggeriscono inoltre nuove modalità di controllo e manovra dell'assetto del velivolo che sfruttino il cambiamento di geometria della struttura.

Dinamica Accoppiata di Corpo Rigido

Come anticipato, in questo lavoro è documentato un nuovo studio degli effetti del gradiente di gravità sulla distribuzione di massa. Il contesto è quello del problema ristretto dei tre corpi, con le ulteriori assunzioni di moto planare e orbite circolari degli attrattori attorno al centro di massa del sistema. La chiave di una dinamica più accurata è lo sviluppo del potenziale gravitazionale in serie di Taylor almeno fino ai termini di secondo ordine. Il gradiente di gravità non solo influisce sulla meccanica orbitale e di assetto della struttura, ma anche ne accoppia le dinamiche, che generalmente sono affrontate indipendentemente. Per la prima volta, e non senza una certa meraviglia, i suoi effetti sono osservati sulle orbite di Lyapunov. A differenza di quanto osservato in un problema a soli due corpi, questa perturbazione è in grado di distruggere la traiettoria nominale entro un arco di tempo relativamente breve, comparabile a pochi periodi orbitali. Tutto questo è stato studiato nei sistemi Terra-Luna e Sole-Terra, riportando conseguenze più critiche nel primo caso. Inoltre, lo scostamento radiale finale risulta maggiore su orbite periodiche della famiglia L_2, rispetto a quello riportato sulla rispettiva controparte attorno ad L_1. Più complesso è l'andamento della deriva finale in funzione delle dimensioni dell'orbita: la curva del legame non è monotona, così che il corrispettivo minimo non corrisponde ne all'orbita più piccola della famiglia, ne tanto meno a quella più grande. Infine, viene mostrato la sensitività del fenomeno ad altri parametri quali l'orientamento, la velocità angolare e la topologia del satellite. In particolare, strutture con distribuzione di massa altamente anisotropa amplificano il disturbo; per converso strutture assialsimmetriche lo minimizzano, ma non lo nullificano.

Da queste considerazioni è possibile estrarre un nuovo ritratto della dinamica in un ambiente gravitazionale multi-corpo, il quale potrebbe rivelarsi sicuramente utile nella progettazione di missioni basate su grandi strutture spaziali; ma ancor più sorprendente è la geometria frattale della

risposta. Lo scostamento dell'orbita periodica di riferimento sembra possedere due proprietà indicate come auto-similarità e cross-similarità. La prima indica che la soluzione si ripete su scale di grandezza diverse con l'aumentare del tempo; la seconda significa invece che lo stesso andamento è osservato su scale diverse a seconda delle dimensioni della lunghezza caratteristica del velivolo. L'auto-similarità conferma che è sufficiente attendere un adeguato intervallo temporale per vedere l'errore sul riferimento amplificato al punto tale che l'orbita di Lyapunov è abbandonata rapidamente negli istanti successivi. In aggiunta, grazie alla cross-similarità, questo vale a prescindere dalla dimensione della struttura spaziale, che funge solo da fattore di amplificazione. Specificatamente, è dimostrato che lo scostamento radiale finale è proporzionale, entro il limite di errori piccoli, al quadrato della lunghezza caratteristica del satellite.

Recentemente, l'interesse sulla dinamica di assetto in un sistema gravitazionale a tre corpi ha suscitato un nuovo grande interesse nella comunità scientifica. Questo lavoro prosegue il percorso indicato dagli ultimi articoli pubblicati sull'argomento, che sottolineano l'importanza di considerare un rappresentazione completamente non lineare delle orbite di Lyapunov. Infatti, si dimostra che la non linearità del moto orbitale può fare la differenza anche su quello di assetto. Se si considerassero orbite quasi lineari, la risposta naturale di beccheggio sarebbe oscillatoria, e l'ampiezza delle oscillazioni limitata. La sola e unica circostanza che porterebbe alla divergenza della soluzione è la condizione di risonanza tra meccanica traslatoria e rotazionale. Al contrario, su un'orbita realmente non lineare, è molto facile che il velivolo inizi a ruotare indefinitamente. Questo comportamento è governato essenzialmente dalle dimensioni dell'orbita e dal rapporto di inerzia del corpo. L'indagine dimostra che, selezionata la grandezza dell'orbita, il rapporto di inerzia può essere diminuito per ottenere librazioni limitate. Viceversa, dato il rapporto di inerzia, la riduzione dell'ampiezza orbitale raggiunge lo stesso scopo. Nello scenario di strutture spaziali destinate ad orbitare attorno ai punti Lagrangiani, questo risultato è di notevole importanza per un miglior progetto del velivolo, così come nella selezione della traiettoria nominale.

Dinamica Accoppiata di Corpo Rigido con Pressione di Radiazione Solare

La pressione di radiazione solare è il disturbo ambientale dominante nelle regioni prossime ai punti di equilibrio in un sistema multi-corpo. Unita

alla intrinseca instabilità delle orbite di Lyapunov, è sufficiente a far divergere il moto dalla traiettoria nominale in poche rivoluzioni e, in alcuni casi, non se ne conta nemmeno una. Tuttavia, un progetto più ponderato del moto di riferimento può risolvere completamente, o almeno in parte, il problema. Includendo la radiazione solare nel modello dinamico, due strategie sono proposte per affrontare due scenari completamente diversi: si tratta di due casi di missione intorno al punto L_1, rispettivamente del sistema Sole-Terra e Terra-Luna. Nel primo sistema planetario, la costruzione dell'orbita operativa si basa sulla teoria delle vele solari. Dalla precedente letteratura, è noto infatti che una vela fotonica può muoversi lungo una orbita artificiale di Lyapunov, che risulta semplicemente traslata rispetto alla soluzione naturale. Ovviamente, questo è possibile solo se si vede rispettato un certo impianto di assunzioni preliminari. Ciò che non è banale, è intuire che un velivolo spaziale standard, dotato di pannelli solari, è in grado di emulare il volo di una vela solare piana e perfettamente riflettente. A tal fine, tra i vari arrangiamenti necessari, è importante sottolineare che è indispensabile garantire un puntamento verso la nostra stella. Ancora una volta riprendendo una vecchia idea per la propulsione solare e trasferendola ad architetture classiche, si dimostra che l'assetto del velivolo può essere stabilizzato passivamente, attorno alla direzione della radiazione incidente, tramite una lieve inclinazione dei pannelli solari (che potrebbero essere schematizzati con una forma a V). La robustezza della soluzione presentata è infine verificata per ampie variazioni dei parametri critici del sistema. In particolare, la sua validità è confermata per strutture fortemente anisotrope (soggette ad un maggiore momento gravitazionale) ed inclinazioni ragionevoli dei pannelli solari, che evitino riduzioni insostenibili della potenza elettrica erogata. Durante la sopraddetta indagine, si è anche identificata un brusca variazione della coppia di gradiente di gravità lungo grandi orbite periodiche, che introduce un disturbo improvviso ed intenso dell'assetto del sistema. A causa della sua correlazione con la vicinanza di P_2, questo fenomeno verrà detto anomalia del secondario.

Una strategia volta a mantenere una struttura spaziale in orbita attorno ad L_1, non ricavata da alcuna teoria precedente, viene proposta anche nel sistema Terra-Luna. Questo approccio inizia con l'estrazione di un'orbita con periodo pari al mese sinodico lunare della famiglia delle Lyapunov. Per motivi evidenti, viene battezzata orbita periodica di Lyapunov quasi eliosincrona. La seconda fase prevede invece che un particolare asse solidale al corpo sia costantemente puntato al Sole. Sotto queste condizioni, si è scoperto una fase solare iniziale che garantisce errori estremamente limitati della condizione di attraversamento dell'orbita periodica, nonostante

la presenza di radiazione solare. Purtroppo, questa tecnica da sola non è sufficiente a mantenere sul lungo periodo la traiettoria originale, ma lo sforzo del cosiddetto station-keeping è sicuramente ridotto. A seguire, la robustezza della soluzione sviluppata è, con soddisfazione, verificata per un'ampio spettro di variazione dei parametri di sistema. In altri termini, viene offerta una flessibilità adeguata all'analista. Per concludere, come nella precedente strategia, la dinamica accoppiata offre soluzioni naturali anche sotto gli effetti della pressione di radiazione solare; soluzioni che si rivelano nuovi ed efficaci strumenti di progetto per future missioni verso i punti di librazione.

Dinamica Accoppiata di Corpo Flessibile

La parte finale del presente lavoro tratta la dinamica di corpo elastico. La flessibilità della struttura è incorporata nella formulazione dinamica tramite la rappresentazione modale della variazione di forma. Considerando le caratteristiche di sonde spaziali classiche, nessuna alterazione apprezzabile della meccanica, predetta dal modello di corpo rigido, è osservata a seguito dell'introduzione delle componenti elastiche del moto. Si è in seguito realizzato che le regioni di equilibrio corrispondono a un minimo generale del carico ambientale sulla struttura, e quindi le deformazioni non sono tali da interagire di fatto con i moti di traslazione e rotazione del sistema. Invertendo la prospettiva, si può però giungere alla conclusione che, architetture altamente deformabili possono sopportare le sollecitazioni di quelle regioni interplanetarie, al contrario di quanto avverrebbe in prossimità della Terra. Per gettare le basi dello studio della dinamica di corpi superelastici nel problema multi-corpo, è opportuno iniziare considerando configurazioni elementari. Ancora una volta, l'analisi conferma che bassi valori di rigidezza, ben al di sotto del livello delle strutture standard, garantiscono un comportamento rigido in termini di moto orbitale e di assetto. Al contrario, se la configurazione è sufficientemente deformabile, l'interazione tra le dinamiche emerge. In realtà, è più corretto esplicitare che solo le componenti rotazionali ed elastiche del moto interagiscono mutualmente, mentre il cammino orbitale influenza si la soluzione elastica, ma non viceversa. La prima configurazione studiata è un satellite a manubrio. Diversi risultati sono presentati e discussi. Nello specifico, è interessante notare che le vibrazioni elastiche lungo l'asse del manubrio sembrano in grado di stabilizzare l'orientamento del sistema. Su piccole orbite periodiche, più la rigidezza diminuisce, più le oscillazioni di beccheggio vengono smorzate. Analogamente, su grandi orbite, il rateo di divergenza della equivalente

configurazione rigida può essere significativamente ridotto introducendo un certo grado di deformabilità. Tuttavia, bisogna anche prendere in considerazione che, un collegamento troppo debole tra le masse di estremità provoca la rottura del manubrio (la distanza tra le suddette masse diverge rapidamente verso infinito). In secondo luogo, si è studiata una configurazione a croce. In questo caso, il sistema è sensibile a parametri critici, quali la rigidezza interna o il rapporto di inerzia del corpo, al punto tale che la natura stessa della soluzione può essere modificata. Il comportamento è evidente negli effetti provocati dalla anomalia del secondario: il velivolo può infatti aumentare la sua velocità di rotazione, invertirne il verso o addirittura arrestare il moto angolare. In quest'ultima circostanza, l'anomalia del secondario innesca un trasferimento critico di energia dalla dinamica di assetto a quella elastica. Ognuna delle precedenti risposte di beccheggio è anche caratterizzata da una diversa storia della deformazione della configurazione. Inoltre, si è scoperto che, su orbite periodiche di grandi dimensioni appartenenti alla famiglia L_2, le oscillazioni dei bracci della croce sono in grado di stabilizzare l'orientamento iniziale del velivolo; senza di esse, l'angolo di beccheggio divergerebbe rapidamente dalla condizione iniziale lungo la traiettoria. In conclusione, diversi meccanismi alla base della dinamica di corpi super-elastici sono portati alla luce. Oltre a fornire un conoscenza più profonda del fenomeno, possono servire, a fronte di ulteriori sviluppi, come nuove tecniche di manovra e controllo di architetture distribuite, tra cui voli in formazione o sistemi multi-elemento con giunti elastici.

Acknowledgments

If there is anything barely close to being valuable in this work, I would like to devote to my beloved girlfriend Chiara; I would like to thank her for the support through my academic career as well as the sympathy and the patience (that are not among her most evident qualities!) demonstrated in these last months abroad. The other thing that has traveled with me all the way across the Atlantic, across the vast expanse of waters, is the friendship of persons such as Mohamed and Francesca. I thank Mohamed Attia Daman (I hope this to be the correct transliteration from the Egyptian language) for his enduring loyalty and also for never letting down my expectations, as some other so-called friends have. Secondly, my sweet Francy must know how the endless conversations with her have been insightful and pleasant. Finally, I want to share the success of the operation Saint Louis with Bombo and Stefano.

I am grateful for the opportunities that Professor M. Lavagna has offered me and for taking the trouble of arranging an exchange abroad. I hope to be able to return her trust, that has been a powerful source of motivation for me.

I truly appreciated the kindness bestowed upon me by Professor K.C. Howell and by her team to welcome me in this new adventure. I would like to write some words personally thanking to each one of the members of the Multy-Body Dynamics Research Group (Natasha Bosanac, Loic Chappaz, Christopher D. Geisel, Amanda Haapala, Galen Harden, Lucia Capdevila, Masaki Kakoi, Amanda Knutson, Tom Pavlak, Raoul Rausch, Wayne Schlei, Cody Short, Rohan Sood, Jeff Stuart, Mar Vaquero, Theodore Wahl, Ashwati Das), but it would require another whole new chapter! I'm sure that in the coming years there will be plenty of chances to display my gratitude for their friendship and collaboration.

I would like to express my appreciation for Doctor R. Armellin, whose constant and prompt help has been crucial for the accomplishment of this Thesis. Also Professor M. Lavagna deserves further thanks for the initial idea of the project, as well as Professor K.C. Howell and her team for having provided a fertile environment where the work was eventually concluded. Especially, I thank Amanda Knutson for the profitable discussions and collaboration that we have had together.

Finally, I owe thanks to the Alta Scuola Politecnica and the Politecnico di

Milano, since they both have provided the funding opportunities to support my academic and personal growth.

Contents

1 Introduction

Io stimo più il trovar un vero, benchè di cosa leggiera, ché l' disputar lungamente delle massime questioni, senza conseguir verità nissuna.
(G. Galilei, Opere, IV p.738)

Contents

In this work the dynamics of large space structures are investigated in a multi-body gravitational environment. Given the ever increasing interest in the multi-body problem, with special focus on the three-body case, this work tries to envision the next generation of large space structures, which could take great advantage of the presence of a complex gravitational field. We can imagine for instance, large telescopes placed in strategic points of the gravitational configuration (*i.e.* periodic orbits around the Lagrangian points), as this already occurs for smaller vehicles; likewise those points appear suitable for new space stations that would be the most remote outpost of human colonization and serve as a base for further explorations. Moreover, in the future we could exploit large solar sails to ply particular channels of motion (*i.e.* manifolds) related to the three-body dynamics. Telescopes, space stations, solar sails, antennas and deployable appendages (*e.g.* solar panels) are only a sample of large space structures, some of which are already flying. Rather than reducing the dynamics of these architectures to a rough model, it would be better to consider an advanced formulation of their motion in order to facilitate the design of missions that

may otherwise be infeasible.

1.1 Problem Definition

The goal of this research is to examine the dynamics of Large Space Structures (LSS) under a multi-body gravitational environment. The subjects of this investigation (*i.e.* the Large Space Structures) as well as the background scenario (*i.e.* the multi-body gravitational field) possess unique characteristics and are promising directions for the next developments in space exploration and astronautics. Therefore, overlapping the two is supposed to offer interesting and novel results that will improve the basis for the LSS mission design. They will also add a deeper insight into the spacecraft dynamics.

Firstly, corresponding to Balas [1], the Large Space Structures retain the following distinctive characteristics:

1. they are distributed parameters systems;
2. they have an higher degree of flexibility;
3. their natural damping is significantly low, even if poorly estimated;
4. the possibility to test their dynamical behavior on-Earth is quite limited;
5. they usually undergo stringent requirements on shape, orientation, alignment, vibrations suppression and pointing accuracy.

Secondly, when more than two bodies interact gravitationally the resulting motion can present a "chaotic" behavior. This possibility was already inferred by Poincaré when discussing the dynamics nearby the "now-called" transverse homoclinic points in his essay about the three bodies [2]. One century later, the "theory of chaos" was broadly spread among the scientific community and widely applied (sometimes unnecessarily) to different disciplines. Plenty of papers exist in this field, and it is beyond the scope of this work to review them. It will be enough to recall Holmes [3], who summarizes the arguments presented in the 270 pages of the Poincaré's essay from a more modern point of view and offers an introduction to "chaos" with examples from the celestial mechanics. For a dynamical system to be classified as chaotic, it must be high sensitive to the initial conditions (a necessary but not sufficient condition) [4]. This means that, two trajectories departing from very similar initial conditions will separate rapidly and

will result in totally different paths despite the initial vicinity. From another perspective, such behavior implies that extremely small perturbations can dramatically alter the system response.

Hence, the basic idea underlying this project is to couple the peculiarities of the Large Space Structures with the particular dynamics in a multi-body problem, so the once neglected secondary phenomena can rise to the level of primary relevance. In more details, the research objectives are as follows:

***i*)** *Investigate the coupled orbital and attitude dynamics for extended bodies.* The current knowledge of the orbital dynamics in a multi-body system has been mainly built focusing on a point mass model to represent the actually extended space vehicle. The presented study waives the assumption of a zero-dimensional space vehicle and looks at the effects of the mass distribution of extended flying vehicles on both orbital and attitude motions in the framework of the multi-body problem. To this end, the gravitational force is computed including the effect of a distributed mass. This naturally leads the orbital motion to be coupled with the attitude dynamics.

***ii*)** *Compare the effects with other perturbations.* The insight gained through the previous point is applied to a scenario approaching real design studies. Thus, other perturbations than the gravity gradient are accounted and discussed. The primary purpose is answering the question if the identified gravity disturbance can be exploited as effective tool to maneuver and control both the orbital and attitude time history. In the negative event, other strategies will be proposed to design missions under the fully-coupled dynamics imposed by the dominant perturbation.

***iii*)** *Introduce and examine the effect of structure flexibility.* As long as LSS are accounted for, it is known that the spacecraft possesses a higher degree of flexibility due to both the structure size and the materials used. Thereafter, a formulation to introduce elastic bodies is proposed. Then, effects of flexibility are presented and discussed.

1.2 Previous Work

The problem of coupling between the attitude libration and the orbital motion was known from the dawning of analytical mechanics as Lagrange was

concerned about the libration of the Moon. In fact, in his work "Théorie de la Libration de la Lune" [5] a first discussion about the effects of the body libration (*i.e.* the Moon) on its orbit is reported. After that, one of the first recent contributions came from Duboshin [6], who delivered a general form for the equations describing the coupled attitude and orbital motions of gravitationally attracting bodies. Those equations are subsequently specialized employing spherical and axisymmetric body mass distributions, while the assumptions to separate the translational and rotational dynamics are investigated for such cases. An actual implementation of the coupled dynamics for a dumbbell satellite in circular orbit was accomplished by Moran [7]. He studied the effects of plane librations on the orbital motion, showing that they produce a sinusoidal perturbation on the original orbit. Debra [8] extended the analysis to a body with an arbitrary mass distribution, focusing on the conditions to obtain bounded free librations. Along with different body shape, elliptical orbits can be selected as basic trajectories [9, 10, 11]. In particular, Yu [9] provided the spacecraft with damping on the attitude motion and studied its effect on the long-term. Mohan [11] instead addressed the interchange of energy between the translation of the center of mass and the body rotations in the near-resonant condition for the pitch oscillations.

So far, the interest arisen for the fully coupled models have been marginal from an engineering perspective. The main reason beyond this scant interest is the nature itself of the interaction. As a matter of fact, both the orbit and attitude motions depend on the mass distribution and orientation, but the order of perturbations incorporated in a purely gravitational coupled model are extremely small, especially for the center of mass motion. Their magnitude is function of the spacecraft size relative to the orbital radius in a quadratic or higher order fashion. The mutual influence of orbit and attitude dynamics under a Newtonian central gravitational field is shown explicitly by expanding the gravitational force and torque in a Taylor series in the small parameter $\varepsilon = L/r_0$, where L is characteristics of the spacecraft size and r_0 is the orbital radius. The gravitational coupling appears when terms at least of the second order (ε^2) are retained. The usual practice for common spacecraft is to neglect terms of order higher than ε^2 [12, 13, 11]. But, for very large spacecraft (as for example solar power stations or solar sails) also terms up to the four order (ε^4) could be considered for studying the coupled problem. In this event, higher-order moments of inertia would show up in the expression of the gravity force and torque. These higher-order moments of inertia as well as the gravitational forces and torque in ε^4 can be derived following various papers [14, 12, 15, 10]. Thus, as it has

been observed the gravitational interdependence of rotational and translation motions in the classical Keplerian dynamics affect clearly only the attitude dynamics (in the form of the well-known gravity torque), while it appears negligible in the orbital motion for any practical purpose [16]. To provide the reader with a concrete feeling of that, it can be recalled the study of Misra and Modi [17]. They computed the orbital perturbation for the Radio Astronomy Explorer (*RAE*) satellite (launched by NASA in July 1968). *RAE* had to measure longwave radio signals from the outer space, so it was composed by four long stem-type antennas, as depicted in Figure 1.1. Other important proprieties are listed in Table 1.1. With a characteristic length $l = 460$m $(1500$ft$)$ and a semi-major axis $a_0 = 12200$km $(7600$ miles$)$ the radial oscillatory perturbation of *RAE* after a year has an amplitude of 4.87m $(16$ft$)$.

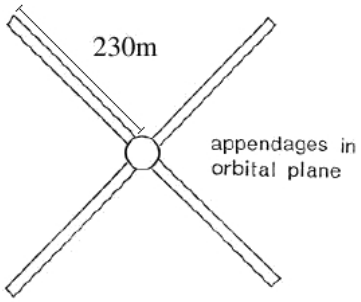

Figure 1.1: *RAE* sketch from [17].

Mass = 147 kg (326 lb)
Inertia = 367.4 $\times 10^3$ kg m^2
(271 $\times 10^3$ slug ft^2)
Length = 460 m (1500 ft)
Semi-axis = 12 200 km
(7600 miles)
Eccentricity = 0.001
Period = 224.4 min

Table 1.1: *RAE* data.

Large Space Structures are usually designed as the aggregation of more components, some of them of considerable extension or even thought as inflatable or deployable appendages. So, considered the size of the overall structure as well as that of the single components and the materials adopted, it seems necessary to account the effect of flexibility in the dynamics of such architectures. For this reason, many approaches has been developed since the 60s to incorporate the elastic deformation in the dynamic analysis of complex structures. This problem (known as Flexible Multi-Body[1] Dynamics) does not concern only the design of spacecrafts, but

[1]Throughout the work, Multi-Body refers to the dynamical problem due to the gravi-

is an extremely general issue in the engineering science: it easily includes the study of ground, air transportation vehicles, manufacturing machines, manipulators, robots and even bio-dynamical systems. As consequence, a huge amount of publications infests the literature to the extension that the difficulty is shifted from findings previous materials on the topic to selecting the most significant contributions. The status up to 2003 and some recent developments in computational modeling of flexible multi-body systems are summarized in the review Wasfy and Noor [18]. In the author's opinion, this review is well organized presenting many tables to compare several methods and can be an optimal starting point for any general purpose research dealing with the multi-body dynamics. In addition, the number of references accounted in this article (*i.e.* 877) gives a clue of the size of the literature written on the Flexible Multi-Body Dynamics. A more concise, but not less effective review effort is offered by Shabana in [19]. In particular, the main strategies available for the formulation of the problem are here discussed more extensively. This work is also useful to understand the basis of the algorithms developed in this thesis.

Narrowing the horizon to space systems, the first application of multi-body dynamics to a spacecraft was published in 1965 by Hooker and Margulies [20]. The first spacecraft considered was a set of rigid bodies interconnected in the so-called tree topology, where no closed chains of bodies exist. Their dynamics equations were delivered firstly using the Newton-Euler method. Later, Ho introduced the capability of modeling the terminal bodies of the tree configuration as flexible structure and wrote the equations of motion by the procedure he developed and named Direct Path Method [21, 22, 23]. This method was used to simulate a spinning Skylab (with flexible booms) and the interplanetary probe Viking (with flexible solar panels and thrust vector control) [24]. In doing so, Hooker assumed elastic modes to represent appendages elastic deformation and included the expression for the kinetic energy and the angular momentum as a tool to monitor the accuracy of the simulations. The tree topology with flexible appendages was also addressed by Linkins [25], where the flexible bodies were not restricted to small deformations. A complementary class of problems was investigated by Hughes [26], who considered a chain of structurally elastic bodies with two rigid bodies at the extremities. The author applied his equations to simulate the dynamics of the Shuttle remote

tational field exerted by multiple attractors. However, in this Chapter only, the expression will address also the dynamics of architectures consisting of several components, which are connected by any kind of mechanical joints. The meaning of Multi-Body should be clear from the context.

manipulator arm. A review of the early flexible multi-body formulations in the spacecraft dynamics literature was accomplished by Jerkovsky in [27], where the tree topology is widely adopted among several methods. The beam theory was also largely employed to incorporate flexibility in the space structures dynamics. Both the whole spacecraft [28, 29, 30] or only its attachments can be modeled as beam-like structures [31, 32]. In particular, the formulation used by Simo and Vu-Quoc in [30] was extended to open-chain as well as closed-loop configurations [33]. But, the possibility to reproduce non-linear deformations of the spacecraft (also referred as geometrical exact structure) with their algorithm [34, 35, 33] is even more interesting. Another important category of possible spacecraft configuration was deeply explored by Meirovitch, who focused on gyroscopic systems and spinning bodies containing elastic parts [36, 37, 38]. He finally delivered with Quinn in [39] the equations of motion for studying the slewing and the vibrations suppression of a flexible spacecraft, both in orbit and in an Earth-based laboratory. They proposed an approach known as perturbation method; in fact the large rigid-body maneuvers are assumed to be the unperturbed motion and the effects of flexibility are computed as perturbations of that motion. The librations dynamics of spacecrafts accounting a certain degree of flexibility has been considered of primary importance since the early stage of astronautics, as demonstrated by the works reviewed by Modi in [40]. Modi himself with other authors presented a Lagrangian formulation for both the orbital [17] and the libration [32] dynamics of cluster type spacecraft with an arbitrary number of flexible appendages. The direct Lagrangian approach may seem inappropriate to the multi-body dynamics, as it involves extremely lengthy expressions, such as the kinetic energy, and many intermediary equations that are discarded when the final dynamic system is written. Nonetheless, this approach experienced a significant success thanks to the symbolic manipulation available with the advent of high speed computers. Thus, the above model was developed by including shift in the center of mass, changing of the central body inertia during deployment operations and the offset of the appendages attachment point [41]. Further contributions [42] extended the formulation to deal with more complex configurations, incorporate thermal deformations and allow appendages deployment maneuvers. Hence, the method was applied to study the dynamics of different proposed space structures [16, 43]. It is worth to recall that all the aforementioned works are based on well-known - even historical - formulations of the dynamics: from the Newton/Euler equations through the D'Alembert principle to the Lagrangian formalism. But a new method was introduced in the last century due to Kane in a first series of three papers [44, 45, 46]. The method

derives from new kinematic quantities discovered by Kane and nowadays called partial angular velocities and partial velocities. This method and its advantage are compared with all the other existing formulations by Kane itself [47] or by other authors like Banerjee in a recent review [48]. In particular, it is claimed that the method leads directly to the simplest form of the dynamic equations. Besides that, it is really inspiring noticed that the novel Kane's method was originally thought to overcome the challanges imposed by the design of complex spacecraft configurations, along with beign naturally suitable for symbolic manipulation and numerical implementation. An example of its employment for a generic large mechanical system is presented by Singh et al. in [49].

The dynamics explored by the authors earlier mentioned is limited to the presence of a single attractor (in the most of cases the Earth). But the next generation of Large Space Structures will be likely placed in area of the cosmic space where more gravitational fields act on the orbiting vehicle. So far, only few works addressed the motion of extended spacecrafts in a multi-body gravitational problem. The model adopted in the following studies is the Restricted Three Body Problem (CRTBP). Thus, Kane and Marsh first published a research on the attitude stability of a symmetric satellite [50]. The spin axis of the satellite corresponds to its symmetry axis and is normal to the orbital plane of the two attractors. Furthermore the satellite is assumed to rest artificially at the equilibrium points, so only the attitude dynamics is considered. The same framework was adopted by Robinson except for the shape of the spacecraft. In fact he started with the examination of a dumbbell satellite [51] and then proposed the linear stability diagram for an asymmetric body at the equilibrium points [52]. A similar analysis was also conducted by Barkin in [53]. Abad et al. [54] introduced quaternions to study the rotations of a spacecraft in the equilateral equilibria. Recent papers came from Bucker et al. [55], Wong et al. [56] and Knutson et al. [57]; Bucker employed the Poincarè maps to trace the libration motion of a satellite artificially fixed at the equilibrium points; Wong dismissed the assumption of spacecraft held in the equilibria and investigated the attitude dynamics of a rigid body on the periodic orbits of the Sun-Earth system, using a linear approximation for both Lyaponouv and halo orbits; Knutson instead explored the attitude motion in a nonlinear regime, using numerically computed Lyapunov orbits. In particular, the scope of the latter work is to develop a general framework for the fully coupled dynamics in the restricted three body problem by the application of the Kane method, but as the previous studies it remains mainly focused on the rotational motion, while the implications on the orbital dynamics

are only preliminarily delineated.

1.3 Scope of the Present Work

The scope of the present work is the fully-coupled dynamics of Large Space Structures (LSS) in the framework of the Planar Circular Restricted Three-Body Problem (PCR3BP). To begin with, a formulation is developed to predict the dynamics of rigid structures including the gravity gradient effects on both the orbital and attitude motion. Hereafter, the analysis is focused on the Lyapunov periodic orbits belonging to the L_1 and L_2 family in the Sun-Earth as well as Earth-Moon system. Then, the gravity gradient perturbation is compared to the solar radiation pressure, which reveals to be the dominant disturbance, especially when addressing the orbital dynamics. Hence, a mission design strategy based on the solar sails theory is proposed to place standard spacecrafts around the Sun-Earth L_1 point, despite the aforementioned perturbation. Similarly, a solution is advanced also for the L_1 point in the Earth-Moon system, but it employs a totally novel approach. Eventually, flexibility is incorporated into the dynamics formulation and, after a preliminary discussion of its effects, two deformable architectures are chosen to dive into this new scenario. The study is organized as follows:

Chapter 2: The dynamical models used in the investigation are introduced. In the first section the PCR3BP is presented, and the characteristics of the differential equations of motion are examined. In particular, the identification and the construction of Lyapunov periodic orbits is explained. In the second Section, the general framework of methodologies to describe the dynamics of LSS is discussed. Every model is basically consisting of three parts (elastic discretization, kinematics and dynamics) and each of those elements is separately detailed.

Chapter 3: the rigid body formulation of the fully-coupled motion in the the PCR3BP is delivered. Firstly, the kinematics representation, the coordinate systems and the variables adopted are clearly displayed; then, the Lagrangian function of the system is computed. Specifically, the gravitational potential is expanded in Taylor series up to the second order terms to account the effects of the gravity gradient over the mass distribution. Finally, the equations of motion are derived via the Lagrangian procedure. The part of the differential system describing the orbital motion is rearranged accordingly to the Encke's method in order to predict more accurately the perturbation introduced with the gravity gradient.

Chapter 4: the analysis of the fully-coupled rigid motion is presented. Briefly, evidence to assess the reliability and the accuracy of the algorithm implemented are furnished. Then, the dynamical behavior is deeply investigated. In the second Section, the drift from the reference trajectory provoked by the gravity gradient disturbance is characterized as function of the different variables of the overall system (*e.g.* environment, initial conditions, spacecraft size and topology). In the third Section, the boundedness of the attitude solution is studied. The parameters that mostly govern this phenomenon are identified and explored to draw an useful insight into the design of LSS on Lyapunov orbits. In the last Section, the novel perturbation is compared to the solar radiation pressure to understand if there is the chance to employ the former to maneuver the vehicle.

Chapter 5: the analysis of the fully coupled motion under the solar radiation pressure is presented. To begin with, an accurate model of the radiation interaction with the spacecraft surfaces is presented. On that basis, the dynamics around the L_1 Sun-Earth point is studied and a strategy derived from the solar sails theory is proposed for the passive station keeping of solar arrays powered vehicles. Outcomes related to the attitude motion reveal an interesting phenomenon appearing on large Lyapunov orbits, that will be named secondary anomaly. After this short digression, the Earth-Moon system will be considered too. Here, the dynamics is significantly different from the Sun-Earth environment. In this scenario, a entirely novel strategy is advanced to mitigate the effects due to the solar radiation pressure. This solution is based on the intuition to couple a particular trajectory (quasi sun-synchronous) with a specific spacecraft pointing. A sensitivity campaign over the design parameters is performed to prove the flexibility and the robustness of the approach devised.

Chapter 6: the flexible body formulation of the fully-coupled dynamics in the PCR3BP is delivered. The method presented in Chapter 3 is rearranged to incorporate the structure deformability. Above all, the discretization of the elastic problem is discussed and the method adopted is stated. The outline of the remaining part is basically the same as Chapter 3: analogous steps are perfomed and eventually the equations of motion including the elastic dynamics are written and detailed.

Chapter 7: the analysis of the flexible spacecrafts dynamics in vicinity of the librations points is reported. In the first Section, the major concerns for reproducing a rigid motion mutually coupled to its elastic counterpart are

expressed. In the latter Sections, the investigation is specialized to two very simple and very flexible configurations: a dumbell and a cross. A huge set of simulations is run to survay the possible responses and the most meaningful results are exposed for both the architectures. It is studied how the reference orbit, the internal stiffness and the spacecraft topology affect the attitude as well as the elastic motion. Specifically, the analysis of dumbell satellite is focused on orbits around the L_2 Sun-Earth point, while the cross-satellite is mostly assumed about both the L_1 and L_2 points of the Earth-Moon system.

Chapter 8: Concluding remarks are offered along with recommendations for future research.

2 Background

Contents

In this Chapter the background knowledge of the present research is recalled. In the first part of the Chapter the multi-body gravitational scenario adopted is defined. Hereafter, the dynamics connected to the selected model is discussed. In the second part of the Chapter the general methodologies to describe the motion of flexible interconnected bodies are reviewed.

2.1 The Circular Restricted Three-Body Problem

Consider three masses that interact gravitationally. The first and more massive body P_1 defines the primary attractor, so it can also be referred as primary; in the same way, the second attractor in order of mass P_2 is called

secondary. Finally, the third body P_3 is supposed to represent the spacecraft. The motion of P_3 is addressed under the following assumptions:

- The mass distribution of each body is considered perfectly spheric.
- P_1 and P_2 are on circular orbit around their common center of mass.
- P_1 is more massive than P_2.
- The mass of P_3 is negligible compared to P_1 and P_2 and does not affect their motion.
- The motion of P_3 is limited to the plane identified by the circular orbits of P_1 and P_2.

The resulting problem is universally known as the Planar Circular Restricted Three-Body Problem (PCR3BP). Most of the books on orbital mechanics widely present this problem, such as [58, 59]. So far, the PCR3BP may seem inappropriate to describe the dynamics of particles in the solar system. Above all, the solar system objects rarely retain exact circular orbits or spherical distribution of mass. Nonetheless, this model is largely adopted even for real mission analyses as it still provides a valuable approximation of the qualitative behavior of certain systems, that surely represent possible scenarios for different space missions (*e.i.*the Earth-Moon or Sun-Earth systems) [60]. Further details of the PCR3BP are summarized in the next sections.

2.1.1 Equations of Motion

To begin with, the problem geometry is set out. Since the two attractors rotate with a constant angular velocity on circular orbits, it is commonly adopted a rotating coordinate system to write the equations of motion for the remaining particle P_3. This frame is placed in the common center of mass of P_1 and P_2 and rotates with a constant angular velocity Ω with respect to an inertial reference system, so that the two primary bodies always lie on the rotating x-axis. As Ω is the orbital angular velocity of P_1 and P_2 about their center of mass, the rotating frame is called synodic frame. In this Chapter the synodic frame is also denoted as the xy-frame, while the inertial reference is the XY-frame. Hence, the position of P_3 relative to the system center of mass is indentified in the synodic frame using the coordinates (x, y) or otherwise the position vector $\boldsymbol{r}$. It is also useful to define the position vectors $\boldsymbol{r_1}$ and $\boldsymbol{r_2}$, which represent the location of P_3 relative to P_1 and P_2 respectively. The system is normalized with the following quantities

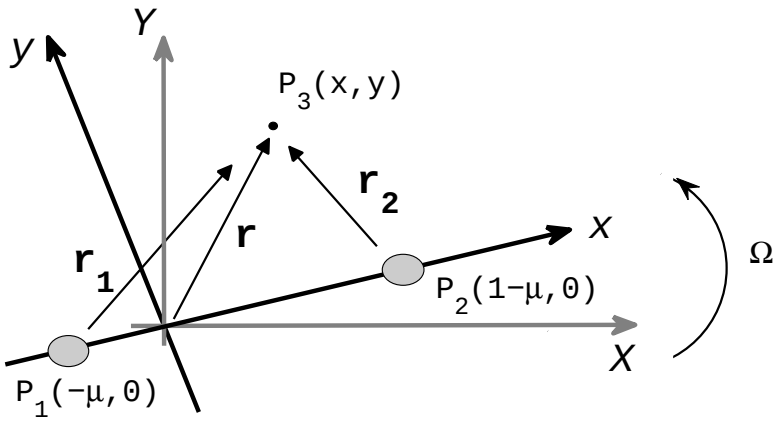

Figure 2.1: Geometry of the R3BP.

appearing as unit: the total mass system m, the distance between the two attractor centers d, the angular frequency Ω of the circular motion of P_1, P_2 and the universal constant of gravity G. When appropriate, the quantities can be converted in dimensional units of the problem scale. Length, velocity and time are converted as follows

$$\begin{aligned} \text{[Length]} \quad & \ell' = L\ell \\ \text{[Velocity]} \quad & v' = Vv \\ \text{[Time]} \quad & t' = \frac{T}{2\pi}t \quad , \end{aligned}$$

where the primed quantities are dimensional, while the unprimed are normalized; L is the distance between P_1 and P_2, V is the orbital velocity of P_1 and T is the orbital period of P_1 and P_2. Such quantities are tabled for different systems in [60]. Otherwise, the only parameter of the system left after the normalization is the mass parameter

$$\mu = \frac{m_2}{m_1 + m_2} \quad , \tag{2.1}$$

where m_1, m_2 are the masses of P_1 and P_2. The mass parameter defines the positions in non-dimensional units of the primary as well as of the sec-

ondary in the synodic frame; thus, recalling the assumption $m_1 > m_2$, P_1 is located in $(-\mu, 0)$ while P_2 is in $(1-\mu, 0)$. The geometry described so far is depicted in Figure 2.1.

There are several ways to derive the equations of motion of a spacecraft within the PC3BP. Here, the Lagrangian approach is employed. According to this method the equations of motion for a general holonomic mechanical system are

$$\frac{d}{dt}\Big(\frac{\partial \mathcal{L}}{\partial \dot{q}_i}\Big) - \frac{\partial \mathcal{L}}{\partial q_i} = Q_i \quad , \tag{2.2}$$

where $\mathcal{L}$ is the Lagrangian function, q_i denote the generalized coordinates and Q_i the generalized non-conservative forces. In the rotating frame, (x, y) are adopted as generalized coordinates and the Lagrangian function results as

$$\mathcal{L}(x, y, \dot{x}, \dot{y}) = \frac{1}{2}((\dot{x} - y)^2 + (\dot{y} + x)^2) - U(x, y) \quad , \tag{2.3}$$

with the gravitational potential represented by

$$U(x, y) = -\frac{\mu_1}{r_1} - \frac{\mu_2}{r_2} - \frac{1}{2}\mu_1\mu_2 \quad . \tag{2.4}$$

The terms appearing in eq. (2.4) are defined as

$$\mu_1 = 1 - \mu \tag{2.5}$$
$$\mu_2 = \mu \tag{2.6}$$
$$r_1 = \sqrt{(x + \mu)^2 + y^2} \tag{2.7}$$
$$r_2 = \sqrt{(x + \mu - 1)^2 + y^2} \quad . \tag{2.8}$$

Assuming no other actions than gravity and substituting eq. (2.3), (2.4) in (2.2), it yields to the system of equations describing the spacecraft motion

$$\begin{cases} \ddot{x} - 2\dot{y} &= -\bar{U}_{/x} \\ \ddot{y} + 2\dot{x} &= -\bar{U}_{/y} \end{cases} , \tag{2.9}$$

where the subscript $_{/(\cdot)}$ denotes the partial derivative respect to the variable $(\cdot)$ and the augmented or effective potential $\bar{U}$ has been introduced to incorporate the effects due to a non-inertial frame

$$\begin{aligned} \bar{U} &= -\frac{1}{2}(x^2 + y^2) + U(x, y) \\ &= -\frac{1}{2}(\mu_1 r_1^2 + \mu_2 r^2) - \frac{\mu_1}{r_1} - \frac{\mu_2}{r_2} \end{aligned} \quad . \tag{2.10}$$

2.1.2 Jacobi Constant

The expression of the Lagrangian function (2.3) does not depend explicitly on time (*i.e* $\partial\mathcal{L}/\partial t = 0$) and the equations (2.9) are an Hamiltonian system. Therefore, an energy integral of motion exists. Straightforwardly, that is the mechanical energy E of the particle P_3

$$E(x, y, \dot{x}, \dot{y}) = \bar{U}(x, y) + \frac{1}{2}v^2 \quad , \tag{2.11}$$

where $v^2 = \dot{x}^2 + \dot{y}^2$. But for historical reasons, the energy integral is formulated in a slight different way for the CR3BP; in astronautics is commonly used the Jacobi constant

$$JC(x, y, \dot{x}, \dot{y}) = -2E \quad . \tag{2.12}$$

Due to the different sign of JC and E, it is worth to notice that when the Jacobi constant decreases the mechanical energy increase, and vice versa. The existence of an integral of motion it is an extremely valuable tool to test the correctness of any numerical algorithm and even to estimate its accuracy.

2.1.3 Equilibrium Points

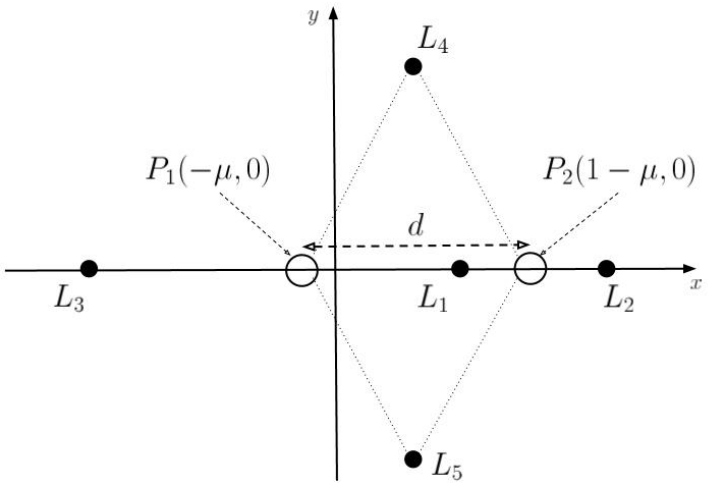

Figure 2.2: Geometry of the equilibrium points.

In particular positions of the configuration space the centrifugal force associated with the rotation of the synodic frame and the gravitational attraction balance each other, so that a spacecraft located in those coordinates will rest fixed relative to the synodic frame. To seek for the location

of the equilibria points ones have to compute the gradient of the effective potential. The coordinates where the gradient $\nabla\bar{U} = 0$ correspond to the equilibrium points. Those equilibria are divided in two classes (see Figure 2.2):

- three equilibrium solutions lie on the x-axis and are referred as collinear points. Specifically, the point between the two attractor is labeled L_1; the point behind the secondary is L_2; the point located before the primary is called L_3.
- two equilibrium solutions retain an unit distance (in non-dimensional units) from both the primary and the secondary. As each of these points forms a equilateral triangle with the attracting bodies, they are known as the equilateral points L_4 and L_5.

It is straightforward to demonstrate that $\bar{U}(r_1, r_2)$ has the same critical points of $\bar{U}(x, y)$ [60] when $y \neq 0$. It yields

$$\begin{cases} \bar{U}_{/r_1} = & -(1-\mu)r_1 + \dfrac{(1-\mu)}{r_1^2} & = 0 \\ \bar{U}_{/r_2} = & -\mu r_2 + \dfrac{\mu}{r_2^2} & = 0 \end{cases} \quad . \tag{2.13}$$

The unique solution of eq. (2.13) is $r_1 = r_2 = 1$, which necessarily leads to the equilateral configuration for P_1, P_2, P_3. For the present work, the collinear points are more interesting, because currently considered for many space missions. These equilibria correspond to the critical points of

$$\bar{U}(x, 0) = -\frac{1}{2}x^2 - \frac{1-\mu}{|x+\mu|} - \frac{\mu}{|x+\mu-1|} \quad . \tag{2.14}$$

The computation of $d\bar{U}(x, 0)/dx = 0$ leads to a quintic equation after simplification. Thus, the distance of $L_i, i = 1, 2$ from the secondary results from the unique positive zero γ_i of the polynomial

$$\gamma^5 \mp (3-\mu)\gamma^4 + (3-2\mu)\gamma^3 - \mu\gamma^2 \pm 2\mu\gamma - \mu \quad , \tag{2.15}$$

where the upper sign is for γ_1, the lower for γ_2. The zeros of (2.15) shall be solved numerically (*e.g.* by the Newton method), but a good first guess can be obtained with a series expansion of the solution. One largely adopted is from Szebehely [61]

$$\gamma_1 = r_h(1 - \frac{1}{3}r_h - \frac{1}{9}r_h^2 + \ldots) \quad , \tag{2.16}$$

$$\gamma_2 = r_h(1 + \frac{1}{3}r_h - \frac{1}{9}r_h^2 + \ldots) \quad , \tag{2.17}$$

with $r_h = (\mu/3)^{1/3}$. Finally, it is worth to point out that the equilibrium points are also called Lagrangian points (in memory to their discoverer) or libration points (in correlation to the periodic motion around them - see next section).

2.1.4 Lyapunov Periodic Orbits

Writing eq. (2.9) into the first order form and linearizing them it is possible to study the stability of the libration points. The reduction to a linear system means that results are accurate when the motion is limited to the vicinity of the equilibrium point, but some considerations about the stability of the non-linear system can be drawn too. The linear version of eq. (2.9), written as first order differential equations, is

$$\begin{cases} \dot{x} = & v_x \\ \dot{y} = & v_y \\ \dot{v_x} = & 2v_y + ax \\ \dot{v_y} = & -2v_x - by \end{cases} , \tag{2.18}$$

where

$$a = 2\bar{\mu} + 1 \tag{2.19}$$

$$b = \bar{\mu} - 1 \tag{2.20}$$

$$\bar{\mu} = \mu|x_e - 1 + \mu|^{-3} + (1 - \mu)|x_e + \mu|^{-3} \tag{2.21}$$

and x_e is the position of the equilibrium point. For the collinear libration points, the eigenvalues analyses of the system (2.18) reveals two real eigenvalues and other couple purely imaginary [60]. Among the real eigenvalues, one is positive, which means that the motion near the equilibrium is diverging. By the way, the presence of two purely imaginary values indicate the possibility of strictly oscillatory motion. In the spatial case, complete families of three dimensional periodic orbits - and even quasi-periodic - appear around the libration points [62]. The geometry of these families is quite complex or at least varied, but for the purpose of this work it is sufficient to restrict our-selves to the orbits in the plane of the system, known as Lyapunov orbits.

2.1.5 Computation of Lyapunov Periodic Orbits

Once assessed the presence of planar periodic orbits, it is practical interest to compute such trajectories. For the linear system a close solution exists as direct consequence of the eigenvalue analysis in the form [60]

$$\begin{cases} \xi = & -A_x \cos(\lambda t + \phi) \\ \eta = & +\kappa A_x \sin(\lambda t + \phi) \end{cases} , \tag{2.22}$$

where $\xi = x - x_e$, $\eta = y - y_e$ and λ, ϕ are the planar frequency and phase, respectively. A_x, κ are two constants denoting the planar amplitude of the orbit in the x direction, and its ratio with the amplitude in the orthogonal direction. An improved model was developed by Richardson [63], who proposed a third order solution for periodic orbits. Despite a considerable progress in the analytical computation of periodic orbits, no solutions seem enough accurate when tested in the fully non linear system. As soon as the trajectory is numerically integrated, it quickly diverges from the linearly-predicted path. So special techniques are required to assure the precise identification of the Lyapunov orbits. To this end, a differential correction method is usually employed [64]. The basic idea underlying the method is to make use of the linearly approximated dynamics to target particular initial conditions, that generate a periodic orbit. The easiest condition to target is the perpendicular crossing of the x-axis, that is certainly necessary - but not sufficient - for a Lyapunov orbit (because of the problem symmetry with respect to the x-axis). The perpendicular crossing does not automatically lead to a Lyapunov orbit, so the linear or higher order approximation of those orbits is extremely useful: it is exploited to generate an initial guess close enough to the actual solution to make the differential correction convergent. The outline of this procedure is the following [60]:

1. Utilize an analytical approximation of the Lyapunov orbit to guess a first set of initial conditions $(x_0, 0, 0, v_{y_0})$. The initial position lies on the x-axis and the initial velocity is orthogonal to the same axis.

2. Integrate the non-linear system with strict tolerance (*e.g.* 10^{-14}) until y changes sign.

3. Change the time step to target the crossing condition as accurately as possible (*e.g* $|y(t)| < 10^{-11}$).

4. Compute the state transition matrix at the crossing time t_1, which is the linear relationship between small initial and final displacement

$$\delta \boldsymbol{x}(t_1) = [\Phi(t_1, t_0)] \delta \boldsymbol{x_0} \quad ,$$

where $\boldsymbol{x}$ is the state vector.

5. Compute the velocity component in the x direction $v_x(t_1)$ at the crossing.

6. Check if $|v_x(t_1)| < tol$, where tol is your desired accuracy. An exact perpendicular crossing is supposed to possess $v_x(t_1) = 0$. If the tolerance is not satisfied go to the next step, otherwise quit the procedure.

7. Correct the initial velocity using the state transition matrix. So the correction is equal to

$$\delta v_{y_0} \approx \left(\Phi_{34} - \frac{1}{v_y(t_1)} \Phi_{24} \right)^{-1} v_x(t_1) \quad ,$$

where Φ_{ij} is the element of the state transition matrix at the row i and column j.

Unfortunately the differential correction alone works properly for small amplitude orbits, as the linear approximation does. To extend the algorithm to very non-linear orbits the differential correction shall be coupled with another procedure known as numerical continuation. This allows to reach large amplitude orbits gradually increasing the energy level. Basically, the steps of the numerical continuation are

1. Find two closed initial conditions for small periodic orbits $\boldsymbol{x_0}^{(1)}, \boldsymbol{x_0}^{(2)}$.

2. Compute the difference $\boldsymbol{\Delta} = \boldsymbol{x_0}^{(2)} - \boldsymbol{x_0}^{(1)}$.

3. Extrapolate the initial guess for a larger orbit

$$\boldsymbol{x_g}^{(3)} = \boldsymbol{x_0}^{(2)} + \boldsymbol{\Delta} \quad .$$

4. Use differential correction to obtain a proper initial state $\boldsymbol{x_0}^{(3)}$.

5. Keep track of energy and repeat the procedure until the final energy level is achieved with the desired accuracy. Refinement steps may be required in the neighborhood of the solution.

In this work a simpler but not less effective method is adopted [65]. The complexity of two coupled algorithm can be overcome by the introduction of a Poincaré map. The Poincaré map is a surface of section S of the flow generated by a n-dimensional system. It is obtained by fixing certain variables so that the order of the problem is reduced. Then, the map is

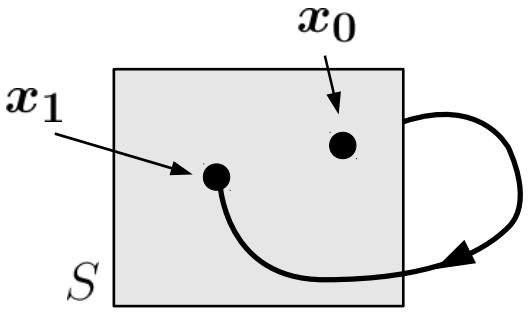

Figure 2.3: Surface Section S intercepting in $\boldsymbol{x}_1$ the flow generated by $\boldsymbol{x}_0$.

generated by emanating trajectories from S and intersecting the flow with the surface again, as in Figure 2.3. The system (2.9) defines a four dimensional flow in the state variables $(x, y, \dot{x}, \dot{y})$. To target the periodic orbit, the perpendicular crossing condition is still sought. Therefore, it appears logical to slice the flow on the x-axis, which means fixing $y = 0$. In this case, the surface of section S has a real location in the configuration space, which is $y = 0$ indeed, but it is worth to stress that S could be generally located in all the hyper-space defined by the state variables. Following the selection of S, the flow of trajectories is generated imposing an orthogonal departure, that is achieved by $\dot{x}_0 = 0$. In addition, the Jacobi constant J can be arbitrarily settled and one of the initial state variables left is consequently derived. For the current purposes, $\dot{y}_0$ is the best option,

$$\dot{y}_0 = \sqrt{-(2\bar{U} + JC)} \quad .$$

Hence, the set of initial conditions that produces the flow is only parametrized in the initial position x_0, after that the energy level has been decided. So, the Poincaré map $\mathcal{M}$ is defined as

$$\mathcal{M} : (x_0, 0, 0, \dot{y}_0(x_0, J)) \rightarrow (x_1, 0, \dot{x}_1, \dot{y}_1) \quad .$$

For a periodic orbit shall be $\dot{x}_1 = 0$, that yields also to $x_1 = x_0$, $\dot{y}_1 = \dot{y}_0$. The initial conditions that evolve into a periodic orbit can be sought on $\mathcal{M}$, depicted as a 2D maps in the variables $(x_1, \dot{x}_1)$ (see Figure 2.4). One only needs to find where the maps cross $\dot{x}_1 = 0$: the corresponding value of x_1 belongs to a periodic orbit. As shown in Figure 2.4, the function has multiple zeros, it is up to the analyst to pick out the Lyapunov orbit. A bisection method may be applied to the map $\mathcal{M}$ near the selected zero to establish an accurate value of the Lyapunov orbit initial condition x_0. Figure 2.4 displays different periodic orbits (including the Lyapunov class) propagated from the zeros obtained from the map in Figure 2.5. Despite

the necessity of an human operator, the periodic orbits with the desired energy level can be addressed directly and quickly by this method, without any iterative process.

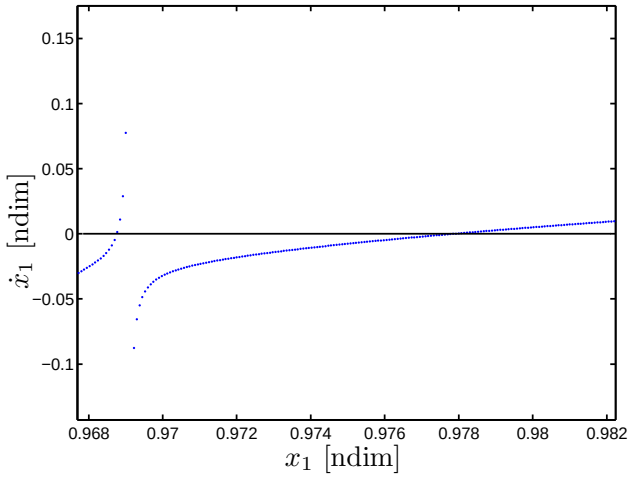

Figure 2.4: Visualization of the Poincaré map.

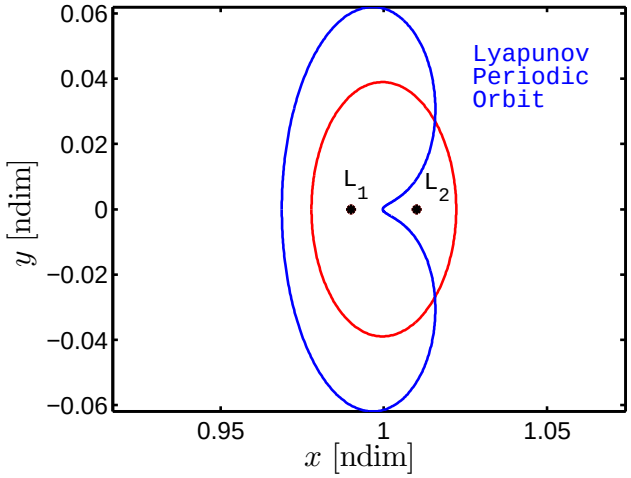

Figure 2.5: Possible periodic orbits in the Sun-Earth system (in *blue* a Lyapunov type orbit).

2.2 Large Space Structures Dynamics

As long as Large Space Structures (LSS) are considered, it is clear that the mass-point approximation or even the single rigid body model may

reveal inappropriate to describe accurately their dynamics. In fact, LSS are more correctly a distributed system and most likely consist in a set of interconnected entities and deployable appendages (such as antennas, solar arrays, deployable arms). Moreover, the inherent flexibility of both the single entities and the architecture as a whole may not be negligible. The importance of an adequate model of the problem is threefold:

1. Furnish a rational representation, necessary to understand the problem.

2. Serve as basis for numerical simulation of the problem.

3. Led to the successful prediction of the motions of the space vehicles.

Selecting the algorithm is anything but a trivial task; it frequently happens that the chosen procedure is so much complex, in terms of either the effort required to deliver the equations of motion or the final form of the equations their-selves, to be prohibitive [47]. Anyway, the general framework is represented by the analysis of Flexible Multi-Body System (FMS). Several approaches exists to address the dynamics of FMS (as discussed in the next Section), but basically any mechanical problem can be written in the well-known fashion

$$[M]\ddot{\boldsymbol{q}} + [K]\boldsymbol{q} = \boldsymbol{Q} + \boldsymbol{Q}_v(\boldsymbol{q}) \quad , \tag{2.23}$$

where $\boldsymbol{q}$ represents the set of generalized coordinates used to describe rigid translations and rotations as well as relative deformations, $[M]$ is the system mass matrix and $[K]$ denotes the stiffness matrix due to the energy built up in elastic deformation. $\boldsymbol{Q}_v$ is the quadratic velocity vector containing gyroscopic and Coriolis effects while $\boldsymbol{Q}$ are the generalized components of external actions. The matrix form of eq. (2.23) should be preferred in order to smooth the way for a numerical implementation. When specialized to the dynamics of large space structures, the model described by eq. (2.23) has the following characteristics:

- the mass matrix $[M(\boldsymbol{q})]$ depends on the generalize coordinates, due to variations of the moments of inertia.

- $[M]$ is a full matrix while $[K]$ works only for the sub-set of generalized coordinates describing elastic displacements.

- The generalized forces $\boldsymbol{Q} = \boldsymbol{Q}_g(\boldsymbol{q})$ result from the interaction with the gravity field as functions of body position, attitude and shape.

- The overall motion is described by large translations and rotations. On the contrary, the structure undergoes small deformations.

- Different dynamics coexist in the system: elastic fast dynamics versus orbital/attitude slow dynamics.

The aforementioned considerations suggest caution to numerically solve the motion. In fact, the variables to be integrated have significantly different order of magnitudes, from millimetric elastic displacements to an orbital radius of thousands of kilometers. Furthermore, a two-velocities dynamics is present. Thus, the problem may prove ill-conditioned and numerical instability may appear if proper integration schemes are not adopted. This will negatively affect the computational effort required. Here, it is worth to clarify how flexibility affects the orbital motion. Equations describing the rigid translational motion are coupled to elastic dynamics by two terms in eq. (2.23): the mass matrix $[M(\boldsymbol{q})]$ and the generalized gravity action $\boldsymbol{Q}_g(\boldsymbol{q})$. But the two terms originate a coupling of different meaning. The coupling due to the mass matrix $[M(\boldsymbol{q})]$ derives from the kinematics adopted (*i.e.* degrees of freedom and coordinate systems used) and can disappear according to a proper choice of the generalized coordinates $\boldsymbol{q}$. The coupling caused by $\boldsymbol{Q}_g(\boldsymbol{q})$ retains instead a physical nature: variations in the body shape can alter the resultant of gravity forces which governs the orbital motion.

2.2.1 Model Formulations

The procedure to deliver equations (2.23) is composed of the following steps (highlighted in Figure 2.6):

1. **Discretization of the Elastic Problem.** Once flexibility has been introduced the theoretical number of degrees of freedom (dofs) required to capture the spacecraft dynamics is boosted up to infinity. But for practical purpose accurate results may still be achieved by an adequate discretization of the elastic problem.

2. **Kinematics.** Several viable reference frames and their attendant independent coordinates can be implemented to describe the system configuration and its motion. Usually more choices are combined to attain the final representation. The kinematic approach selected is closely connected to the method adopted to discretize the elastic problem.

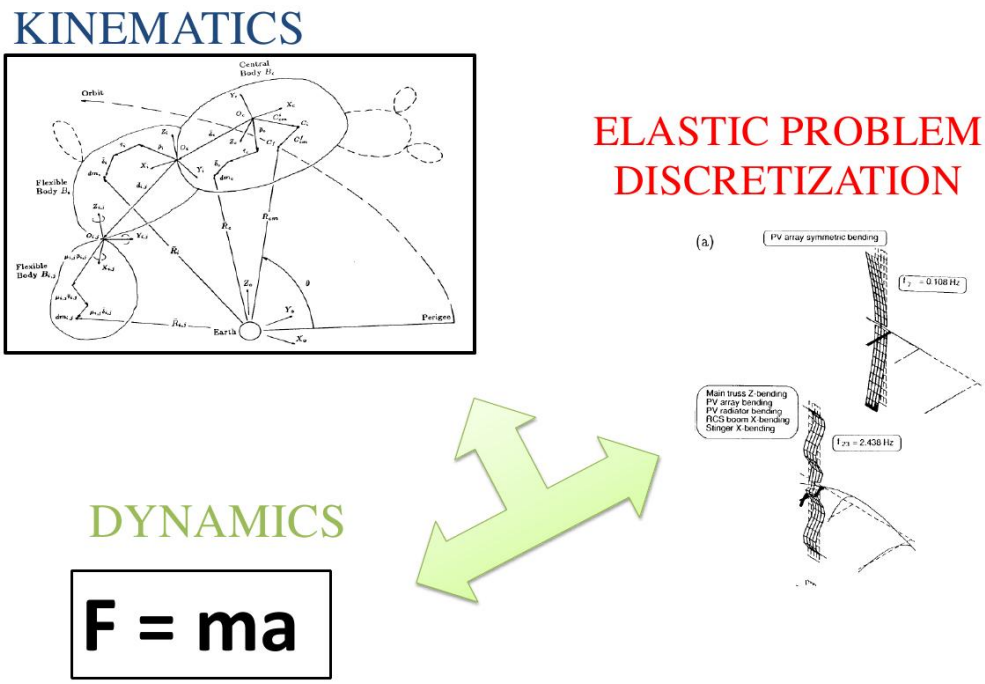

Figure 2.6: Model Formulation Framework (*upper* and *right* insets from [16]).

3. **Dynamics.** A series of physical principles can be used to write the final equations of motion. Depending on the kinematics used certain approaches are more convenient than other.

2.2.2 Elastic Discretization

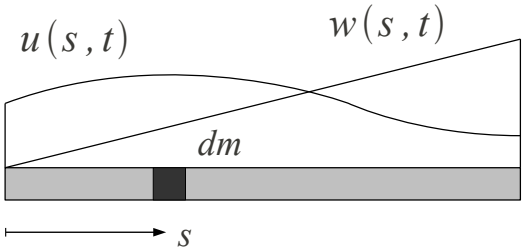

Figure 2.7: Diagram of the elastic displacement field on an elastic body.

As any infinitesimal mass point dm of a flexible structure moves independently from the others, the number of kinematic variables theoretically necessary to predict the motion is infinite. Thus, the displacement field

relative to the undeformed shape of the flexible body is better described by a continuous function $u(s,t)$, where s denotes the position of the dm as depicted in Figure 2.7 and t is the temporal instant. Even so, a mechanical problem ruled by differential equation like eq. (2.23) surely requires the computation of integrals written in a general fashion as

$$R = \int_V w(s,t)u^n(s,t)dV \quad , \tag{2.24}$$

with V representing the structure volume, u^n the nth spatial derivative of the displacement field $u(s,t)$ and $w(s,t)$ a generic weight function (as could be the body density, its elastic proprieties or the function $u^n(s,t)$ itself). Integrals like (2.24) are functions of the solution itself $u(s,t)$ of the differential problem, so they cannot be solved directly (the problem should be more correctly addressed as integro-differential). To that end, an approximation $\tilde{u}(s,t)$ of the solution $u(s,t)$ is employed instead. The approximation is built in order to reduce the number of elastic degrees of freedom to a finite value n_e (*i.e.* discretization) and split the temporal-spatial dependence of the elastic displacements $u(s,t)$ (*i.e.* variables separation). Different techniques are possible. Every method involves a different degree of accuracy as well as of arbitrariness left to the analyst. Basically, four wide classes of approximations are available (also listed in Table 2.1):

- **Finite Segment Method**. $u(s,t)$ and $w(s,t)$ are assumed to be a summation of delta-Dirac functions

  $$u(s,t) = \sum_i^{n_e} a_i(t)\delta_i(s - s_i) \quad .$$

  Physically, the structure considered as a distributed system transforms into a set of rigid bodies, springs and dumpers. This may be convenient since rigid bodies methodologies can be easily employed to formulate the equations of motions. On the other hand, the selection of the discrete parameters, such as springs stiffness, rigid bodies size and their location, may be a serious issue for the convergence and the accuracy of the method.

- **Ritz Method**. $u(s,t)$ is expressed as a linear composition of admissible functions $\psi_i(s)$ (referred as *shape functions*)

  $$u(s,t) = \sum_i^{n_e} a_i(t)\psi_i(s) \quad .$$

Admissible means that the functions used to represent the spatial variation of the elastic displacement have to respect the essential conditions of the problem. This reveals unsuited for complex geometry. The approximation usually adopted is a polynomial or trigonometric series. It should be considered that high order polynomials lead to ill-conditioning.

- **Modes Method**. It is the same as the Ritz method, but deserves a dedicated class because of the importance among the structural dynamics analysis methodologies. The sharp difference with the other method lies in the particular choice of the shape functions $\psi_i(s_i)$: the auto-solutions of the problem (*i.e.* modes) are selected. According to the essential conditions and the modeling criteria, either normal or constrained modes are used as well as global or local. The severity of this approach may rely on the modal shapes that rarely are known as analytical expressions but more likely have to be computed numerically.

- **FEM**. A breakthrough in structural analysis is beyond doubt the advent of the Finite Elements Method in the last century. Instead of evaluating the integral (2.24) along the entire domain, it is approximated as the summation of the same integral on smaller sub-domains (*i.e.* elements)
$$R = \sum_V \int_{V_i} w_i(s) u_i^n(s,t) dV_i \quad .$$
In the same way, also $u(s,t)$ is approximated using shape function $\psi_i(s)$ defined just on the single sub-domain. The shape functions largely adopted on the sub-domains are the interpolation polynomials of the displacements in points belonging to the element itself (*i.e.* nodes). The success of the FEM was due to the ability to solve geometry of arbitrary complexity while automatically satisfying the essential conditions.

All the classes previously reported are equally applicable to linear problems. On the contrary, limitations to their validity occur when non-linear effects are introduced in terms of both large rigid motions or large deformations. Spacecrafts naturally experience rigid translations and rotations. Furthermore, highly flexible large space structures may prove false the assumption of small deformations underlying the linear structural theory. Therefore, it is worth to carefully examine the circumstances where the elastic model is used. Here, it should be highlighted that the FEM formulation is particularly sensitive to the former kind of non-linearity: some

Table 2.1: Discretization Methods of the Elastic Problem.

METHOD	DISCRETIZATION	NOTES
Finite Segment Method	Rigid Bodies connected by Springs or Dumpers	1) Rigid Bodies Methodologies. 2) Problem of selection of number, size and position of Rigid Bodies. 3) Inertia Coupling.
Ritz	Series: trigonometric/polynomial	1)Require admissible functions. 2)High order polynomial may lead to ill-conditioning. 3) Unsuited for complex domains.
Modes	Normal/Constrained and Local/System Modes	1) Require to be previously computed (analytical forms are known only simple cases).
FEM	Finite Elements + Shape Functions	1) Infinitesimal displacements. 2) Not exact modeling of rigid body motion.

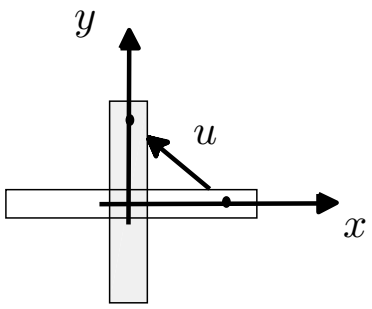

Figure 2.8: Sketch of a 90 degrees rigid rotation of the element.

elements are not able to exactly predict rigid motion and non-zero strain appears during an arbitrary rigid displacement. For instance, image an element undergoing a 90 degrees rigid rotation like in Figure 2.8. Assuming linear shape functions to represent the element relative motion, the rigid rotation would result as

$$\begin{cases} u_x = y - x \\ u_y = x - y \end{cases}, \tag{2.25}$$

but when computing the strain on the element

$$\begin{cases} \varepsilon_x = u_{x/x} = -1 \\ \varepsilon_y = u_{y/y} = -1 \end{cases}, \tag{2.26}$$

a non-zero field comes out, despite just a rigid motion has been imposed. One of the most popular procedure to solve non-linearities in the FEM is known as *incremental finite element approach*. It basically considers consequent configurations of the structure close enough to remain in the limit of small displacements (regardless they are due to rigid motions or deformations, so it is applicable to different kinds of non-linearities). Then, the solution is approached iteratively. Nonetheless, the representation of rigid motion is still an approximation in many incremental formulations, especially when the structure rotates as a rigid body [66]. Thus, different efforts, as discussed briefly in the next section, have been done to seek kinematics variables able to exactly track rigid translations and rotations.

2.2.3 Kinematics

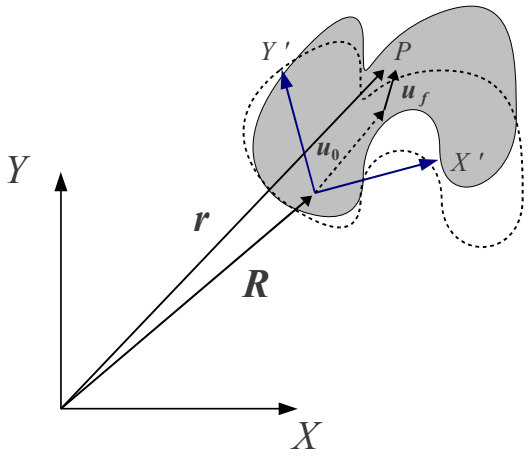

Figure 2.9: Floating Frame (in blue) and its attendant location vectors.

No better introduction for this section than the words of Shabana [19]:

"*The shape of deformation of the body is defined in its coordinate system, and as a consequence, the selections of the deformation shapes and the body coordinate system cannot be considered as two independent issues*".

In fact, the selection of discrete generalized coordinates to reproduce the elastic deformation naturally affects the choice of the local reference system, and vice versa. The most widely adopted formulation in the flexible multi-body dynamics is currently the *Floating Frame* [19]. The *Floating Frame* is the same kinematics framework generally adopted to describe the

rigid body dynamics and that is also the likely reason of its success. Different formulations of the *Floating Frame* are possible, but all are based on two set of coordinates: one set defines the location and the orientation of a local body coordinate system (*i.e.* the *Floating Frame*), while the second represents elastic displacement relative to the local body reference previously defined. According to this description, with reference to Figure 2.9, the global position vector $\boldsymbol{r}$ of an arbitrary point on a deformable body can be written as [67]:

$$\boldsymbol{r} = \boldsymbol{R} + [A](\boldsymbol{u}_0 + \boldsymbol{u}_f) \quad , \tag{2.27}$$

where $\boldsymbol{R}$ is the vector locating the *Floating Frame* and $[A]$ is the rotation matrix that defines its attitude; $\boldsymbol{u}_0$ and $\boldsymbol{u}_f$ refer respectively to the undeformed position in the *Floating Frame* and the elastic displacement in the last mentioned frame. It should be stressed that the *Floating Frame* formulation leads to the exact description of completely rigid motions. It is also worth to mention that there is no guarantee of separation between rigid and flexible dynamics with this approach. The possible decoupling depends on the selected local body reference. Many investigations in flexible body dynamics addressed a coordinate system that minimize the relative kinetic energy with respect to an observer stationed on the body [19]. Thus, the rigid and elastic dynamics result weakly coupled. The set of coordinates that minimizes the coupling are known as *mean axis* [68].

Otherwise, especially along with the FEM, a *convected coordinate system* is employed. In this approach the kinematics variables are defined in the element reference frame with the further assumption that the element coordinate system remains fixed despite the motion of the element itself. Shape functions used to describe general displacements are clearly unable to capture large rotation if defined in such a frame. The *convected coordinate system* was born in the context of static analysis under the assumptions of the linear structural theory and it is not proper for structures, like spacecrafts, undergoing large motions. Therefore, different attempts were prosecuted to develop a kinematic formulation able to bring the computation power of the FEM into the multi-body dynamics. A set of different coordinate reference system may be thought to overcome the issue [69, 66]. Briefly, the set should consist of a global fixed frame, a body frame (similar to the *floating frame*), a intermediate element frame whose origin is the same as the previous body frame and finally the usual element frame. To avoid using so many frames, element nodal coordinates may be defined in the global coordinate system and large rotation vectors could be used to identify the element configuration [70, 34, 71]. But, as pointed out in [19] this kind of formulation can lead to singularity problems. Finally a

Table 2.2: Kinematics Approaches.

METHOD	REFERENCES	NOTES
Floating Reference	Modi, Misra et al. (1978) [17]	Two sets of coordinates are used: 1) one set describes the location and the orientation of an arbitrary body coordinate system (*i.e* the floating frame), 2) another set describes the deformations w.r.t. the floating frame.
Direct Path	Ho (1977) [22]	Vectorial oriented path from the main body directly toward the appendages.
Rotationally Fixed Floating Frame	Vu-Quoc,Simo (1987) [33]	The floating reference is a translational frame parallel to the inertial one, placed in the instantaneous center of mass.
Convected Coordinate System		Associated to the incremental finite element approach. Kinematics equations are defined in the element coordinate system.
Large Rotator Vectors	Vu-Quoc,Simo (1980) [34]	Avoid displacements linearization. Element nodal coordinates are expressed w.r.t. the global coordinate system.
Absolute Nodal Coordinate	Shabana (1997) [19]	Absolute displacements and global slopes are used as the element coordinates.

more recent approach, named *absolute nodal coordinates*, suggests to use as nodal coordinates neither infinitesimal nor finite rotations. Instead, absolute displacements and global slopes are selected as kinematics variables [72, 73, 67]. This method employs geometrically exact non-linear strain theories and is applicable to structures undergoing large overall displacements regardless their origin, either rigid or elastic. Methods discussed in this Section are summarized in Table 2.2, where also references to two other more specific formulation are accounted.

2.2.4 Dynamics

Basically, eigth approaches yield to the equations of motion of a mechanical system [47, 48]:

1. *Newton-Euler equations*. Derived from the use of momentum principles. They describe the combined translational and rotational dynamics of a rigid body.
2. *D'Alembert principle*. It introduces forces generated by the inertial acceleration of every single particles. Considering these so-called inertia forces along with the other actions the system always appears as null system.
3. *Lagrange procedure*. The evolution of the system is described by the solutions to the Euler–Lagrange equations.
4. *Hamilton's canonical equations*. The Hamiltonian function is used to derive the equations of motion.
5. *Virtual works*. Weak formulation of the problem. Based on the equivalence of virtual works.
6. *Boltzmann-Hamel equations*. Similar to Lagrange procedure, but the dependent variables are not constrained to the form of generalized coordinates.
7. *Gibbs method*. Based on the Gibbs' equations. It offers the same advantages of the Boltzmann-Hamel algorithm, but the procedure is simpler and much more systematic.
8. *Kane's method*. Based on the projection of forces and torques along the directions defined by the "partial velocity" and "partial angular velocity" vectors. It claims to be the most direct method to achieve the simplest equations form.

Table 2.3: Common drawbacks of the dynamics formulations.

ISSUE	METHODS
Non-automatic elimination of constrain/non-contributing forces and moments	Newton-Euler, D'Alembert principle
Operationally challenging	Virtual works
Lengthy scalar functions	Lagrange, Hamilton, Boltzmann-Hamel, Gibbs
Limited choice of independent variables	Lagrange, Hamilton
Direct final equations not in the simplest form	Lagrange, Hamilton, Boltzmann-Hamel

Despite based on different principles, the aforementioned methods eventually lead to the same dynamics. It is straightforward to see that it could not be otherwise. Even so, the methods are not equivalent at all. In fact, many practical issues may arise while following some of those procedures for complex systems: multiple intermediate steps may be required and make the algorithm extremely long, equations may turn out to be too complex to be handled, final expressions or selected variables may retain an obscure meaning. While choosing a dynamics formulation, one needs to be aware of the following aspects at least:

1. The number of steps required to deliver the final equations.
2. The length and the complexity of the expressions to be handled (sometimes even symbolic manipulator run out of their memory).
3. The meaning of the kinematics variables adopted, as well as of the expressions encountered during the procedure.
4. The effort required to numerically implement the algorithm.

Table 2.3 summarizes some drawbacks frequently faced using the methods here recalled. The aspects enumerated should be firstly considered, but according to the specific problem addressed other issues may reveal as important as those here mentioned. For instance, the readiness of the algorithm for the control design, the direct availability of integral of motions or simply the familiarity of the analyst with some procedures are other indexes to select the proper formulation.

3 Formulation for the Rigid Fully-Coupled Motion

Contents

In this Chapter the formulation adopted to reproduce the planar dynamics of large rigid space structures in the vicinity of libration points is presented. In the first Section, the coordinate reference systems and the kinematics variables are introduced. The kinematics is based on the floating reference method mentioned in the previous Chapter. Secondly, the last Section reports the procedure used to derive the equations of motion. These equations are obtained in the Euler-Lagrange form and are successively manipulated accordingly to the Encke's Method.

3.1 Kinematics

In this work the dynamics of Large Space Structures (LSS) on planar Lyapunov periodic orbits is investigated within the framework of the Circular Planar Restricted Three-Body Problem (CPR3BP). Further details about the CPR3BP or the computational procedure of the periodic orbits have been presented in the previous Chapter. Before addressing directly the development of the equations of motion, the kinematics framework deserves to be

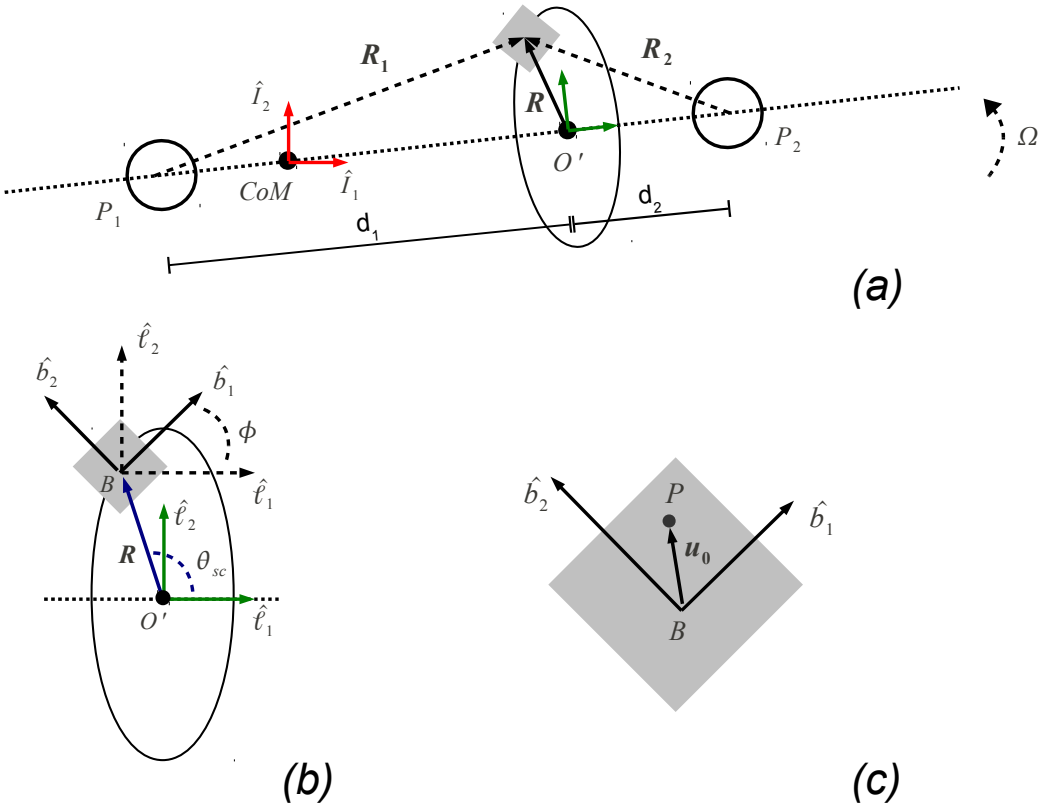

Figure 3.1: Kinematic Representation. *(a)* Global frames and vectors. *(b)* Body frame location and orientation. *(c)* Local position vector.

explained. In order to identify the position and the attitude of a spacecraft, as well as its linear and angular velocity, different sets of frames can be employed, as shown in the second part of Chapter 2. The choice of the kinematic degrees of freedom should consider the effort to deliver the differential equations of motion in such variables as well as the meaning that they might possess, in order to reduce the cost of both producing and interpreting results. Presently dealing with rigid bodies, the adoption of the Floating Frame it is straightforward. But considering that also deformable structures in space undergo mainly large translations and rotations, it will prove to be a convenient choice also when flexibility is incorporated. In the Floating Frame formulation basically two coordinate systems have to be defined: a global system is used to describe the body position and a local system to track the body attitude. To properly define these coordinate systems in the PCR3BP more reference frames are introduced and below explained.

For sake of clarity, each coordinate systems mentioned is identified by a letter, and the attendant versors by the same letter with a proper subscript: so the X-frame will be established by the $(\hat{x_1}, \hat{x_2}, \hat{x_3})$ tern of versors. Firstly, a inertial frame denoted as I-frame is fixed in the center of mass of the planetary system. The $\hat{I}_1$ versor of the I-frame is initially aligned with the axis through the primary P_1 and the secondary P_2, but the I-frame does not rotate with the planetary system. The ℓ-frame rotates instead. The ℓ-frame at the time $t = 0$ is oriented as the I-frame, but its origin O' is located on the libration point, L_1 or L_2 accordingly to the Lyapunov periodic orbit considered. Then, the ℓ-frame rotates with the planetary system angular velocity Ω, so that the $\hat{\ell}_1$ versor always matches with the $P_1 - P_2$ line, and translates maintaining its origin attached to the libration point. The ℓ-frame represents the global coordinate system for the Floating Frame formulation, so it is also intended for being the common vector basis. Finally, the local coordinate system, referred as b-frame, is attached to a general point B. The origin B of the b-frame does not necessarily belong to the body, or equivalently B it is not needed to have mass. The point, where the floating frame is attached, has only to retain a constant position with respect the undeformed mass distribution. In a similar way, the undeformed mass distribution must appear still if observed in the b-frame. Hence, the attitude of the body is defined via the b-frame by the angle ϕ, which is the angle of rotation between the local coordinate system and the global coordinate system. Throughout this work, only the planar dynamics in the orbital plane of the two attractors is addressed, so a single angle is sufficient to define the orientation of the spacecraft. The angle ϕ will be also referred as pitch angle or simply pitch. Figure 3.1 depicts all the coordinate systems presented.

Thus, the position of an infinitesimal mass dm in the point P is defined in the ℓ-frame (*i.e.* the global coordinate system) by the vector

$$\boldsymbol{r}_P = \boldsymbol{R} + [A]\boldsymbol{u}_0 \quad , \tag{3.1}$$

where $\boldsymbol{R}$ is the position vector of the origin B of the b-frame (*i.e.* the local coordinate system), $\boldsymbol{u}_0$ is the undeformed position vector of P in the b-frame and $[A]$ stands for the rotation matrix from the b-frame to the ℓ-frame. This matrix appears as

$$[A] = \begin{bmatrix} \cos\phi & -\sin\phi \\ \sin\phi & \cos\phi \end{bmatrix} \quad . \tag{3.2}$$

Since the body is assumed rigid, the only generalized coordinates $\boldsymbol{q}$ necessary to describe the motion are the rigid set $\boldsymbol{q}_r$, which defines the position

and the orientation of the b-frame. So

$$\boldsymbol{q} = \begin{bmatrix} \boldsymbol{q}_r \end{bmatrix} = \begin{bmatrix} \boldsymbol{R} \\ \phi \end{bmatrix} \quad . \tag{3.3}$$

It is also important to be able to write the temporal derivative of the position vector, in order to later develop the kinetic energy of the body,

$$\dot{\boldsymbol{r}}_P = \dot{\boldsymbol{R}} + [\dot{A}]\boldsymbol{u}_0 \quad , \tag{3.4}$$

with

$$[\dot{A}] = \dot{\phi}[A]_{/\phi} \quad .$$

The subscript $_{/\bullet}$ denotes the derivative relative to the variable $\bullet$. Finally, as stressed by Shabana in [67], some integral quantities are function of the distribution of mass, but do not depend on the generalized coordinates $\boldsymbol{q}$. It means that such integrals can be computed in advance of the solution of the dynamics and will remain constant parameters of the problem for a given mass configuration. That propriety will be particularly useful when the deformations of the body will be accounted in Chapter 6. Shabana named these quantities Inertia Shape Integrals. The Inertial Shape Integrals for a rigid body are

$$[I_1] = \int_V \rho \boldsymbol{u}_0 \, dV \tag{3.5}$$

and

$$I_{00} = \int_V \rho \boldsymbol{u}_0^T \boldsymbol{u}_0 \, dV \quad . \tag{3.6}$$

It is worth to recall that the vector $[I_1]$ is null when the origin B of the b-frame is fixed to the body center of mass.

3.2 Dynamics

In this Section the fully-coupled equations of motion for a spacecraft orbiting in the vicinity of libration points are delivered via the Lagrangian procedure. Firstly, all the terms present in the Lagrangian function $\mathcal{L}$ of the system are derived; secondly, the equations of motions obtained are rearranged using the Encke's method.

The following motivations support choice of adopting the Lagrangian procedure among the seven methods presented in the previous Chapter:

- Widely implemented and large author's experience using this method.

- Clear physical meaning in terms of contributing forces.
- Readily amenable to stability study and well suited for control design.

Thus, the Lagrangian function of the system is

$$\mathcal{L} = T_{rel} + T_1 + T_2 - U_1 - U_2 \quad , \tag{3.7}$$

where T_{rel} is the kinetic energy of the body as observed in the ℓ-frame and U_1, U_2 denote the gravitational potential due to the fields generated from the primary and the secondary; the terms T_1 and T_2 are the generalized potential of the fictitious forces (respectively the centrifugal and the Coriolis force) that are observed in the ℓ-frame. As it should be clear, the global coordinate system adopted is not an inertial reference (since it rotates with a constant angular velocity Ω and also possesses a translational acceleration).

To study the dynamics of LSS incorporating the effect of a finite dimensional mass distribution, the gravitational potential has to be properly formulated. Considering the field generated by the attractor P_x (where the subscript $x = 1, 2$ is adopted to address respectively the primary or the secondary), the general expression for the gravitational potential is

$$U_x = -\mu_x \int_V \frac{\rho(\boldsymbol{r}_x)}{|\boldsymbol{r}_x|} dV \quad , \tag{3.8}$$

where μ_x is the planetary gravitational constant of P_x, ρ is the mass density, V is the undeformed volume of the mass configuration and $\boldsymbol{r}_x$ is the position vector of the infinitesimal mass $dm = \rho dV$ relative to the attractor P_x. In classical orbital mechanics the integral in eq. (3.8) is solved assuming $\boldsymbol{r}_x$ constant over the volume of integration and equal to the center of mass position. This assumption also implies the followings:

- the vehicle is represented as a zero-dimensional mass-point; the whole mass of the configuration is collapsed in its center of mass.
- The spacecraft center of mass corresponds to its center of gravity.

Otherwise, dropping these assumptions, there is no close solution of eq. (3.8) for a body with arbitrary topology. Thus, the argument of the integral $1/|\boldsymbol{r}_x|$ is expanded in Taylor series in order to resolve the gravitational potential of the configuration in a close form. Firstly, $\boldsymbol{r}_x$ is expressed as the sum of two components: the position vector of a reference point $\boldsymbol{r}_0$ and the small variations vector $\boldsymbol{\delta r}$ with respect to the reference,

$$\boldsymbol{r}_x = \boldsymbol{r}_0 + \boldsymbol{\delta r} \quad .$$

Then $1/|\boldsymbol{r}_x|$ is expanded around $\boldsymbol{r}_0$ up to terms of the second order

$$\frac{1}{|\boldsymbol{r}_x|} \cong \frac{1}{|\boldsymbol{r}_0|} + \frac{\boldsymbol{\delta r} \cdot \hat{\boldsymbol{r}}_\mathbf{0}}{|\boldsymbol{r}_0|^2} + 3\frac{(\boldsymbol{\delta r} \cdot \hat{\boldsymbol{r}}_\mathbf{0})^2}{|\boldsymbol{r}_0|^3} - \frac{(\boldsymbol{\delta r} \cdot \boldsymbol{\delta r})}{|\boldsymbol{r}_0|^3} \quad . \tag{3.9}$$

with

$$\hat{\boldsymbol{r}}_\mathbf{0} = \frac{\boldsymbol{r}_0}{|\boldsymbol{r}_0|} \quad .$$

The second order is the lowest possible to introduce changes in the gravitational potential as consequence of an extended distribution of mass. Given the kinematic framework earlier presented, $\boldsymbol{r}_0$ can be expressed as

$$\boldsymbol{r}_0 = \boldsymbol{R}_x \quad ,$$

where $\boldsymbol{R_x}$ is the vector drawn from the attractor P_x to the origin B of the b-frame, while $\boldsymbol{\delta r}$ is equal to

$$\boldsymbol{\delta r} = [A]\boldsymbol{u}_0 \quad .$$

It yields to the Taylor series written in the adopted kinematic variables

$$\frac{1}{|\boldsymbol{r}_x|} \cong \frac{1}{|\boldsymbol{R}_x|} - \frac{\boldsymbol{u}_0^T[A]^T\hat{\boldsymbol{R}}_x}{|\boldsymbol{R}_x|^2} + \frac{3}{2}\frac{(\boldsymbol{u}_0^T[A]^T\hat{\boldsymbol{R}}_x)^2}{|\boldsymbol{R}_x|^3} - \frac{1}{2}\frac{\boldsymbol{u}_0^T[A]^T[A]\boldsymbol{u}_0}{|\boldsymbol{R}_x|^3} \quad , \tag{3.10}$$

with

$$\hat{\boldsymbol{R}}_x = \frac{\boldsymbol{R}_x}{|\boldsymbol{R}_x|} \quad .$$

Substituting the expansion (3.10) into eq. (3.8) and solving the integral, the general expression of the gravitational potential for a body with total mass m becomes

$$U_x(\boldsymbol{R}_x) = -\mu_x \left[\frac{m}{|\boldsymbol{R}_x|} - \frac{1}{|\boldsymbol{R}_x|^2}\boldsymbol{l}_x^T[I_1] - \frac{1}{2}\frac{1}{|\boldsymbol{R}_x|^3}I_{00} + \frac{3}{2}\frac{1}{|\boldsymbol{R}_x|^3}\boldsymbol{l}_x^T[JJ_{00}]\boldsymbol{l}_x\right] \tag{3.11}$$

where it has been introduced the director cosine of $\boldsymbol{R}_x$ in the b-frame

$$\boldsymbol{l}_x = [A]^T\hat{\boldsymbol{R}}_x$$

and a new inertia shape integral

$$[JJ_{00}] = \int_V \rho\boldsymbol{u}_0\boldsymbol{u}_0^T\,dV \quad . \tag{3.12}$$

The overall gravitational field caused by two attractors P_1 and P_2 is finally represented by the potential

$$U = U_1(\boldsymbol{R}_1) + U_2(\boldsymbol{R}_2) \quad . \tag{3.13}$$

The relative kinetic energy with respect to an observer on the ℓ-frame is

$$T_{rel} = \frac{1}{2}\int_V \rho \dot{\boldsymbol{r}}_P^T \dot{\boldsymbol{r}}_P dV \quad . \tag{3.14}$$

Substituting the expression (3.4) for $\dot{\boldsymbol{r}}_P$ and resolving the integral in eq. (3.15), the kinetic energy is rearranged as function of the derivative of the generalized coordinates $\dot{\boldsymbol{q}}$

$$T_{rel} = \dot{\boldsymbol{q}}^T [M] \dot{\boldsymbol{q}} \quad , \tag{3.15}$$

where

$$[M] = \begin{bmatrix} m_{RR} & m_{R\phi} \\ \text{symm.} & m_{\phi\phi} \end{bmatrix} \tag{3.16}$$

is the mass matrix of the system, which is a symmetric matrix. The components of $[M]$ are defined as

$$\begin{aligned} m_{RR} &= \int_V \rho [I]\, dV \\ m_{\phi\phi} &= [I_{00}] \\ m_{R\phi} &= [A]_{/\phi} [I_1] \end{aligned}$$

where $[I]$ denotes the identity matrix.

So far, only the generalized potential of the fictitious forces remains in order to be derived to complete the Lagrangian function of the system (3.7). As already mentioned, the ℓ-frame used as a common basis of the generalized coordinates is not an inertial reference. Therefore, each point P of the spacecraft observed from the inertial coordinate system I-frame possesses a further component of velocity besides the relative term $\dot{\boldsymbol{r}}_P$, noticeable in the ℓ-frame. As the principles of dynamics hold true only in a inertial coordinate system, it is necessary to account this discrepancy when the equations of motion are delivered on the basis of a non-inertial reference. The further component of the velocity vector provoked by the motion of the ℓ-frame relative to the I-frame results as

$$\boldsymbol{v}_T(P) = \boldsymbol{v}(O') + \boldsymbol{\omega} \wedge \boldsymbol{r}_P \quad , \tag{3.17}$$

where $\boldsymbol{v}(O')$ and $\boldsymbol{\omega}$ are respectively the translational and angular velocity vectors of the ℓ-frame relative to an inertial coordinate system. For convenience in handling the following developments, the cross product in eq.

(3.17) can be turned into a matrix form

$$\boldsymbol{\omega} \wedge \boldsymbol{r}_P = \begin{bmatrix} 0 & -\omega_z & -\omega_y \\ \omega_z & 0 & -\omega_x \\ -\omega_y & \omega_x & 0 \end{bmatrix} \boldsymbol{r}_P = [\tilde{\omega}]\boldsymbol{r}_P \quad , \tag{3.18}$$

where a planar dynamics yields to

$$\boldsymbol{\omega} = \begin{bmatrix} 0 \\ 0 \\ \Omega \end{bmatrix}$$

and

$$[\tilde{\omega}] = \begin{bmatrix} 0 & -\Omega \\ \Omega & 0 \end{bmatrix} \quad .$$

Hence substituting eq. (3.18) in eq. (3.17) and making explicit $\boldsymbol{r}_P$, it gives

$$\boldsymbol{v}_T(P) = \boldsymbol{v}(O') + [\tilde{\omega}]\boldsymbol{R} + [\tilde{\omega}][A]\boldsymbol{u} \tag{3.19}$$

The expression (3.19) is used to compute the generalized fictitious potential $T_1 + T_2$. Firstly, T_1 is generally defined as

$$T_1 = \frac{1}{2}\int_V \rho \boldsymbol{v}_T^T \boldsymbol{v}_T \, dV \quad . \tag{3.20}$$

Inserting the expression (3.19) in the former equation, after some algebra, the generalized potential representing the centrifugal action appears as

$$\begin{aligned} T_1 \;=\; & \frac{1}{2} m \boldsymbol{v}(O')^T \boldsymbol{v}(O') \;+\; m \boldsymbol{v}(O')^T [\tilde{\omega}]\boldsymbol{R} \;+\; \boldsymbol{v}(O')^T [\tilde{\omega}][A] I_1 + \frac{1}{2}\Omega^2 m \boldsymbol{R} \\ & + \Omega^2 \boldsymbol{R}^T [A] I_1 \;+\; \frac{1}{2}\Omega^2 I_{00} \quad . \end{aligned} \tag{3.21}$$

Secondly, T_2 is generally defined as

$$T_2 = \int_V \rho \dot{\boldsymbol{r}}_P^T \boldsymbol{v}_T \, dV \quad . \tag{3.22}$$

As previously, by inserting the expression (3.19) in the definition of T_2, after some algebra, the generalized potential representing the Coriolis action appears as

$$\begin{aligned} T_2 \;=\; & m \dot{\boldsymbol{R}}^T \boldsymbol{v}(O') \;+\; m \dot{\boldsymbol{R}}^T [\tilde{\omega}] \dot{\boldsymbol{R}} + \dot{\boldsymbol{R}}^T [\tilde{\omega}][A] I_1 \\ & + I_1^T [\dot{A}]^T (\boldsymbol{v}(O') + [\tilde{\omega}]\boldsymbol{R}) \;+\; \Omega \dot{\phi} I_{00} \quad . \end{aligned} \tag{3.23}$$

Given the Lagrangian function of the system $\mathcal{L}$ in eq. (3.7), the motion of the spacecraft depicted by the generalized coordinates $\boldsymbol{q}$ is the solution of the well-known Lagrange-Euler equations

$$\begin{aligned} \frac{d}{dt}\left(\frac{\partial T_{rel}}{\partial \dot{\boldsymbol{q}}}\right) - \frac{\partial T_{rel}}{\partial \boldsymbol{q}} &= -\frac{\partial U}{\partial \boldsymbol{q}} + \frac{\partial T_1}{\partial \boldsymbol{q}} \\ & \frac{\partial T_2}{\partial \boldsymbol{q}} - \frac{d}{dt}\left(\frac{\partial T_2}{\partial \dot{\boldsymbol{q}}}\right) \quad , \end{aligned} \tag{3.24}$$

that can be presented in a more compact fashion as

$$[M]\ddot{\boldsymbol{q}} = \boldsymbol{Q}_\nu + \boldsymbol{Q}_g + \boldsymbol{Q}_\Omega \quad , \tag{3.25}$$

where $\boldsymbol{Q}_\nu$ is the so called quadratic velocity vector [67]

$$\boldsymbol{Q}_\nu = \begin{bmatrix} (Q_\nu)_R \\ (Q_\nu)_\phi \end{bmatrix} = [M]\ddot{\boldsymbol{q}} - \frac{d}{dt}\left(\frac{\partial T_{rel}}{\partial \dot{\boldsymbol{q}}}\right) + \frac{\partial T_{rel}}{\partial \boldsymbol{q}} \quad , \tag{3.26}$$

$\boldsymbol{Q}_g$ is the action caused by the gravitational field

$$\boldsymbol{Q}_g = \begin{bmatrix} (Q_g)_R \\ (Q_g)_\phi \end{bmatrix} = -\frac{\partial U}{\partial \boldsymbol{q}} \tag{3.27}$$

and $\boldsymbol{Q}_\Omega$ is the action provoked by the fictitious accelerations

$$\boldsymbol{Q}_\Omega = \begin{bmatrix} (Q_\Omega)_R \\ (Q_\Omega)_\phi \end{bmatrix} = +\frac{\partial T_1}{\partial \boldsymbol{q}} + \frac{\partial T_2}{\partial \boldsymbol{q}} - \frac{d}{dt}\left(\frac{\partial T_2}{\partial \dot{\boldsymbol{q}}}\right) \quad . \tag{3.28}$$

The notation $(V)_\bullet$ simply stands for the components of the vector $\boldsymbol{V}$ related to the equations describing the dynamics $\bullet$, where $\bullet = R$ denotes the orbital motion and $\bullet = \phi$ the attitude motion.

In the orbital motion it is straightforward to expect the perturbation induced by the mass distribution to be extremely small if compared to the gravitational forces on the center of mass. Therefore, the numerical integration of the overall motion as stated in eq. (3.25) would result in a very poor accurate picture of the phenomena investigated. In fact, the problem formulated in the fashion of eq. (3.25) is dominated by the dynamics of zero order (*i.e.* the spacecraft collapsed in its center of mass), making almost impossible to discern dynamics of higher order (*i.e.* perturbed motions due to extended mass configuration of the spacecraft) from integration errors. To overcome this issue, the Encke's method is implemented [74]. The basic idea of the Encke's method is to assume known the unperturbed dynamics and subtract such motion from the overall problem,

in order to emphasize the perturbing effects on a reference trajectory. It is also assumed that the nominal and the actual trajectory correspond at the initial instant $t = 0$ (for this reason the reference trajectory will be also referred as osculating orbit). To begin with, the orbital equations of motion are extracted from the system (3.25)

$$[m_{RR}]\ddot{\boldsymbol{R}} + [m_{R\phi}]\ddot{\phi} = (\boldsymbol{Q}_\nu)_R + (\boldsymbol{Q}_g)_R + (\boldsymbol{Q}_\Omega)_R \quad , \tag{3.29}$$

then such equations are specialized for the zero order dynamics

$$[m_{RR}]\ddot{\boldsymbol{R}}_0 = -\frac{\partial U^0}{\partial \boldsymbol{R}_0} + \frac{\partial T_1^0}{\partial \boldsymbol{R}_0} + \frac{\partial T_2^0}{\partial \boldsymbol{R}_0} - \frac{d}{dt}\left(\frac{\partial T_2^0}{\partial \dot{\boldsymbol{R}}_0}\right) = (\boldsymbol{Q}_\nu)_{R_0} + (\boldsymbol{Q}_g)_{R_0} + (\boldsymbol{Q}_\Omega)_{R_0} \quad . \tag{3.30}$$

Naturally, eq. (3.30) are equivalent to those governing the PCR3BP and the solution $\boldsymbol{R}_0(t)$ represents the reference trajectory (that in this work will be a Lyapunov periodic orbit in vicinity of the Lagrangian points). Let's now introduce the displacement of the perturbed motion from the osculating orbit

$$\boldsymbol{\delta} = \boldsymbol{R} - \boldsymbol{R}_0 \tag{3.31}$$

and its second time derivative

$$\ddot{\boldsymbol{\delta}} = \ddot{\boldsymbol{R}} - \ddot{\boldsymbol{R}}_0 \quad . \tag{3.32}$$

Hence, subtracting eq. (3.30) from eq. (3.29) the problem is rearranged in such a way that the unknown of the system is the displacement vector $\boldsymbol{\delta}$

$$[m_{RR}]\ddot{\boldsymbol{\delta}} + [m_{R\phi}]\ddot{\phi} = (\boldsymbol{\delta Q}_\nu)_R + (\boldsymbol{\delta Q}_g)_R + (\boldsymbol{\delta Q}_\Omega)_R \quad . \tag{3.33}$$

The differential actions $(\boldsymbol{\delta Q_\bullet})_R$ appearing in the former equation are further developed in the following of the paragraph. Specifically, the differential quadratic velocity vector results in

$$(\delta Q_\nu)_R = \dot{\phi}^2[A][I_1] \tag{3.34}$$

and the differential gravity action appears as

$$(\delta Q_g)_R = -\left(\frac{\partial U_1}{\partial \boldsymbol{R}} - \frac{\partial U_1^0}{\partial \boldsymbol{R_0}}\right) - \left(\frac{\partial U_2}{\partial \boldsymbol{R}} - \frac{\partial U_2^0}{\partial \boldsymbol{R_0}}\right) \quad , \tag{3.35}$$

where

$$\left(\frac{\partial U_x}{\partial \boldsymbol{R}} - \frac{\partial U_x^0}{\partial \boldsymbol{R_0}}\right) = \mu_x \frac{m}{|\boldsymbol{R}_x^0|^3}(\boldsymbol{\delta} + f(h)\boldsymbol{R}_x) + \boldsymbol{a}_P^x \quad . \tag{3.36}$$

with

$$f(h) = h\frac{3 + 3h + h^2}{1 + (1 + h)^{3/2}} \quad , \tag{3.37}$$

$$h = \frac{\boldsymbol{\delta}^T\boldsymbol{\delta} - 2\boldsymbol{\delta}^T\boldsymbol{R}_x}{|\boldsymbol{R}_x|^2} \quad , \tag{3.38}$$

$$\begin{aligned}\boldsymbol{a}_P^x &= -\mu_x \left[\frac{2}{|\boldsymbol{R}_x|^3}\frac{\partial|\boldsymbol{R}_x|}{\partial\boldsymbol{R}}\boldsymbol{l}_x^T[I_1] - \frac{1}{|\boldsymbol{R}_x|^2}\left(\frac{\partial\boldsymbol{l}_x}{\partial\boldsymbol{R}}\right)^T[I_1] + \frac{3}{2}\frac{1}{|\boldsymbol{R}_x|^4}\frac{\partial|\boldsymbol{R}_x|}{\partial\boldsymbol{R}}I_{00} \right. \\ &\left. -\frac{9}{2}\frac{1}{|\boldsymbol{R}_x|^4}\frac{\partial|\boldsymbol{R}_x|}{\partial\boldsymbol{R}}\boldsymbol{l}_x^T[JJ_{00}]\boldsymbol{l}_x + 3\frac{1}{|\boldsymbol{R}_x|^3}\boldsymbol{l}_x^T[JJ_{00}]\frac{\partial\boldsymbol{l}_x}{\partial\boldsymbol{R}} \right] \quad .\end{aligned} \tag{3.39}$$

The former of the two right-hand terms of eq. (3.36) describes the zero-order effects consequent to the drift of the center of mass from the reference trajectory and it is written in a form avoiding the direct subtraction of nearly identical numbers (see [74] for details). The latter term $\boldsymbol{a}_P^x$ is instead the actual spacecraft distributed mass perturbation exerted by P_x. It represents the force due to the gravity gradient over the structure. Lastly, the differential action of the fictitious forces is

$$\begin{aligned}(\delta Q_\Omega)_R &= \left(\frac{\partial T_1}{\partial\boldsymbol{R}} - \frac{\partial T_1^0}{\partial\boldsymbol{R_0}}\right) + \left(\frac{\partial T_2}{\partial\boldsymbol{R}} - \frac{\partial T_2^0}{\partial\boldsymbol{R_0}}\right) \\ &\quad - \left(\frac{d}{dt}\left(\frac{\partial T_2}{\partial\dot{\boldsymbol{R}}}\right) - \frac{d}{dt}\left(\frac{\partial T_2^0}{\partial\dot{\boldsymbol{R}}_{\boldsymbol{0}}}\right)\right) \quad ,\end{aligned} \tag{3.40}$$

with

$$\left(\frac{\partial T_1}{\partial\boldsymbol{R}} - \frac{\partial T_1^0}{\partial\boldsymbol{R_0}}\right) = \Omega^2[A][I_1] + \Omega^2 m\boldsymbol{\delta} \quad , \tag{3.41}$$

$$\left(\frac{\partial T_2}{\partial\boldsymbol{R}} - \frac{\partial T_2^0}{\partial\boldsymbol{R_0}}\right) = m[\tilde{\omega}]^T\dot{\boldsymbol{\delta}} + [\tilde{\omega}]^T[\dot{A}][I_1] \quad , \tag{3.42}$$

$$\frac{d}{dt}\left(\frac{\partial T_2}{\partial\dot{\boldsymbol{R}}}\right) - \frac{d}{dt}\left(\frac{\partial T_2^0}{\partial\dot{\boldsymbol{R}}_{\boldsymbol{0}}}\right) = m[\tilde{\omega}]\dot{\boldsymbol{\delta}} + [\tilde{\omega}][\dot{A}][I_1] \quad . \tag{3.43}$$

So far, has been fully described eq. (3.33), which refers to the orbital motion of the space vehicle. Thus, for sake of completeness, also the attitude equation is extracted from the system (3.25)

$$[m_{\phi\phi}]\ddot{\phi} + [m_{R\phi}]^T\ddot{\boldsymbol{R}} = (\boldsymbol{\delta Q}_\nu)_\phi + (\boldsymbol{\delta Q}_g)_\phi + (\boldsymbol{\delta Q}_\Omega)_\phi \quad , \tag{3.44}$$

where the attitude component of the quadratic velocity vector and the gravity action are respectively

$$(Q_\nu)_\phi = 0 \tag{3.45}$$

and

$$(Q_g)_\phi = -\frac{\partial U_1}{\partial \phi} - \frac{\partial U_2}{\partial \phi} \quad , \tag{3.46}$$

with

$$\frac{\partial U_x}{\partial \phi} = -\mu_x \left[-\frac{1}{|\boldsymbol{R_x}|^2} \left(\frac{\partial \boldsymbol{l_x}}{\partial \phi} \right) [I_1] + \frac{3}{|\boldsymbol{R_x}|^3} \boldsymbol{l_x}^T [JJ_{00}] \frac{\boldsymbol{l_x}}{\partial \phi} \right] \quad . \tag{3.47}$$

The derivative of the gravitational potential with respect to the attitude angle in eq. (3.47) is the well-known torque induced by the gravity gradient. Finally, also the attitude component of the fictitious actions is expressed

$$(Q_\Omega)_\phi = \frac{\partial T_1}{\partial \phi} + \frac{\partial T_2}{\partial \phi} - \frac{d}{dt} \left(\frac{\partial T_2}{\partial \dot{\phi}} \right) \quad , \tag{3.48}$$

where computing the derivatives yields to

$$\frac{\partial T_1}{\partial \phi} = \boldsymbol{v}^T(O')[\tilde{\omega}][A]_{/\phi}[I_1] + \Omega^2 \boldsymbol{R}^T [A]_{/\phi}[I_1] \quad , \tag{3.49}$$

$$\frac{\partial T_2}{\partial \phi} = \dot{\boldsymbol{R}}^T [\tilde{w}][A]_{/\phi}[I_1] + [I_1]^T [\dot{A}]^T_{/\phi} (\boldsymbol{v}(O') + [\tilde{\omega}]\boldsymbol{R}) \quad , \tag{3.50}$$

$$\frac{d}{dt} \left(\frac{\partial T_2}{\partial \dot{\phi}} \right) = [I_1]^T \frac{d}{dt} \left([\dot{A}]_{/\dot{\phi}} \right)^T (\boldsymbol{v}(O') + [\tilde{\omega}]\boldsymbol{R}) + [I_1]^T [\dot{A}]_{/\dot{\phi}} [\tilde{\omega}] \dot{\boldsymbol{R}} \quad , \tag{3.51}$$

with

$$[\dot{A}]_{/\dot{\phi}} = [A]_{/\phi} \quad .$$

The representation of the attitude dynamics can be heavily simplified adopting as body coordinate system (*i.e.* b-frame) the principal axes of inertia. Doing so, the inertia shape integral $[I_1]$ is null and $[JJ_{00}]$ becomes a diagonal matrix; if $[I_1] = 0$, $(Q_\Omega)_\phi$ disappears and $(Q_g)_\phi$ is elementary. Furthermore, this formulation leads to understand that the spacecraft topology, in planar dynamics, can be fully described by a single parameter, known as inertia ratio

$$k_3 = (I_{22} - I_{11})/I_{33} \tag{3.52}$$

where I_{11}, I_{22} are the principal moments of inertia around the axes in the plane of motion and I_{33} is the principal moment of inertia around the out-of-plane axis, which is actually equal to $I_{33} = I_{11} + I_{22}$ for a planar geometry.

Before extensively studying the dynamics of Large Space Structures, it is worth to notice that eq. (3.33) and eq. (3.44) form a set of mutually coupled equations. The main factors accountable for the coupling are

- the mass matrix $[M]$, which is a full-matrix in a general kinematic formulation. Thus, the cross components of the matrix $[m_{R\phi}]$ and $[m_{R\phi}]^T$ shown in eq. (3.33) and (3.44) are evidence of the coupling.
- the gravity action $\boldsymbol{Q}_g$, since the orbital component $(\delta Q_g)_R$ depends on the spacecraft attitude through the term $\boldsymbol{l}_x$, which appears in the expression of the perturbation force (3.39); similarly, the attitude component $(Q_g)_\phi$ is function of the vehicle orbital position relative to the attractor as shown in (3.47).

The two origins of the mutual coupling between orbital and attitude dynamics consist of a significant different nature. The coupling introduced by the mass matrix $[M]$ is only a mere consequence of the kinematic framework employed. In fact, if the rigid motion is described using a local coordinate system (*i.e.* the b-frame) fixed to the body center of mass, the cross components of the matrix $[m_{R\phi}]$ and $[m_{R\phi}]^T$ vanish and with them the coupling too. On this basis, there is no apparent reason to not take advantage of a diagonal mass matrix, which seriously reduces the effort of numerically integrating the motion. Therefore, the origin of the b-frame will be located in the configuration center of mass throughout this work. On the contrary, the interdependence generated by the gravitational action has a physical connotation. It states that both the orbital and the attitude response are coupled by an external action. Such interaction can not be eliminated modifying the kinematic representation.

4 Analysis of the Rigid Fully-Coupled Motion

Contents

One of the main goals of this thesis is about the effect of the spacecraft mass distribution on its fully-coupled dynamics. In the previous Chapter the equations of motion incorporating that perturbation have been derived for a rigid body in vicinity of a reference trajectory. In this Chapter, the dynamic analysis is performed after the numerical implementation and solution of the formulation developed. The results here presented provide a deeper understanding of the motion of the Large Space Structures (LSS) in the PCR3BP and suggest some directions for their mission design. Thus, the Chapter organizes into a brief presentation of some examples to assess the reliability of the code employed and later reports in succession the most interesting results for the orbital and the attitude motion.

4.1 Validation

Throughout the developing of a numerical code several tests and comparisons shall be made to assess the reliability and the accuracy of the solutions

obtained. To satisfy this claim, some evidence to prove the validity of the code employed are reported in this section. Basically, the validation relies on the comparison with other works in literature and another code independently developed for similar purposes. Furthermore, the system has an energy integral of motion that can support the consistence of the simulation when no other comparisons are available.

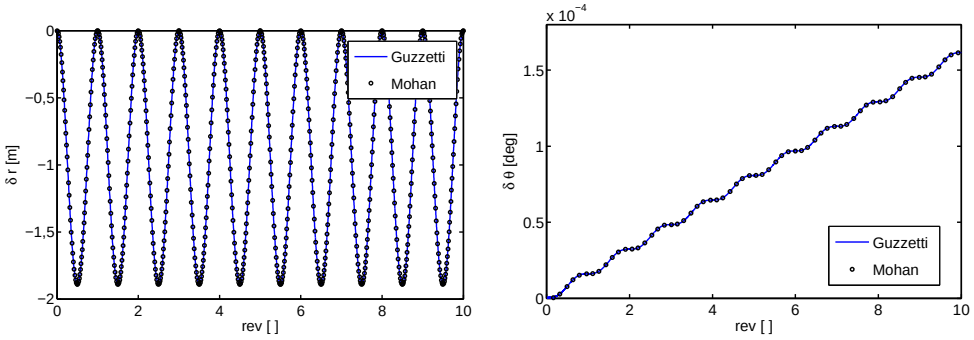

(a) Radial displacement. (b) True anomaly shift.

Figure 4.1: Comparison between the coupled motion predicted by Mohan [11] and by the author.

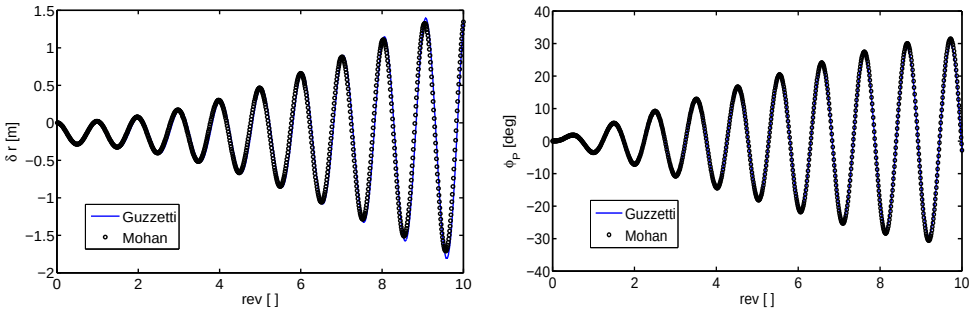

(a) Radial displacement. (b) Attitude angle relative to the radial direction.

Figure 4.2: Comparison between the coupled motion predicted by Mohan [11] and by the author in the near resonant condition.

In 1972, Mohan et al. derived the fully-coupled equations for a rigid

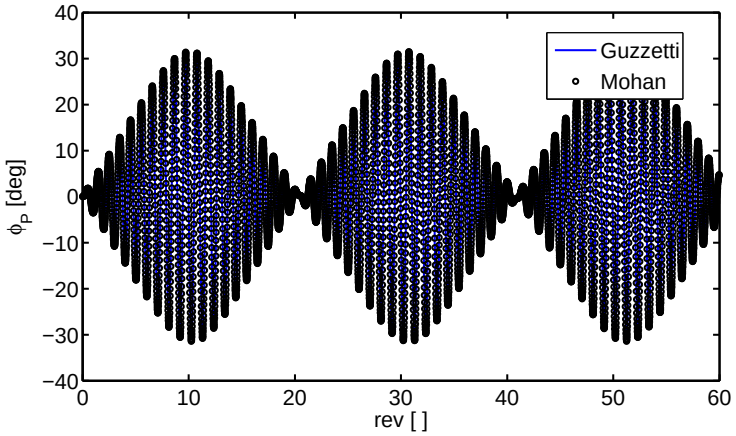

Figure 4.3: Beats phenomena in the near resonant condition.

body in a near keplerian orbit of low eccentricity [11]

$$\ddot{r} - \left(\dot{\theta}^2 - \frac{\mu}{r^3}\right) r = \frac{3G_3^2}{2r^2}\frac{\mu}{r^2}\left[\frac{r_1 + r_2 - 2}{2} - \frac{3k_3}{2}\cos 2\phi_p\right] \tag{4.1}$$

$$2\dot{r}\dot{\theta} + r\ddot{\theta} = \frac{3G_3^2}{2r^2}\frac{\mu}{r^2}\sin 2\phi_p \tag{4.2}$$

$$\ddot{\phi}_p + \ddot{\theta} = -\frac{3\mu}{2r^2}k_3 \sin 2\phi_p \quad , \tag{4.3}$$

where r is the orbital radius, θ denotes the true anomaly and ϕ_p the pitch angle measured from the radial direction; the parameter G_3^2 is the moment of inertia of the body about the pitch axis per unit of mass and $k_3 = (G_{22} - G_{11})/G_{33}$, with G_{ii} representing the moment of inertia about i-th inertia principal axis per unit of mass ($i = 3$ identify the pitch axis). The numerical solution of the system of differential equations (4.1)-(4.3) is compared with the motion predicted by the code implementing the formulation developed in this work. Neglecting the contribution of the secondary, the equations of motions presented in Chapter 3 can reproduce the dynamics near a reference orbit in the R2BP as well. Figure 4.1 reports the perturbed trajectory from a geostationary orbit in terms of the radial displacement and the shift of the true anomaly. In particular, those results refer to a spacecraft configuration defined by $k_3 = 0.7519$, $r_1 = 0.1241$, $r_2 = 0.8759$, $G_3^2 = 1.632 \times 10^7 \mathrm{m}^2$. In Figure 4.1 the trends obtained with the author's model well match the evolution predicted by Mohan in eq. (4.1)-(4.3).

A further evidence is provided studying the resonant condition $k_3 = 1/3$ on a low eccentricity orbit. The reference case is set by the configuration

parameters $k_3 = 0.3323$, $r_1 = 0.3339$, $r_2 = 0.6661$, $G_3^2 = 3.9935 \times 10^6$ m^2 on a orbit with semi-major axis $a = 42164$ km and eccentricity $e = 0.01$. A good agreement between the outcome from the two different sources adopted (*i.e.* author's formulation and Mohan's equations) is still clear for both the orbital and the attitude response, as shown in Figure 4.2. In particular, the attitude oscillations plotted in Figure 4.2-(b) seem to undergo a secular increase of amplitude as expected from the linear analysis in the resonant condition. But, considering a longer time of integration, an interesting phenomenon appears, as depicted in Figure 4.3. In fact, as the pitch oscillations increase the non-linear effects of the coupling limit their amplitude, leading to the beats phenomenon evident in Figure 4.3. The beats are an unambiguous proof of the periodic interchange of energy between the orbital motion and the attitude motion in the resonant or near resonant condition. Further details on this behavior can be sought in [11].

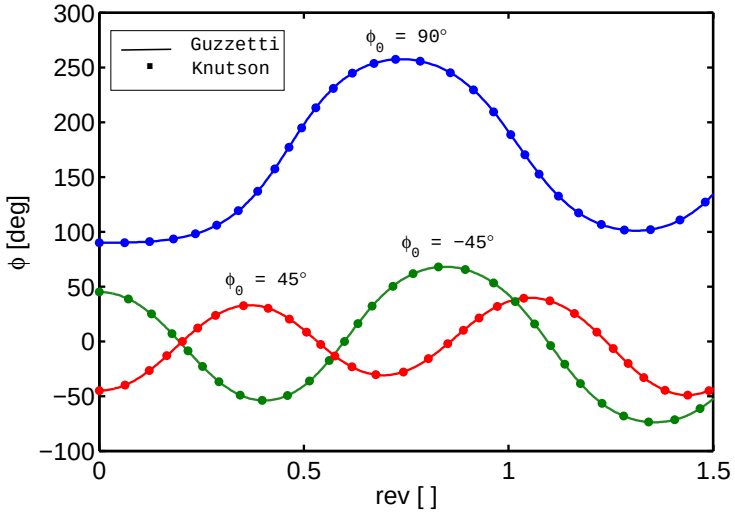

Figure 4.4: Comparison of the attitude angle response (B-orbit, $\phi_0 = \{-45°, 45°, 90°\}$, $\dot{\phi}_0 = 0$) from different algorithms.

In the CR3BP environment the algorithm is validated setting the response against the outcomes from a code with similar purposes. The data reported in this section originated from an internal correspondence with A. Knutson from the Purdue University. Knutson has been developing a code to simulate the spatial attitude dynamics in vicinity of the libration points. She adopts the Kane's method and the algorithm is coded in Fortran. Up to two interconnected body can be introduced in the Knutson's simulator. In order to use the Knutson's work as comparison, the differences with the author's formulation should be highlighted. Firstly, the author of this thesis

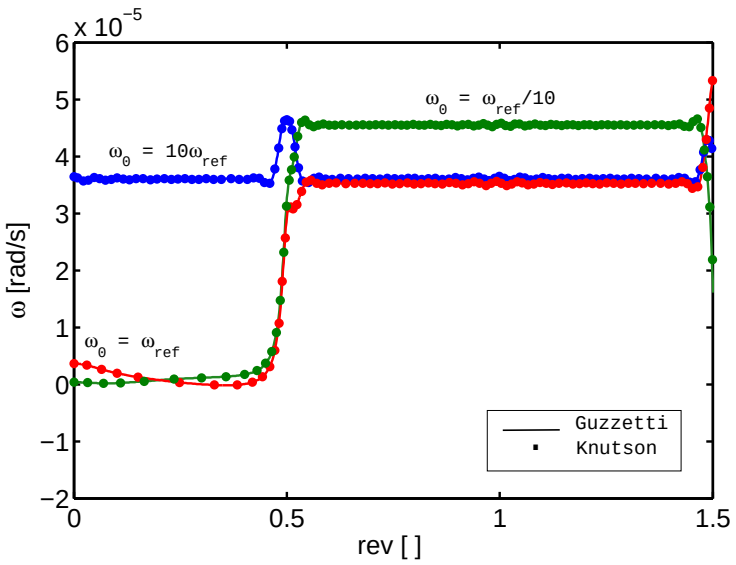

Figure 4.5: Comparison of the angular velocity response (A-orbit, $\phi_0 = 0$, $\dot{\phi}_0 = \dot{\phi}_0 = \{0.1\omega_{ref},\ \omega_{ref},\ 10\omega_{ref}\}$) from different algorithms.

investigates only the dynamics in the orbital plane of the system, while the Knutson's dynamics is three-dimensional. Secondly, the author includes the perturbation force exerted by the mass distribution into the orbital dynamics but Knutson does not. The general parallel between the two algorithms is summarized in Table 4.1.

Table 4.1: Parallel between the algorithms developed by Knutson and Guzzetti.

Knutson	**Guzzetti**
Coded in Fortran	Coded in MATLAB
Kane's formulation	Lagrangian formulation
Spatial Dynamics	Planar Dynamics
No mass distribution perturbation	Include mass distribution perturbation
Two-body architecture	Single body architecture

Given the differences earlier mentioned, only the pitch motion can be reasonably compared. Nonetheless, very few papers are published on the attitude dynamics in the CR3BP, so this analysis is extremely valuable for both the algorithms under development. Moreover, most of the works assume the spacecraft hovering exactly on the libration points or employ a linear approximation of the Lyapunov orbit in the very vicinity of the equi-

libria. On the contrary, in the study with Knutson actual Lyapunov periodic orbits are considered, including the effects of the orbital non-linearities in the attitude response. Thus, several simulations are performed on the basis of common parameters. Throughout the analysis the spacecraft is shaped as a parallelepiped with the following dimensions: 100 m long, 30 m wide, 0.4 m deep. The origin of the b-frame is in the center of mass and the longest side of the parallelepiped is aligned with $\hat{b}_1$. The total mass of the flying vehicle is 140 tons, uniformly distributed. At the initial time the spacecraft lies on the line connecting P_1 and P_2, placed on the left crossing of the Lyapunov trajectory relative to the Lagrangian point. Two planar Lyapunov periodic orbits about L_1 of the Earth-Moon system are selected as the nominal orbital path. They are chosen being significant different in size, in order to compare the attitude motion on both a nearly linear orbit and a truly non-linear orbit. The larger trajectory, labeled as orbit-A, has a period of 19.98 days; the smaller trajectory, labeled as orbit-B, has a period of 11.75 days. Finally, a set of different initial conditions is created by four initial attitude angles $\phi_0 = \{-45°, 0°, 45°, 90°\}$ and three initial angular velocities $\dot{\phi}_0 = \{0,\ 0.1\omega_{ref},\ \omega_{ref},\ 10\omega_{ref}\}$, where $\omega_{ref} = 2\pi/T_{orb}$ and T_{orb} denotes the orbital period. For any simulation in the framework delineated, the pitch libration response from the author's code proves to well fit the Knutson's outcome and vice-versa. For sake of brevity, only few analysis are reported here. Figure 4.4 shows the pitch temporal evolution on the orbit-B for different initial orientations (with $\dot{\phi}_0 = 0$), while Figure 4.5 reports the angular velocity trend on the orbit-A for different initial values of the angular velocity itself (with $\phi_0 = 0$). Again, Figures 4.4 and 4.5 demonstrate the reliability of both the algorithms, in particular considering that they are independently developed and implement different formulations in different code language.

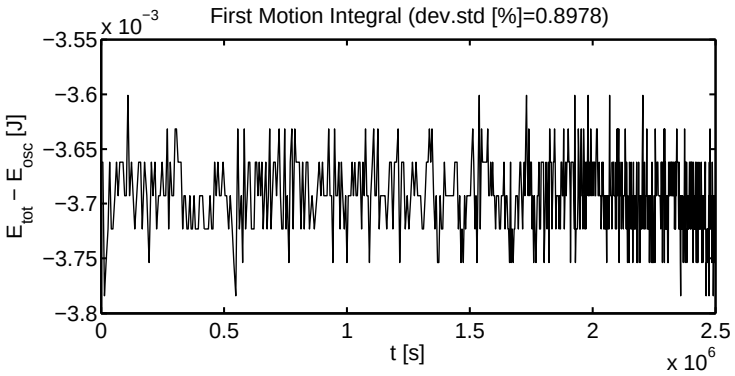

Figure 4.6: Energy Integral Conservation.

Lastly, it is always good practice to identify possible quantities that remain constant during the whole motion. In fact, they represent an inherent mean of the problem to prove the consistence, sometimes even the accuracy, of the analysis without resorting to external data. At least, they are a necessary condition that shall be verified each time the existence of such quantities is known. In a mechanical system a quantity that may stay unchanged is the energy integral of motion. In particular, if the equations of motions are derived via the Lagrangian formulation is quite effortless attesting the energy conservation, even for complex dynamics. As matter of fact, if

$$\frac{\partial \mathcal{L}}{\partial t} = 0 \tag{4.4}$$

then

$$\mathcal{H} = \boldsymbol{p}^T \dot{\boldsymbol{q}} - \mathcal{L} \qquad \text{with} \qquad \boldsymbol{p} = \frac{\partial \mathcal{L}}{\partial \dot{\boldsymbol{q}}} \tag{4.5}$$

is an integral of motion. For the Lagrangian function $\mathcal{L}$ defined in eq. (3.7) it yields to

$$\mathcal{H} = T_{rel} + U_1 + U_2 - T_1 \quad . \tag{4.6}$$

In the former expression of the energy integral of motion (4.6) the energy of the reference orbit is accounted as well. But, as the energy of the reference orbit is the major contribution to the total amount, the evaluation of (4.6) turns out to be misleading. The perturbing action incorporated derives from the higher terms of the gravitational potential expansion, so it still retains a conservative nature and the total energy shall be constant during the motion. Nonetheless, even if the implementation of perturbation is not consistent with the energy conservation it may be not noticed observing the total energy of the system, which is in large part due to the reference orbit and only in a minimal amount to the terms of higher order. Therefore, if the former contribution is constant, inconsistence in the latter becomes unnoticeable. A practicable solution consists in subtracting the energy of the osculating orbit E_{osc}, which is constant, to the total value E_{tot}, which is constant too. The difference shall be constant throughout the evolution of the system as well, as shown in Figure 4.6. Its standard deviation from the mean value can be an index of the integration accuracy.

4.2 Orbital Dynamics

The topic of the research detailed in this section is the dynamic analysis of rigid mass-distributed architectures under a multi-body gravitational field

from the orbital motion perspective. The scope of the investigation concerns the drift from a Lyapunov periodic orbit in the PCR3BP after the introduction of a more accurate description of the gravity action on Large Space Structures, as described in Chapter 3. To this end, a sensitivity campaign is performed varying the gravitational environment, the body shape and dimension and the initial conditions.

The drift from the nominal path is particularly interesting because of the direct correlation with the orbit stability. In fact, the zero-order dynamics of the CR3BP is well-known to be chaotic, implying that small perturbations of the reference conditions lead to significant alteration of the motion. Thus, under a natural dynamics, even small errors in position (*e.g.* in the order of meters) will easily provoke the divergence of the trajectory from the periodic orbit within a limited time window, comparable to few periods. In the following results the shift from the osculating orbit is represented as the radial displacement

$$\delta r(t) = |\boldsymbol{R}(t)| - |\boldsymbol{R_0}(t)| \quad , \tag{4.7}$$

where $\boldsymbol{R}(t)$ is the actual position vector of the spacecraft and $|\boldsymbol{R_0}(t)|$ denotes the position vector on the osculating orbit at the same temporal instant. Specifically, the final radial displacement $\delta r_f = \delta r(t_f)$ after 2.5 revolutions around the Lagrangian point will be monitored.

To begin with, the responses are compared for different Lyapunov periodic orbits from families around L_1 and L_2. The Earth-Moon and the Sun-Earth are the planetary systems addressed. The complete set of osculating orbits is summarized in Table 4.2 for the Earth-Moon system, in Table 4.3 for the Sun-Earth system. The size variation of these trajectories is designed to cover the transition from the nearly linear to the truly non-linear orbital dynamics in vicinity of the libration points. Hence, in this gravitational environment study the spacecraft is assumed to be a parallelepiped 100 m long, 30 m wide, 0.4 m deep, with a total mass of 140 tons uniformly distributed. The origin of the b-frame is in the center of mass and the longest side of the parallelepiped is aligned with $\hat{b}_1$. For each simulation, the spacecraft is initially located on the left crossing of the Lyapunov periodic orbit relative to L_1 or L_2 equivalently. At the starting point, the body attitude angle ϕ_0 may be varied while the angular velocity $\omega_0 = \dot{\phi}(t = 0)$ observed in the ℓ-frame is always null.

The results of this first analysis can be stated in the following considerations:

Table 4.2: Vertical Amplitude A_y and Period T_{osc} for the set of osculating Lyapunov orbits in the Earth-Moon system.

L_1		L_2	
A_y [km]	T_{osc} [days]	A_y [km]	T_{osc} [days]
145761	22.17	146446	23.12
123640	19.97	124948	20.83
87593	16.13	92279	17.41
64011	13.95	69637	15.82
42351	12.61	43959	15.00
32208	12.21	28348	14.79
13213	11.78	15386	14.69
6593	11.72	6125	14.67

Table 4.3: Vertical Amplitude A_y and Period T_{osc} for the set of osculating Lyapunov orbit in the Sun-Earth system.

L_1		L_2	
A_y [km]	T_{osc} [days]	A_y [km]	T_{osc} [days]
4030245	321.53	4031849	322.56
3250533	282.19	1410349	282.93
1716542	200.76	1725303	202.26
1081877	183.45	1084845	185.45
810258	179.47	806328	181.63
711690	178.4	691964	180.49

1. Despite the slightness of the perturbation added, the consequences on the orbital motion over few periods are appreciable and large enough to eventually destroy the nominal trajectory.

2. The attitude and the orbital motion prove to be sensibly coupled, as different initial spacecraft orientations lead to different final orbital positions.

3. The phenomenon is visible for reasonable body dimensions (structure size comparable to the International Space Station).

4. The final radial displacement δr_f is not a monotonic function of the orbit size. Thus, the minimum does not correspond neither to the largest nor smallest orbit.

5. The final shift from periodic orbits around L_2 is larger than around

L_1.

6. The perturbation is weaker in the Sun-Earth system than in the Earth-Moon system.

Figures 4.7 and 4.8 are reported as evidence of the aforementioned points. Examining the Earth-Moon environment, Figures 4.7 presents the final radial displacement δr_f as function of the orbit size, which is easily deducible from the period of the osculating trajectory in abscissa. The trend in vicinity of the both L_1 and L_2 is plotted. Different curves refer also to different initial attitude angles. In Figures 4.7 can be noticed that the worst case in the set (*i.e.* the maximum δr_f) corresponds to a spacecraft in the smallest Lyapunov orbit about L_1 and initial $\phi_0 = 0°$. Likewise, Figure 4.8 depicts the δr_f fashion in the Sun-Earth system, although only the curve for $\phi_0 = 0°$ is shown. It is worth to remark that the conclusions drawn earlier and later hold true within the scenario analyzed and shall not be regarded as universal arguments. Further efforts and demonstrations are required to achieve a boarder range of validity due to the complexity of the dynamics addressed.

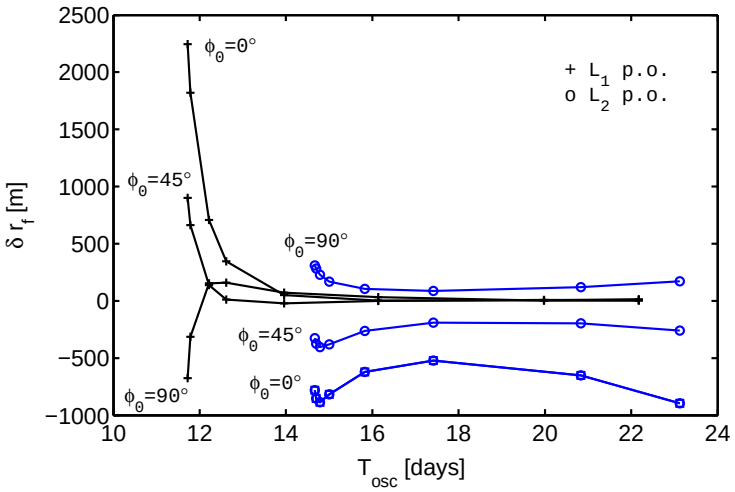

Figure 4.7: Final radial displacement δr_f after 2.5 revolutions as function of the osculating orbit period T_{osc} and the initial attitude angle ϕ_0 in the Earth-Moon system.

A second campaign of simulations is carried out to investigate the influence of the body shape on the perturbed orbital motion. Assuming a planar dynamics and a gravitational potential expansion up to the second order, the spacecraft mass distribution topology can be parametrized by a

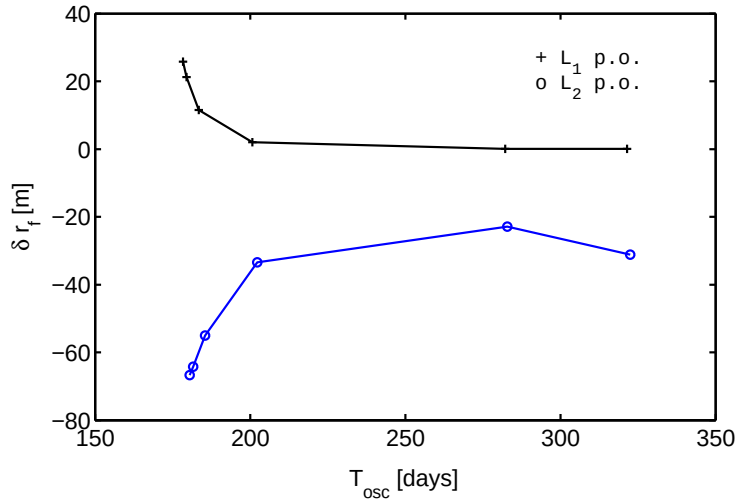

Figure 4.8: Final radial displacement δr_f after 2.5 revolutions as function of the osculating orbit period T_{osc} with $\phi_0 = 0°$ in the Sun-Earth system.

single quantities $k_3 = (I_{22} - I_{11})/I_{33}$, where I_{33} is the principal moment of inertia around the axis normal to the orbital plane and I_{11}, I_{22} are the principal moments of inertia around the axes in the plane of motion. $k_3 = 0$ represents an axisymmetric body, while $k_3 = \pm 1$ means that the body collapses along one of the principal inertia directions in the plane. The body is still assumed to be a parallelepiped and the shape is varied maintaining constant the length $L = 100$ m of the side aligned with the versor $\hat{b}_1$ of the local coordinate system. As the b-frame is also placed in the center of mass of the configuration, the three body axis $(\hat{b}_1, \hat{b}_2, \hat{b}_3)$ are the principal directions. So, $k_3 = 0$ means that both sides are equal to 100 m; conversely, if $k_3 = 1$, one side is null and the structure collapses in a 100 meters-long beam lying on $\hat{b}_1$. The sensitivity campaign is based on mass distributions in the whole range $k_3 = [0, 1]$. Next, the analysis is conducted in the Earth-Moon system, using the set of orbits in Table 4.2. Lastly, the spacecraft is initially on the P_1-P_2 line, to the left of the equilibrium point, with $\hat{b}_1$ aligned to $\hat{\ell}_1$. Figure 4.9 offers a comprehensive picture of the dynamics in this scenario. For different values of k_3, it shows the trend of δr_f as function of the orbital size. In this study the largest perturbation on the orbit is observed for $k_3 = 1$, while the weakest is observed for $k_3 = 0$. In the latter case, the effects are minimal but do not disappear as happens for the gravity torque. Both the gravity gradient force introduced in this work and the well-known gravity gradient torque arise from the second-order term in the gravitational potential Taylor series. But, unlike the gravity gradient torque, the gravity gradient force can not be nullified by designing an

axisymmetric spacecraft, as demonstrated in Figure 4.9. In that case, the only -still significant- achievement is the minimization of the perturbation. Fixed the osculating orbit (*i.e* around L_1 with period 22.17 days), a deeper understanding on the response is provided by Figure 4.10. It is evident from Figure 4.10 that, as k_3 increases, not only the final displacement δr_f, but the entire response is amplified. Furthermore, the orbital response appearing in the Figure is not radically altered by fundamental changes in the spacecraft topology (k_3 varies from 0 to 1). On the contrary, as discussed in the next section, the attitude behavior is strongly affected by the ratio between the principal inertia moments or, in other words, by the body shape. Thus, the rotational motion of the vehicle may considerably differ between the cases creating Figure 4.9.

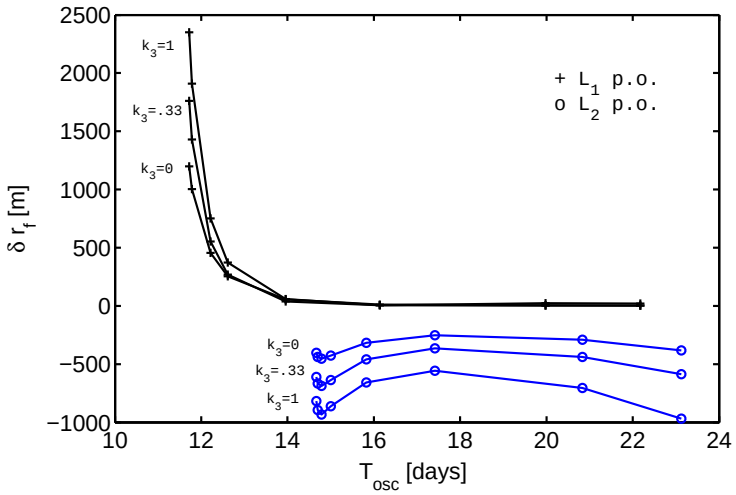

Figure 4.9: Final radial displacement δr_f after 2.5 revolutions as function of the osculating orbit period T_{osc} and the spacecraft topology in the Earth-Moon system.

So far, the initial angular velocity $\omega_0 = \dot{\phi}(t = 0)$ has been kept equal to zero. To avoid misinterpretations, it should be recalled that the attitude is defined as the angle ϕ between the b-frame and the ℓ-frame. In this work, the angular velocity attributed to the body refers to the temporal derivative of ϕ. Therefore, when the angular velocity $\omega = \dot{\phi}$ is null, it does not imply that the spacecraft is not rotating. In fact, it shall be noted that the ℓ-frame is not an inertial coordinate system, but rotates with rate Ω. It follows that the spacecraft rotates with the same rate Ω when observed from an inertial coordinate system, as the I-frame. The effects of imposing a non-zero initial angular velocity ω_0 are depicted in Figure 4.11. Figure 4.11 deserves

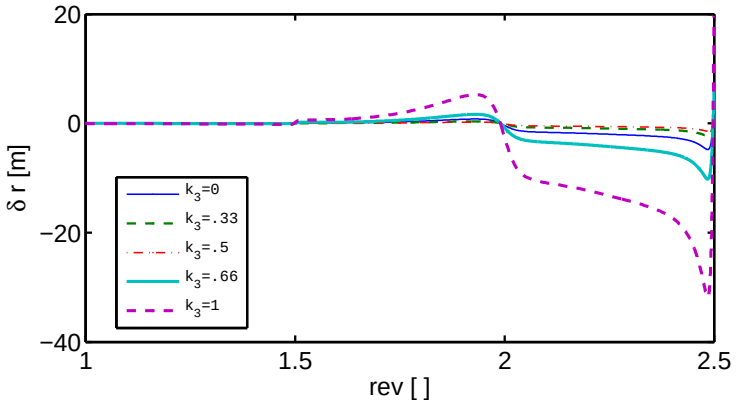

Figure 4.10: Radial displacement evolution δr_f as function of the spacecraft topology in the Earth-Moon system.

further explanations. Firstly, ω_0 is expressed as multiple of ω_{osc}, which is defined as the mean angular rate of the spacecraft on the orbit $\omega_{osc} = 2\pi/T_{osc}$. Secondly, large periodic orbit refers to the largest orbit of a specific family in Table 4.2; likewise, small periodic orbit refers to the smallest orbit of a specific family in Table 4.2. Only trajectories in the Earth-Moon system are considered. It appears quite clearly in Figure 4.11 that the increase of ω_0 leads eventually to a reduction of the perturbation. It also seems that, after a certain threshold, a further growth of the initial angular velocity does not lead to any noticeable decrease of the final radial displacement. As the ratio between the body angular velocity ω_0 and the orbital angular rate ω_{osc} rises up to several orders of magnitude, the attitude dynamics becomes much faster than the orbital motion. Here, it can be inferred that high frequencies of rotation emulate an axisymmetric distribution of mass. Roughly, the mass occupies uniformly each achievable place around the spinning axis before that the body changes its position. This explains the diminution of δr_f (it has been previously demonstrated that $k_3 \to 0$ lessen the perturbation) and the plateau visible in Figure 4.11. In fact, once the spacecraft rate of rotation is large enough to practicably reproduce an axisymmetric distribution of mass, it is straightforward to see that the situation can not improve anymore in this direction. The behavior as function of ω_0/ω_{osc} could be also interpreted in reason of the coupling between the orbital and attitude dynamics. A large ratio between the frequency of the motions implies that their dynamics is decoupled. The greater is the frequency gap, the less the two motions mutually interfere. From this perspective, $k_3 = 0$ could be considered a special case of decoupling: as the attitude is constant (the gravity gradient torque is the only external moment on the system and is null when $k_3 = 0$), there is no chance to transfer energy between the

orbital and attitude motions.

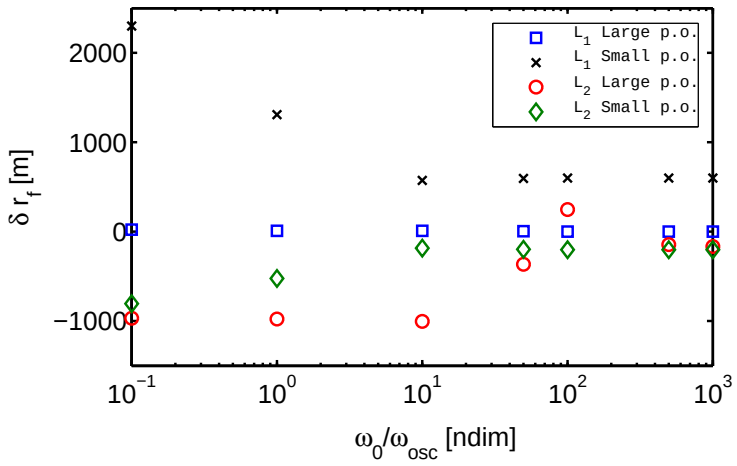

Figure 4.11: Final radial displacement δr_f after 2.5 revolutions as function of the initial angular velocity ω_0 in the Earth-Moon system.

The last study advanced in this section aims at understanding the role of the spacecraft characteristic dimension. As the novel dynamics addressed relays on modeling the mass distribution itself, it is important to correlate the response of the system to the extension of such distribution. It is obvious to notice that Large Space Structures distinguish them-selves because of the size of the flying vehicle. To that end, the spacecraft is modeled as a beam of length L along the $\hat{b}_1$ axis, with the b-frame fixed to the center of mass, while the starting orbital and attitude conditions are the same as the previous analysis, besides the specification of a null angular velocity ω_0. Before discussing the outcomes from the entire campaign of simulations, it is worth to analyze a sample case. In Figure 4.12 there are the typical trends of the radial displacement over the orbit for different spacecraft lengths. The dynamics in the example takes place on a large Lyapunov orbit ($T_{osc} = 22.17$ days) about L_1 in the Earth-Moon system. Figure 4.12 plots curves describing the departure from the nominal path that seem to be identical, or more correctly show the same fashion projected on different scales. This evidence of cross-similarity (or quasi cross-similarity, as further studies are required to prove the patterns to be exactly identical) has a relevant impact on the understanding of the mechanisms that underlie the phenomenon. It means that the body size does not alter the nature of the orbital dynamics response, but only amplifies the effects. It follows that, small satellites as well as Large Space Structures undergo the same orbital motion, just on different scales. Likewise, a closer inspection of a single

time history reveals that, not only the responses from different values of L are similar, but also the single trend for a given length repeats itself on different scales as the time increases. The propriety of auto-similarity (or quasi auto-similarity) is clearly visible in Figure 4.13, where the dynamics is integrated for a longer period, considering a 100 meters-long beam orbiting a large Lyapunov of L_1 in the Earth-Moon system. The most direct consequence of auto-similarity is that, no matter how small are the drifting effects on the first orbit, they will reappear identical but increased on each following revolutions and the trajectory will eventually diverge from the Lyapunov orbit. In other words, even normal sized satellite orbiting in vicinity of the librations points will depart from their locations after few periods. Figure 4.13 shows that a spacecraft with a characteristic length of 100 m will be displaced by 40 km in 4 revolutions, so in the next one or two orbits will be likely far away from the nominal path.

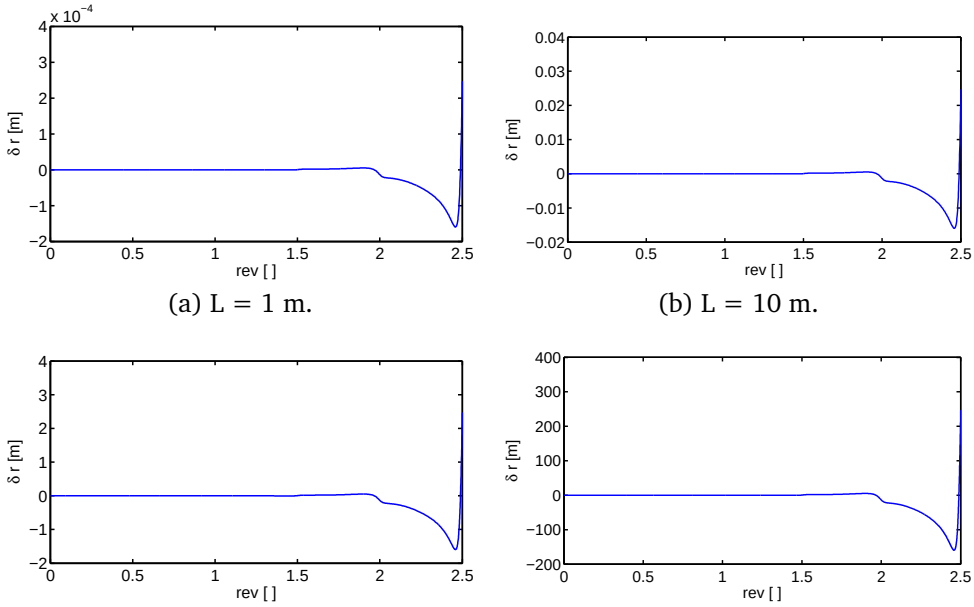

(a) L = 1 m. (b) L = 10 m.

(c) L = 100 m. (d) L = 1000 m.

Figure 4.12: Cross-similarity of different responses for variations of the spacecraft characteristic length.

In addition to the examples recalled, an overview of the of entire investigation is depicted in Figure 4.14. Figure 4.14 plots the final radial displacement δr_f over 4 periods as function of the spacecraft length

$$L\,[\mathrm{m}] = \{1,\ 2,\ 5,\ 10,\ 20,\ 50,\ 100,\ 200,\ 500\,1000,\ 2000,\ 5000\} \quad .$$

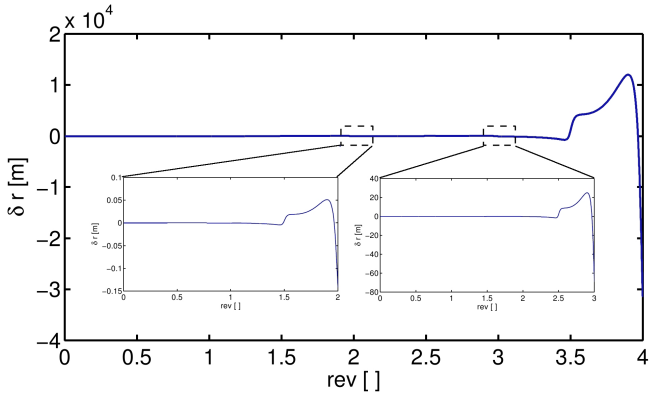

Figure 4.13: Auto-similarity of the response.

The trend is studied for large, medium, small periodic orbits, which have respectively period: 22.17 days, 16.13 days, 11.72 days, around L_1 and 23.12 days, 15.82 days, 14.67 days, in vicinity of L_2. In Figure 4.14 appears distinctly that a relationship between the final radial displacement and the spacecraft size exists. As shown by the data fitting in the plot (please notice the axes logarithmic scale), the relationship seems to be parabolic and can be written in the form

$$\delta r_f = \mathcal{A} L^2 \quad , \tag{4.8}$$

where $\mathcal{A}$ is a scaling factor which is function of the osculating orbit and the period of integration. Beside the quantitative and accurate prediction of the final displacement through the fit (4.8), it is important to notice the order of the relationship between the shift from the osculating orbit and the spacecraft characteristic dimension. A second-order means that as the spacecraft size is doubled the perturbation is quadrupled. Finally, an attentive observer of Figure 4.14 might notice that the fit proposed in eq. (4.8) is valid up to a certain value of δr_f (in the order of 10^8m). Likely, when the trajectory departs sufficiently from the osculating orbit, the trajectory is not governed any more by the perturbation, but instead the dynamics of the center of mass alone regains possession of the motion. In that event, the fit proposed naturally ends its validity.

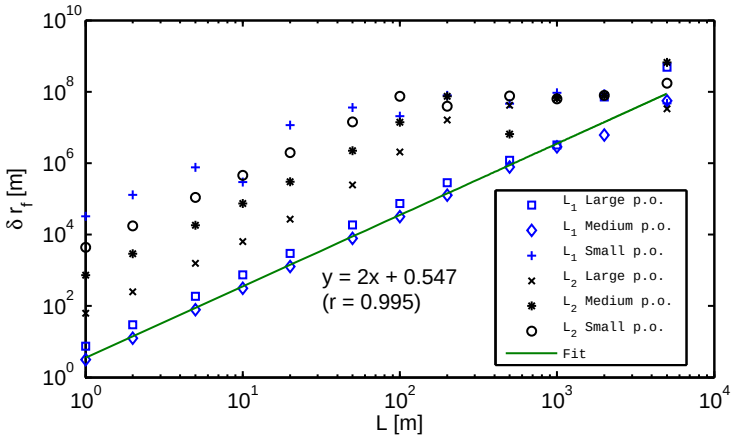

Figure 4.14: Final radial displacement δr_f as function of the spacecraft characteristic length.

4.3 Attitude Dynamics

The topic of the research detailed in this section is the dynamic analysis of rigid mass-distributed architectures under a multi-body gravitational field from the attitude motion perspective. The scope of the investigation concerns the identification of bounded (its not proper to use the word stable) angular motions and to outline the conditions that guarantee such responses on a Lyapunov periodic orbit in the PCR3BP, after the introduction of the gravity torque, as described in Chapter 3. To this end, a sensitivity campaign is performed varying the gravitational environment, the body shape.

The most of the studies on the natural attitude dynamics in the CR3BP assume the spacecraft fixed in the Lagrangian point [50, 51, 52, 53, 54, 55]. So the influence of the orbital motion on the attitude response is basically neglected. Wong et al. [56] introduce in their work the translational motion of the spacecraft by considering a linear approximation of the Lyapunov periodic orbits. They discover a resonant condition of the spacecraft librations in the synodic plane due to the coupling between the attitude and orbital motion. This condition is expressed in terms of a critical value for the inertia ratio $k_3 = k_{crit}$, which leads the rotational dynamics to have the same frequency as the linear Liapunov orbit approximation. In L_2 of the Sun-Earth system $k_{crit} \approx 0.3579$, while in L_2 of the Earth-Moon system $k_{crit} \approx 0.364$. Considering Lyapunov orbits in the linear form, that represents the only case where the vehicle natural oscillations grow indefinitely. However, since the Lyapunov orbits are linearly approximated, these results

are only valid for relatively small orbits close to the equilibrium points. Knutson et al. [57] in her recent paper studies the rotational dynamics on non-linear numerically-computed Lyapunov and Halo periodic orbits. She shows that the nonlinear regime of the orbital motion can seriously affect the stability of the attitude motions. Thus, the current investigation continues along this direction to improve the understanding of the rotational behavior of a spacecraft in a fully coupled nonlinear regime.

What is still pending in the Knutson work [57] is the evidence, and in the event the definition, of thresholds between bounded and unbounded pitch responses as function of the orbit size and spacecraft topology, which are the two governing parameters of the phenomenon. Here, it is worth to spend some words on a little digression. It the investigation presented in this section the words stable or instable will never be used as attributes of the pitch response observed. That would not be correct. By definition, the stability refers to the solutions of a system as the capacity of those solutions to remain indefinitely close to them-selves against small perturbations. Therefore, the solution shall not be confused with its propriety. A response limited over time does not tell us anything about its stability, since further analysis are required to prove the solution to not explode under small perturbations (at least the solution should be perturbed!). So the pitch response we observe is just the solution of the natural dynamics of the system, but we do not know its sensitivity to perturbations. Misinterpretations may arise because the most of us are used to study trajectories nearby the equilibrium points of a general system and the boundedness of those trajectories is the proof of the stability of the system; nonetheless, it should be realized that the equilibrium point represents the actual solution of the system and we are observing the perturbed motion nearby that solution. In conclusion, the analysis in this section aims only at the boundedness or unboundedness of the pitch solutions, not to their stability or instability.

Two main factors affect the natural attitude dynamic of the space structure: the orbital path and the distribution of mass. Therefore, to seek bounded solutions these are the first parameters to be explored. Three characteristic samples of Lyaponouv orbits are selected in the analysis: a fully nonlinear orbit labeled as large; a nearly linear orbit labeled as small; an orbit in the middle of the formers labeled as medium. Nonetheless the small orbit might be approximated with the linear solution, all the orbits are numerically computed following the procedure in Chapter 2, accounting for the nonlinear behavior, regardless whether it is dominant or not. The simulations campaign takes place in the Earth-Moon system, even if

can be easily moved to other systems, such as the Sun-Earth environment. The periods of the sample orbits are detailed in Table 4.4 for both the families around L_1 and L_2. Secondly, the dependence of the gravity gradient torque on the body distribution of mass is function only of the inertia ratios. Specifically, this is truly correct when the gravity moment is derived from a second-order expansion of the potential: an higher order series will account further details of the spacecraft topology and more parameters may be needed. However, since that is not the current case and additionally the motion is planar, the inertia ratio k_3 alone is sufficient to characterize the spacecraft shape.

Table 4.4: Sample orbits period for the attitude dynamics campaign.

Orbit Size	T_{osc} **[days]**	
	L_1 Family	L_2 Family
Large	22.17	23.12
Medium	12.61	15.82
Small	11.72	14.67

In this analysis the pitch motions is considered bounded when the spacecraft does not overturn it-self. Technically, the solution is bounded when $\phi \in [-90°, 90°] \ \forall t < \bar{t}$. An adequate window of observation is set by $\bar{t} = 2.5T_{osc}$, where T_{osc} is the period of the Lyapunov orbit. The spacecraft may actually undergo larger rotation on a longer period, that would change the classification of the motion, but the selected temporal span can be judged an adequate sample of the attitude time history, as unlikely the spacecraft will remain totally uncontrolled for a such long period. Then, the results of the simulation survey can be effectively summarize in a table by combining the test parameters and marking the solutions which appear to be limited. Doing so, Table 4.5 is created for the family of orbit about L_1 and Table 4.6 for the family of orbit about L_2. The responses related to each row of the aforementioned Tables are plotted in the Figures referred in the last column of the Tables them-selves.

The examination of outcome for the L_1 family in Table 4.5 leads to the following conclusions:

1. As noticed by Knutson [57], nonlinearities of the orbital motion affect the pitch response to the extend that the spacecraft generally starts to spin indefinitely, in particularly after a close approach of the secondary at $t = 0.5T_{osc}$. However, a complete exploration of the possible

Table 4.5: Analysis map of the bounded pitch responses in vicinity of L_1.

Orbit Size	k_3 0.05	0.20	k_{crit}	0.80	0.95	**Ref. Figure**
Large	x	x				4.15-(a)
Medium	x	x				4.15-(b)
Small	x	x		x	x	4.15-(c)

x: *the symbol denotes a pitch response within* $\pm 90^\circ$ *limit.*

Table 4.6: Analysis map of the bounded pitch responses in vicinity of L_2.

Orbit Size	k_3 0.05	0.20	k_{crit}	0.80	0.95	**Ref. Figure**
Large						4.16-(a)
Medium	x					4.16-(b)
Small	x	x		x	x	4.16-(c)

x: *the symbol denotes a pitch response within* $\pm 90^\circ$ *limit.*

mass configurations demonstrates, as shown in Figure 4.15-(a), that for $k_3 \to 0$ (*i.e.* the body approach an axisymmetric topology) the motion can return to be confined.

2. A sharp-edge variation of the pitch angle is evident in Figure 4.15-(a) as soon as the spacecraft approaches the secondary at $t = 0.5T_{osc}$ or $t = 1.5T_{osc}$. This rapid change in the ϕ derivative is lessen for $k_3 \to 0$, but do not disappear even for very small values of k_3. Instead, it does not occur when the orbit size is reduced, as noticeable in 4.15-(b), which refers to a medium size orbit.

3. The results proposed by Wong [56] are still valid on numerically computed Lyaponuv periodic orbits, if they are close enough to the linear approximation. As shown in Figure 4.15-(c), the response for $k_3 = k_{crit}$ actually respect the limits for the ϕ angle, but it will not be marked as bounded since the oscillations are known from [56] to increase endlessly.

Likewise, the study for he L_2 family in Table 4.6 adds considerations as follows:

1. Unlike the sample from the L_1 family, the selected large orbit about L_2 seems to not allow bounded motions even for k_3 close to zero.

2. The chance to obtained limited solution for $k_3 \rightarrow 0$ is retreived by decreasing the orbit size, as reported in Figure 4.16-(b).

All considered, there is a clear indication that a threshold between the bounded and unbounded pitch responses exists and it is function of the orbit size and spacecraft topology. Specifically, as the orbit dimension increases and nonlinear effects of the orbital dynamic are accounted, the spacecraft shall approach an axisymmetric mass distribution (*i.e.* $k_3 \rightarrow 0$) in order to guarantee limited attitude librations over a certain time window. Large Lyapunov orbits are the first extreme of this behavior, since they lead to the unbounded response even for values of k_3 close to zero, as observed in the L_2 family. The second is represented by small Lyapunov orbits, which always guarantee limited natural oscillations, with the exception of the resonant condition $k_3 = k_{crit}$.

The understanding gained with the previous analysis makes a significant contribution to the design of Large Space Structures or even classical satellites. It allows to predict if the natural pitch librations of the vehicle will be bounded and suggests how to alter either the orbit size or the mass distribution in order to contain the motion into the desired limits. A natural bounded solution is desired when it is related to control requirements. In fact, it is likely that the control effort will be smaller and also controlling devices with saturation issues, such as reaction wheels, will be more effective. So, for instance, considering the large Lyaponuv orbit of the family around L_1, the threshold between a limited or diverging solution might be sought. It results that configurations with $k_3 < 0.32$ undergo a bounded pitch libration, while structures with $k_3 > 0.33$ start to spin perpetually in one direction. Otherwise, instead of varying the inertia ratio, the orbit size could be changed keeping fixed the spacecraft topology. For example, assuming $k_3 = 0.8$ the orbit size can be reduced until a bounded pitch motion appears. This happens between an orbit of period $T_{osc} = 12.21$ days and other with $T_{osc} = 11.78$ days. Figure 4.17 compares the bounded and unbounded solutions of this example and for the case $k_3 = 0.95$.

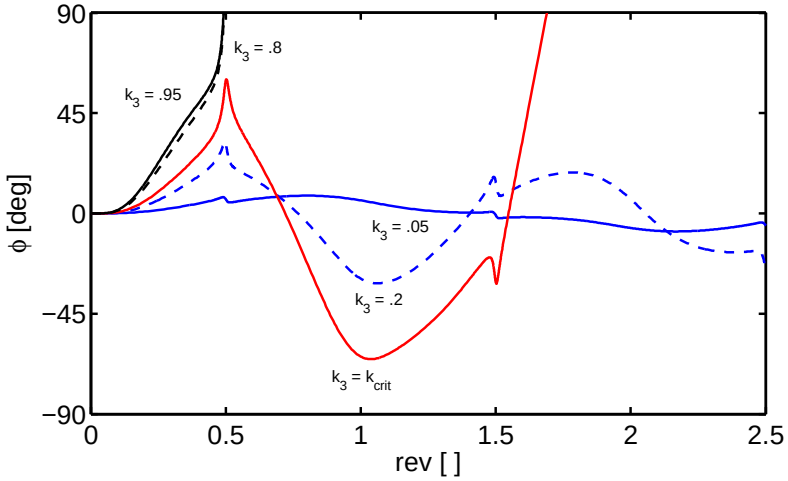

(a) Large Lyapunov.

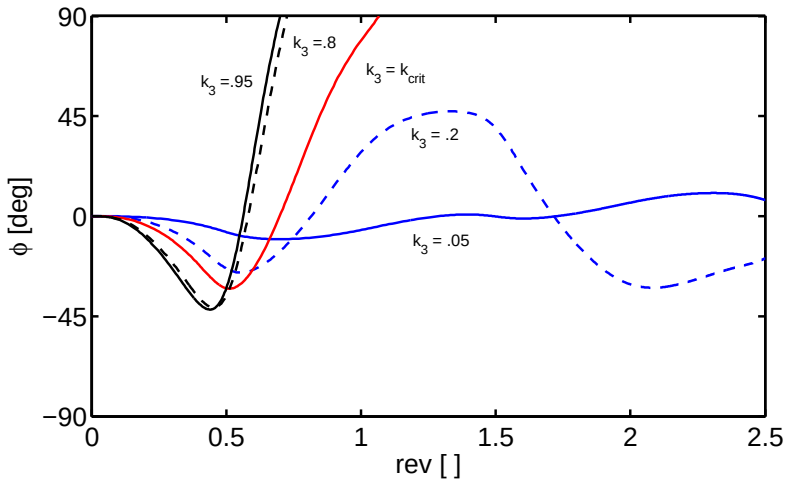

(b) Medium Lyapunov.

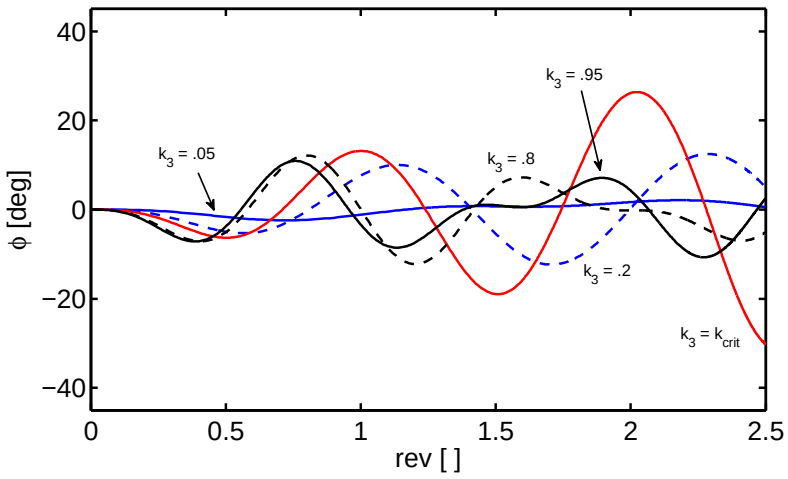

(c) Small Lyapunov.

Figure 4.15: Pitch response on periodic orbits about L_1.

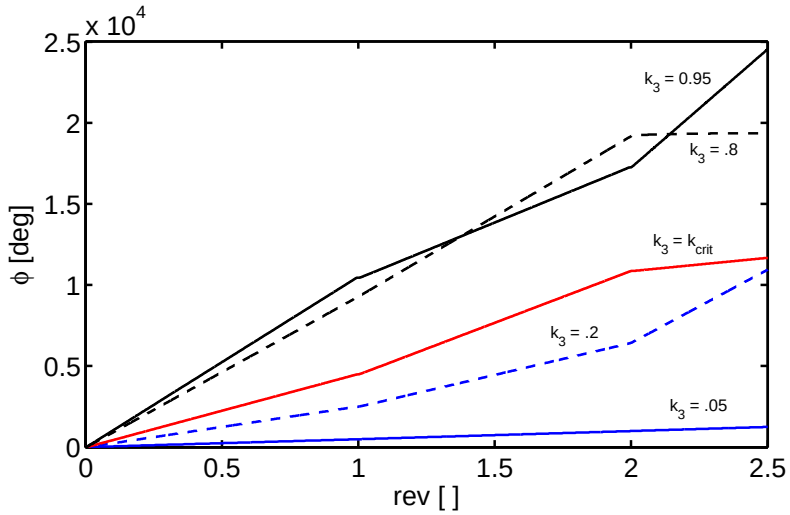

(a) Large Lyapunov.

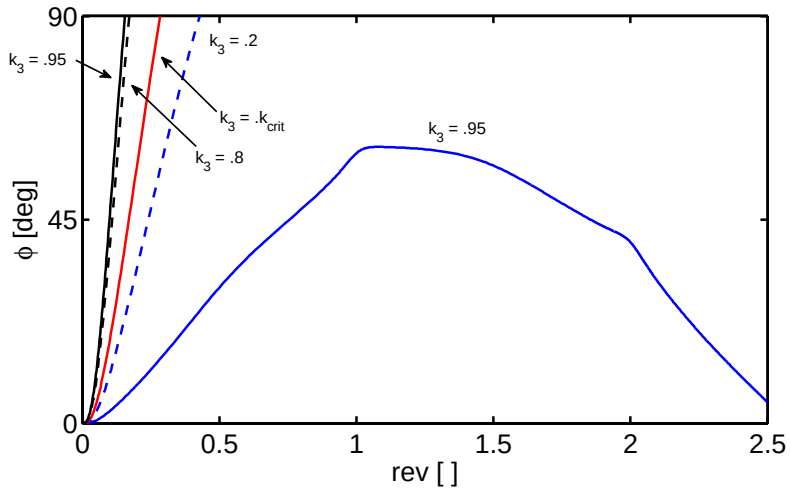

(b) Medium Lyapunov.

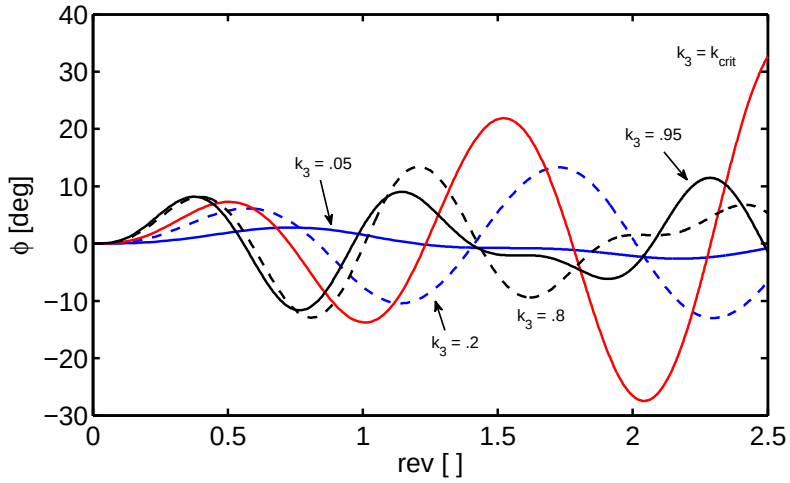

(c) Small Lyapunov.

Figure 4.16: Pitch response on periodic orbits about L_2.

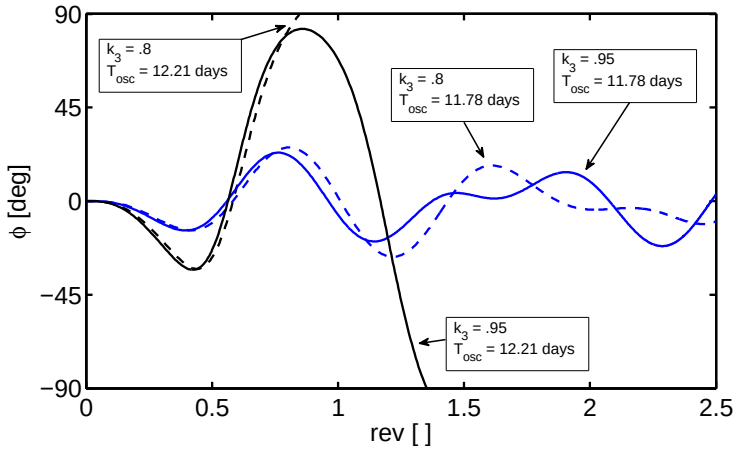

Figure 4.17: Example of the orbit size threshold between bounded and unbounded pitch response.

4.4 Comparison with other perturbations

One of the initial ideas of this work was to exploit the effects of a fully-coupled dynamical model as an effective tool to actively maneuver the spacecraft. In particular, the main interest was to maintain the reference orbit against other perturbations by controlling the attitude dynamics. To this end, it is preliminarily necessary to establish that the mass distribution induced force:

1. can be arbitrarily directed, regardless the position on the orbit;

2. is enough strong to reject common external perturbations.

For a beam-like ($k_3 \to 1$) spacecraft, it can be demonstrated that, on large Lyapunov orbits of the L_1 family, the body attitude controls the force orientation allowing to target any desired direction in any position on the trajectory. Nevertheless, the order of magnitude of such force results to be negligible when compared with other perturbations, that certainly affect the system. First of all, the solar radiation pressure is the dominant disturbance of the orbital dynamics in vicinity of the libration points. In fact, it is straightforward to see that no atmospheric drag survives at such distance from the attractors, and for the same reason, the influence of the attractor oblateness decades very rapidly. To have a rough approximation of the acceleration provoked by the the solar radiation pressure a_{SRP} in the Earth-Moon system, it could be recalled a formula from Wertz [75]:

$$a_{SRP} = -4.5 \times 10^{-6}(1+c)A/m \quad , \tag{4.9}$$

where A is the satellite cross-sectional area exposed to the sun in m^2, m is the satellite mass in kg, c is a reflection factor ($c = 0$ for absorption, $c = 1$ for specular reflection, $c \approx 0.4$ for diffuse reflection). The solar pressure acceleration estimated with eq. (4.10) is compared with both the mean and maximum value of the acceleration a_{dm} induced by the mass distribution (with $k_3 = 1$), as function of the spacecraft characteristic length L. a_{dm} is computed, fixing $\phi = 0$, along a large periodic orbit about L_1 in Figure 4.18 and along a small one about L_1 in Figure 4.19. In neither the former nor the latter case, a_{dm} results to be in the least comparable to a_{SRP}, derived by eq. (4.10) assuming reasonable values of the ratio A/m (the International Space Station has $A/m \approx 0.01$ m^2/kg). Therefore, there are no credible chances to control the weaker perturbation to reject the stronger disturbance.

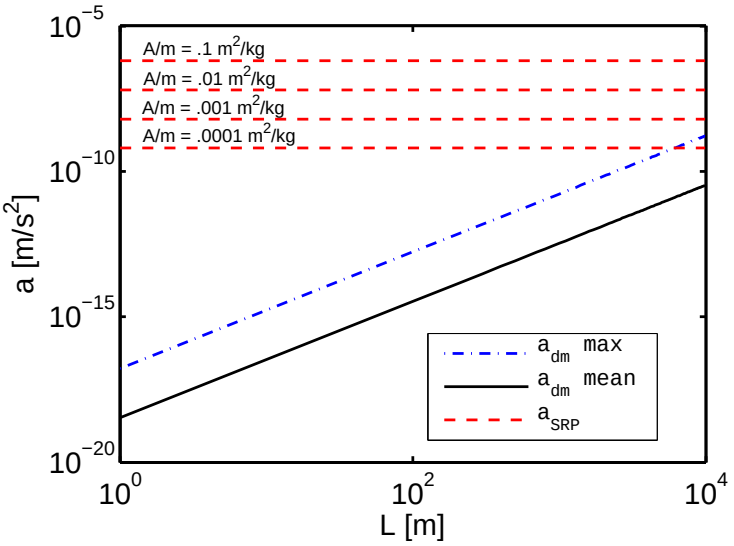

Figure 4.18: Comparison of accelerations a_{SRP} and a_{dm} provoked respectively by the solar radiation pressure and the gravity gradient force along a large Lyapunov orbit about L_1.

Unlike the orbital components, the angular acceleration due to a distributed mass may still be comparable to the action of the solar radiation pressure. Hence, eq. (4.10) can be rearranged to provide an estimation of the angular acceleration exerted by the solar radiation pressure:

$$h_{SRP} = -4.5 \times 10^{-6}(1+c)Ar/I \quad , \tag{4.10}$$

where r is the distance between the center of pressure and the center of mass of the configuration and I is the spacecraft inertia around the spin axis. Thus, h_{SRP} is compared with the angular acceleration h_{dm} due to the distribution of mass as function of the inertia ratio k_3: in Figure 4.20 for a body on a large orbit from the L_1 family, in Figure 4.21 for body on a small orbit from the L_1 family. This time, in both Figure 4.20 and 4.21 the gap among the two perturbations is significantly reduced to the extend that h_{dm} overcomes h_{SRP} in certain situations. Furthermore, more horizontal lines for lower values of Ar/I could be plotted. In fact, it is not unlikely to have a center of pressure very close to the center of mass, resulting in $r \to 0$. Finally, it is worth to note in Figure 4.20 the serious difference between the mean and the maximum value of h_{dm} over a large Lyapunov orbit (also present on the transitional acceleration a_{dm} in Figure 4.18). This contrast among the mean and the maximum value is an index of the nonlinear nature of the large Lyapunov orbits.

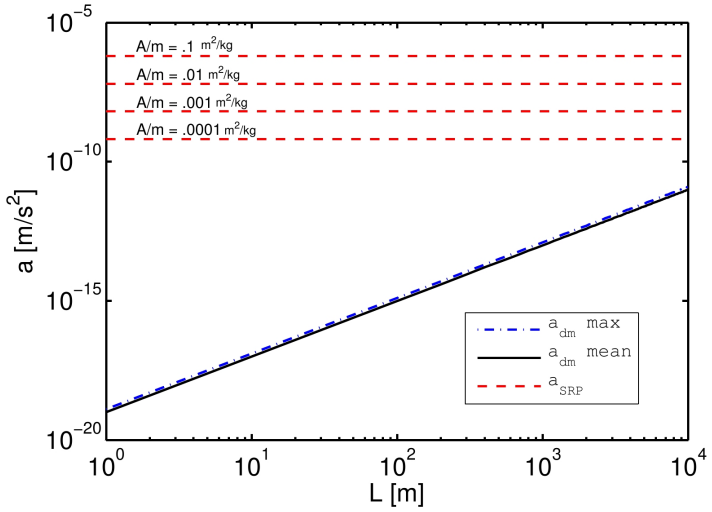

Figure 4.19: Comparison of accelerations a_{SRP} and a_{dm} provoked respectively by the solar radiation pressure and the mass distribution force along a small Lyapunov orbit about L_1.

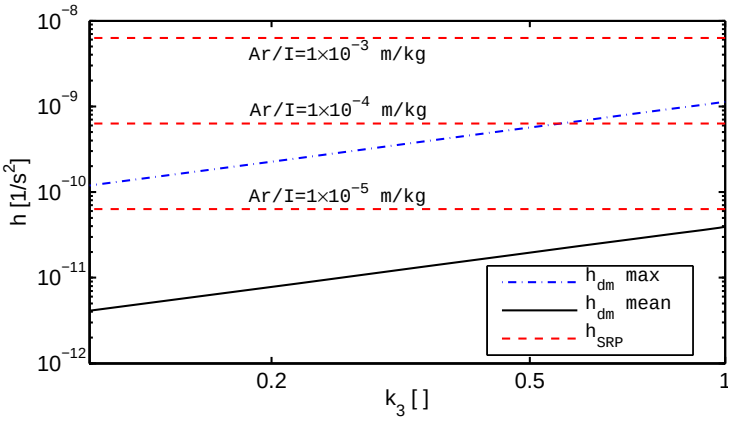

Figure 4.20: Comparison of angular accelerations h_{SRP} and h_{dm} provoked respectively by the solar radiation pressure and the mass distribution torque along a large Lyapunov orbit about L_1.

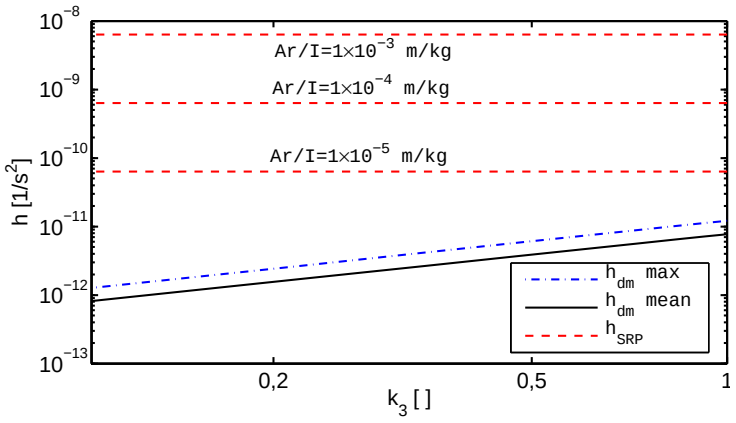

Figure 4.21: Comparison of angular accelerations h_{SRP} and h_{dm} provoked respectively by the solar radiation pressure and the mass distribution torque along a small Lyapunov orbit about L_1.

5

Rigid Fully-Coupled Motion under Solar Radiation Pressure

Contents

The parallel with the solar radiation pressure in the previous Chapter has stressed the influence of such perturbation on the spacecraft dynamics (especially on the orbital component). Moreover, it becomes truly critical for Large Space Structures (LSS) in three-body gravitational scenario. The solar radiation always affects the motion of satellites close enough to the Sun, since it is intrinsic of the operative environment; however, further factors makes this disturbance challenging in the mission analysis of LSS. Trivially, the solar radiation pressure is the strongest external perturbation in vicinity of libration points. In addition, the orbital motion around those points is well-know to be highly instable, making the station keeping problem one of the principal causes of fuel consumption, especially on long operative life. Finally, it can be plausibly assumed that LSS require large amount of power, that is likely to be provided by solar arrays, so the cross-sectional area exposed to the solar radiation increases quickly for these architectures. With these premises, it would be of great interest to identify solutions of the uncontrolled fully-coupled dynamics under the solar disturbance which drastically reduce the station keeping cost. To this end, in

the Section 5.1 of this Chapter, the model of the solar radiation pressure is described; then, in Section 5.2, the design of periodic orbits for LSS in vicinity of the L_1 point of the Sun-Earth system is presented. Likewise, the same problem is addressed in Section 5.4 for the Earth-Moon system, but radically different strategies are proposed.

5.1 Solar Radiation Pressure Model

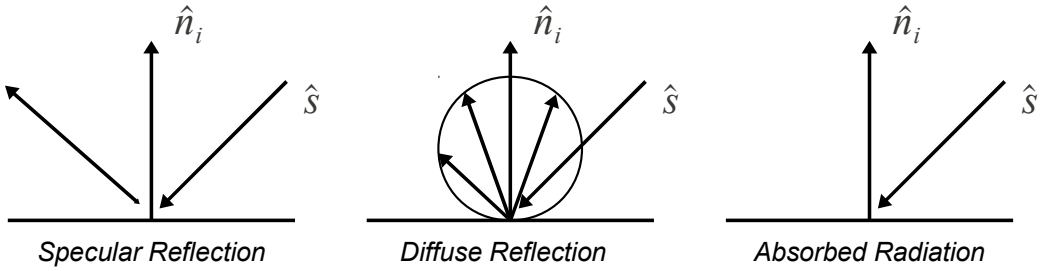

Figure 5.1: Possible interactions of the incident radiation.

The solar radiation incident on the exposed surfaces of the spacecraft exerts a pressure that surely transforms into a disturbing force and probably into an external moment as well, according to the relative position between the center of pressure and the center of mass. The total pressure depends on the type of interaction between the radiation and the surface. Assuming opaque surfaces for the rest of this work, three kinds are classified and depicted in Figure 5.1: specular reflection, diffuse reflection, absorption of the radiation. Each one introduces a different force on an infinitesimal area dA_i of the i-th surface exposed:

$$\boldsymbol{dF_a} = -Pc_a^i \cos\alpha_i \hat{\boldsymbol{s}}\, dA_i \qquad \alpha_i \in [-\pi/2, \pi/2] \qquad (5.1)$$

$$\boldsymbol{dF_d} = Pc_d^i \left(-\frac{2}{3}\cos\alpha_i \hat{\boldsymbol{n}}_{\boldsymbol{i}} - \cos\alpha_i \hat{\boldsymbol{s}} \right) dA_i \qquad \alpha_i \in [-\pi/2, \pi/2] \qquad (5.2)$$

$$\boldsymbol{dF_s} = -2Pc_s^i \cos^2\alpha_i \hat{\boldsymbol{n}}_{\boldsymbol{i}}\, dA_i \qquad \alpha_i \in [-\pi/2, \pi/2] \qquad (5.3)$$

where the subscripts a, d, s, denote respectively the absorbed, diffusively reflected and specularly reflected radiation; P is the mean radiation pressure at a given distance from the Sun r_{AU}, computed from the value at one astronomical unit (AU) $P_{1AU} = 1358\text{W/m}^2$ as

$$P = \frac{P_{1AU}}{r_{AU}^2} \quad , \qquad (5.4)$$

with r_{AU} expressed in astronomical units; α_i is the angle between the incident direction $\hat{\boldsymbol{s}}$ and the surface normal $\hat{\boldsymbol{n}}_{\boldsymbol{i}}$, defined by

$$\alpha_i = \cos^{-1}(\hat{s} \cdot \hat{n}_i) \quad ; \tag{5.5}$$

c_a^i, c_d^i, c_s^i represent the radiation coefficients of the opaque surface and shall fulfill the relationship

$$c_s^i + c_d^i + c_a^i = 1 \quad . \tag{5.6}$$

Adding up all the contributions due to different types of interaction from eq. (5.1)-(5.3) and exploiting eq. (5.6), the total force provoked by the solar radiation on the i-th surface is given by

$$\boldsymbol{F_i}^{SRP} = -P \int_{A_i} \left[(1 - c_s^i)\hat{\boldsymbol{s}} + 2 \left(c_s^i \cos\alpha_i + \frac{1}{3} c_d^i \right) \hat{\boldsymbol{n}}_{\boldsymbol{i}} \right] \cos\alpha_i \, dA_i \quad . \tag{5.7}$$

The attendant moment of $\boldsymbol{F_i}$ is found by the cross product

$$\boldsymbol{M_i}^{SRP} = \boldsymbol{b_i} \wedge \boldsymbol{F_i}^{SRP} \quad , \tag{5.8}$$

where $\boldsymbol{b_i}$ is the position vector of the center of pressure on the ith surface relative to the spacecraft center of mass.

5.2 Sun-Earth System

In this section is presented the construction of displaced solar Lyapunov periodic orbits for solar arrays powered space stations with passive station keeping in vicinity of the Sun-Earth L_1 point. A spacecraft orbiting the first Sun-Earth equilibrium point would have constant and generous supplying of power via solar arrays, which are a completely reliable technology. Additionally, the thermal environment would be easily predictable and controllable. These reasons are sufficient to consider the L_1 neighborhood a profitable site for gateway stations, Sun observers and even solar plants. Unfortunately, the same source of power is also the source of the main orbital disturbance, which combined with a truly unstable dynamics, leads to the challenge of keeping the designed trajectory. To solve this issue without adopting active techniques, it is exploited a model for the solar sails dynamics and it is demonstrated applicable to the mission analysis of space stations in the L_1 Sun-Earth point. The orbital-attitude fully coupled dynamics is leveraged to obtain a passive station keeping of the solution.

Describing the design process developed in this work, a specific vehicle configuration will be referred, whose characteristics are close to those of

the International Space Station. This choice should not only guarantee clearness of explanation but also provide an useful quantitative picture of the results for a general purpose architecture. As it will be evident at the end, it is straightforward reproducing the process with configurations of major concern for the reader. Anyway, the addressed space station layout is sketched in Figure 5.2. Basically, it is consisting of a central rectangular module (assuming uniform distribution of mass) and two identical massless branches of solar arrays; their features are tabled in 5.1, where m, L, w, A_{sa}, b denote in the order mentioned: the total spacecraft mass, the central module length and width, the solar array area for a single branch and the distance between the branch center of solar pressure C_p and the spacecraft center of mass CoM. The two centers of pressure and the configuration center of mass are hypothesized to be aligned along the $\hat{b}_2$ axis of the b-frame, whose origin corresponds to CoM. The adopted pattern of surfaces exposed to the solar radiation pressure is such that the attendant torque is null. Because of its I shape, this configuration will labeled as I-Shaped Station (I-SS).

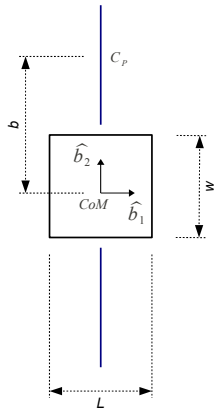

Figure 5.2: Schematic picture of the I-SS configuration.

Table 5.1: I-SS configuration data.

Spacecraft		**Solar Array**	
m [tons]	400	A_{sa} [m^2]	2000
L [m]	100	b [m]	80
w [m]	100	c_s [ ]	0.4
k_3 [ ]	0	c_d [ ]	0.4

If the I-SS is placed on a Lyapunov periodic orbit of the L_1 Sun-Earth

family, the station will certainly depart from the unperturbed trajectory within an orbital period as consequence of the solar radiation pressure. This happens regardless the orbit size as shown in Figure 5.3.

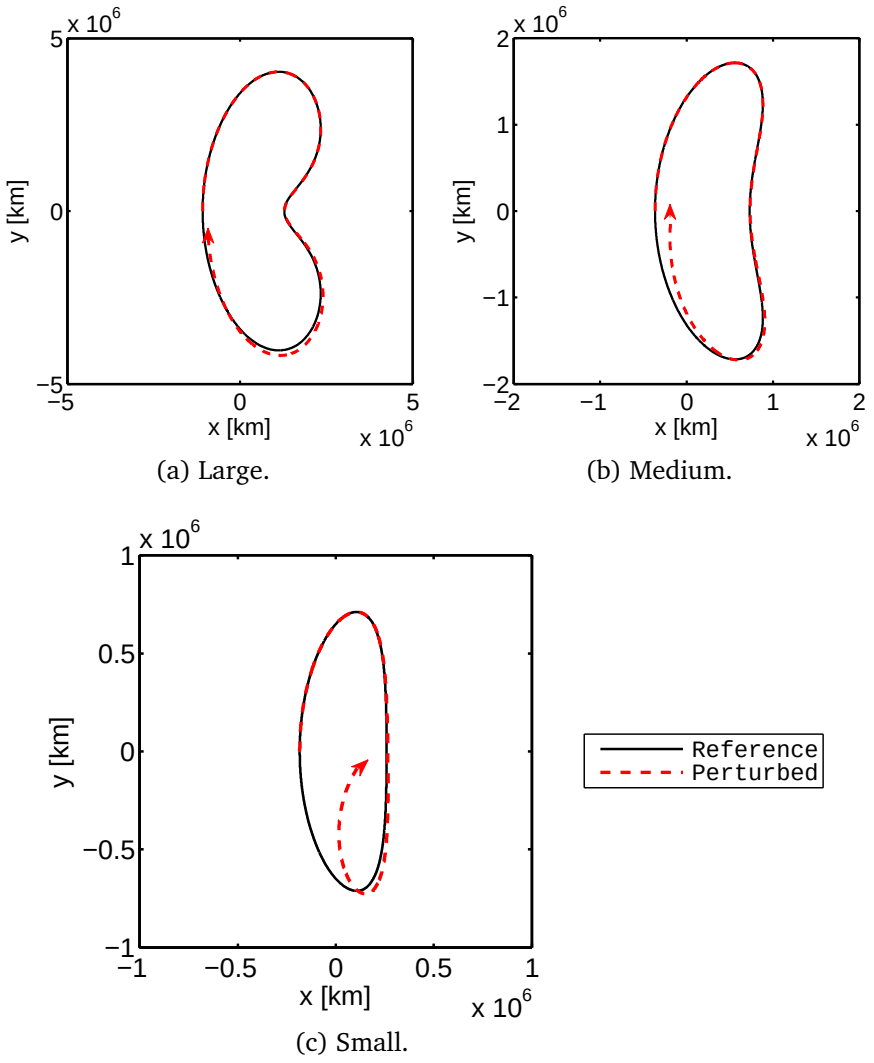

(a) Large.

(b) Medium.

(c) Small.

Figure 5.3: Drift from classic Lyapunov orbits about L_1 induced by the solar radiation pressure.

Despite the solar radiation pressure cannot be annihilated without a active rejection, at least it can be incorporated in the dynamic model and provide meaningful solutions under certain conditions. The mere addiction of the perturbation as an external action to the equations of motion does not lead to an useful insight, but simply alters the proprieties of the original

system. Above all, the problem is no longer conservative. However, it is still autonomous because the solar radiation has a constant direction when observed in the rotating frame. From this basis, McInnes shows [76] that the equation of motions developed to study the dynamics of solar sails can be derived by a potential expression modified to account the solar force. Unfortunately, this is possible only with a specif framework of assumptions:

1. the solar sail is flat and perfect reflective (no absorption or diffusive reflection).
2. the solar sail is modeled as a infinitesimal mass point and its attitude dynamics is not accounted in the equations of motion.
3. the solar sail normal is always direct toward the Sun and aligned with the Sun-Spacecraft line.
4. the solar sail area is constant during the whole motion.

These hypothesis lead to the equation of motions

$$\begin{cases} \ddot{x} = & 2\dot{x} + x - (1-\mu)(1-\beta)\dfrac{x+\mu}{r_1^3} - \mu\dfrac{x-1+\mu}{r_2^3} \\ \ddot{y} = & -2\dot{y} + y - (1-\mu)(1-\beta)\dfrac{y}{r_1^3} - \mu\dfrac{y}{r_2^3} \end{cases} , \tag{5.9}$$

which are expressed in the non-dimensional coordinates x, y of the classical synodic frame defined in Chapter 2 (whose origin is fixed in the center of mass of the planetary system rather than in the Lagrangian point, as for the ℓ-frame). r_1 and r_2 represents the distance from P_1 and P_2 respectively, while μ is the mass parameter. The variable describing the solar sail interaction with the radiation is β, the so-called dimensionless sail lightness parameter. β is defined as the ratio of the solar radiation pressure acceleration to the solar gravitational acceleration. The lightness parameter does not depend on the distance from Sun, because both accelerations are assumed to be inversely proportional to that distance.

As anticipated earlier, the system of equations (5.9) relies on the modified pseudo-potential

$$\bar{U}_\beta = \frac{1}{2}(x^2+y^2) + \frac{(1-\mu)(1-\beta)}{r_1} + \frac{\mu}{r_2} \quad , \tag{5.10}$$

which has three stationary solution on the axis $y = 0$, given by solving the roots of

$$f = x - (1-\mu)\frac{(1-\beta)(x+\mu)}{(x+\mu)^3} - \mu\frac{x-1+\mu}{(x-(1-\mu))^3} \quad . \tag{5.11}$$

Detailed in [77], the equilibrium positions of solar sails in the RC3BP does not necessarily lie on the P_1-P_2 line, but are function of the sail orientation respect the radiation direction. On the other hand, when the exposed surface is perpendicular to the Sun-spacecraft line, the equilibrium points are located at $y = 0$ as in the classical problem and can be computed as the zeros of eq. (5.11). It turns out that they are just displaced forward the Sun by a shift subordinate to the β value. These particular solutions are often referred as artificial on-axis libration points. The name itself anticipates that periodic orbits still exist around the new equilibria. In fact, a proper stability analysis demonstrates [76] that the original qualitative nature of the problem is preserved and periodic orbits survive in a modified form. For example, Figure 5.4 depicts a planar Lyapunov periodic orbit around the artificial L_1 (clearly moved forward respect its classical location) for $\beta = 0.051689$ and the Jacobi constant $JC = 2.8956695$ (which is calculated accounting the modified version of the pseudo-potential). As proof of validity, in the plot the same orbit appears also as computed by Farres in [78].

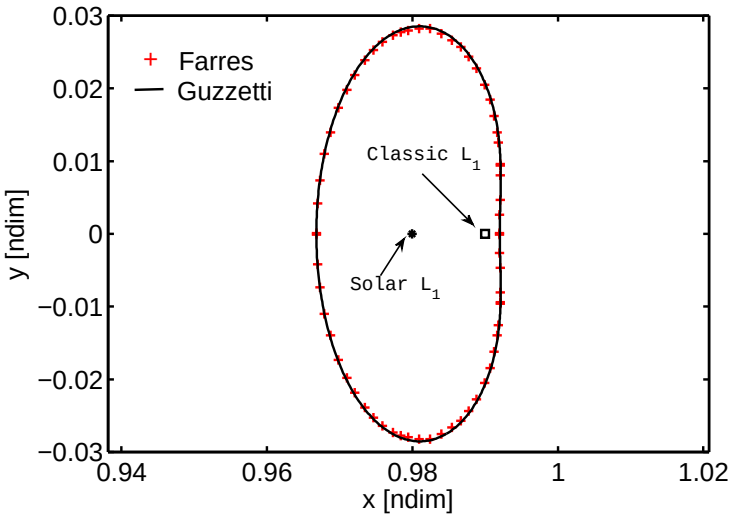

Figure 5.4: Displaced Lyapunov periodic orbit around the artificial L_1 point. Configuration space on the basis of the standard synodic frame.

Although periodic orbits result to be a possible solution of the equation of motions (5.9), similarly to the unperturbed dynamical model, they are owing to the set of hypothesis developed specifically for the solar sails dynamics. Thus, further considerations are necessary before extending their employment to standard vehicles without sails. First of all, the perfect reflection of the solar radiation on the exposed surface (*i.e* $c_s = 1$) is not

authentic for a general opaque covering. In fact, other two types of interactions occur beside the specular reflection: the absorption or the diffusive reflection of part of the total incident radiation. As discussed in the previous Section, each type of interaction translates into forces different for magnitude and direction; adding up all the contributions, the total force on a general surface is not equal to the force on the equivalent specular area, both in terms of intensity and orientation. If the force exerted by the solar radiation pressure changes, the solution and even the equations of motions will do too. Therefore, the periodic orbits may disappear in the dynamics of classical spacecraft. But, if it is possible to demonstrate that a space structure with general surfaces exposed to the solar radiation and an equivalent flat specularly reflective solar sail result in the same solar force vector during the entire motion, eq. (5.9) and their solutions will be true again. In other words, the total force shall correspond in magnitude and direction between the two models of radiation interaction. To this end, the lightness parameter β shall be computed according to the actual force on each exposed surface

$$\beta = \frac{|\boldsymbol{R}_1|^2}{\mu_1 m} \sum_i^{n_S} |\boldsymbol{F}_{\boldsymbol{i}}^{SRP}| \quad , \tag{5.12}$$

where n_S is the total number of surfaces, $\boldsymbol{F}_{\boldsymbol{i}}^{SRP}$ is defined in eq. (5.7), $|\boldsymbol{R}_1|$ denotes the distance from the Sun and μ_1 its planetary constant; m stands for the total spacecraft mass. The range of β for configurations without solar sails is about $[10^{-6}, 10^{-4}]$, while a design range for sails is between a conservative $\beta \approx 0.03$ and an optimistic $\beta \approx 0.3$ [76]. Figure 5.5 shows the displacement of the artificial L_1 point (solution of eq. (5.11)) for the effective β in the range of a standard spacecraft.

So far, given an arbitrary spacecraft, the resultant exerted by the solar pressure is equivalent in terms of euclidean norm to the force generated by a solar sail with lightness factor computed from eq. (5.12), but not in terms of orientation. Let us consider two surface: a perfectly specular surface (like the solar sail) and another non-perfectly specular. On the perfectly specular surface the solar radiation pressure provokes a force in the direction of the normal $\hat{\boldsymbol{n}}_{\boldsymbol{i}}$ of the surface; on the non-perfectly specular surface the resultant is made up of components in the direction $\hat{\boldsymbol{n}}_{\boldsymbol{i}}$ and in the direction of the incident radiation $\hat{\boldsymbol{s}}$, as obvious from eq. (5.1). Therefore, considering these two type of surfaces, the only chance to obtain the same orientation of the resultant is when $\hat{\boldsymbol{n}}_{\boldsymbol{i}}$ matches $\hat{\boldsymbol{s}}$. This happens when the surface is orthogonal to the incident radiation. Luckily, this condition is

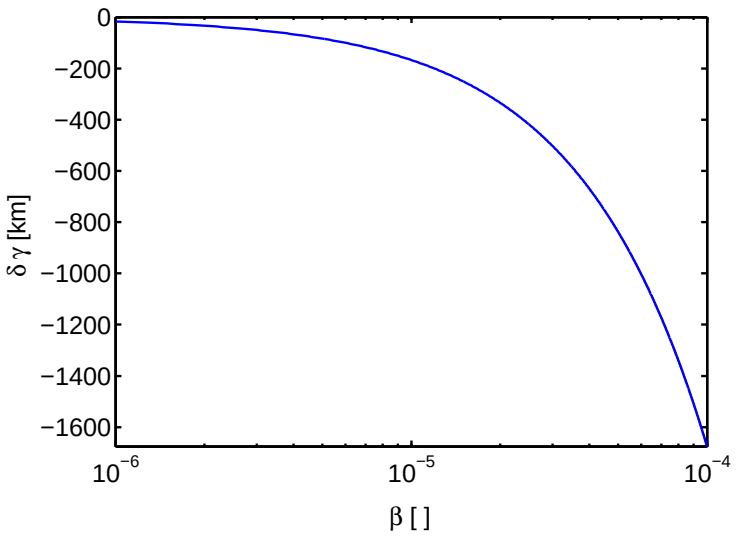

Figure 5.5: Displacment of the artificial L_1 point as function of the lightness parameter for solar arrays powered satellites.

contained in the framework of hypothesis leading to the model presented for solar sails (*i.e* equations of motion (5.9)). Hence, as long as the surface is perpendicular to the Sun-spacecraft line and the lightness parameter is computed properly, the solutions of the model (*i.e.* periodic orbits) remain legitimate for a non-perfectly reflective surface too. The concept is easily applicable also to a typical satellite constituted by different surfaces: the configuration of exposed surfaces is required to be symmetrical respect to an arbitrary axis. At this point, it is sufficient to have such axis aligned with the solar radiation vector, so that the total effective cross-sectional area of the configuration becomes normal to the Sun-spacecraft line. The symmetry is a sufficient condition to cancel all the components not directed as $\hat{\boldsymbol{s}}$.

The periodic orbits generated including the thrust due to the solar radiation $\boldsymbol{F}^{SRP} = \sum_i^{n_S} \boldsymbol{F_i}^{SRP}$ assume no external torques on the spacecraft, and its orientation perfectly controllable in order to maintain $\boldsymbol{F}^{SRP} \equiv \hat{\boldsymbol{s}}$. However, this may not be the case for an arbitrary space structure under its uncontrolled fully-coupled dynamics. The natural evolution of the attitude motion may lead to slight deviations from the correct alignment of the vehicle with respect to the Sun-spacecraft line. To appreciate the consequences of attitude misalignments on the orbital trajectory, it is worth to recall the I-SS configuration. Accordingly to data in Table 5.1, it is hypothesized that the solar arrays are the only surfaces interacting with the solar radiation. Additionally, the body is axisymmetric ($k_3 = 0$), therefore the

gravity gradient torque is null, and the local body coordinate system, the b-frame, corresponds to the principal axes of inertia. Next, the study addresses three sizes of artificial Lyapunov periodic orbits: a large orbit with period 311 days, a medium orbit with period 198 days and a small orbit with period 177 days.

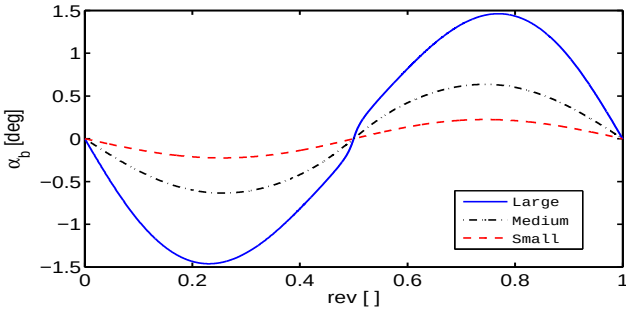

(a) Trend for the I-SS along different artificial Lyapunov orbits.

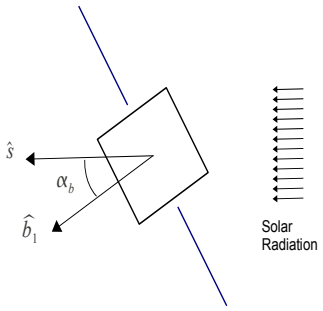

(b) Sketch.

Figure 5.6: Misalignment angle α_b.

The exposed surfaces of the I-SS are a symmetrical configuration relatively to the $\hat{b}_1$ axis, therefore it is necessary to maintain $\hat{b}_1$ aligned with $\hat{\boldsymbol{s}}$ in order to satisfy the conditions underlying the existence of the artificial Lyapunov orbit. However, small variations occur around the desired pointing condition when the actual uncontrolled attitude dynamics is studied. Figure 5.6-(a) reports the misalignment angle α_b of $\hat{b}_1$ relative to $\hat{\boldsymbol{s}}$ (see Figure 5.6-(b)), defined positive when counterclockwise. Introducing this pointing error the spacecraft undergoes an evident departure from the artificially displaced periodic orbit. In fact, the final radial displacement after one period, see Table 5.2, is smaller than that experienced in the classical formulation of the problem, but it is still large enough to lose the nominal trajectory in the following revolution.

Table 5.2: Final Radial Displacement of the I-SS for different artificial Lyapunov orbits.

	Large	**Medium**	**Small**
Classic	1.4×10^7 m	-1.8×10^8 m	-4.5×10^7 m
Artificial	1.8×10^6 m	1.5×10^5 m	1.2×10^5 m

To enable the spacecraft to passively target the Sun, an idea proposed

for the solar sails design is exploited again. In fact, different recent papers [79, 80] suggest tailoring the sail shape as an effective passive mean to impose the desired attitude along the orbit. The concept employed here is the simplest possible and it is inspired by the work of Kirpichnikov et al. [81]: the attitude of a conic surface exposed to the solar radiation is stable around the direction of the incident radiation. In the plane, this is equivalent to a two-folding surface formed by two equally inclined branches. Thus, the I-SS is modified rotating symmetrically both the solar arrays around their center of pressure by an angle δ_{sa}, as sketched in Figure 5.7. Without need to explain the name, the vehicle in its new configuration will be referred as V-Shaped Station (V-SS). In the following investigation, this configuration will replace the I-SS on the same orbits chosen earlier. At this point, after the rotation δ_{sa}, the solar arrays area shall be increased to keep the effective lightness parameter equal to the original value of the I-SS, otherwise the aforementioned periodic orbits would not represent the exact nominal trajectory. As a matter of fact, each artificial periodic orbit is uniquely linked to a value of β. Also, let us introduce the gravity gradi-

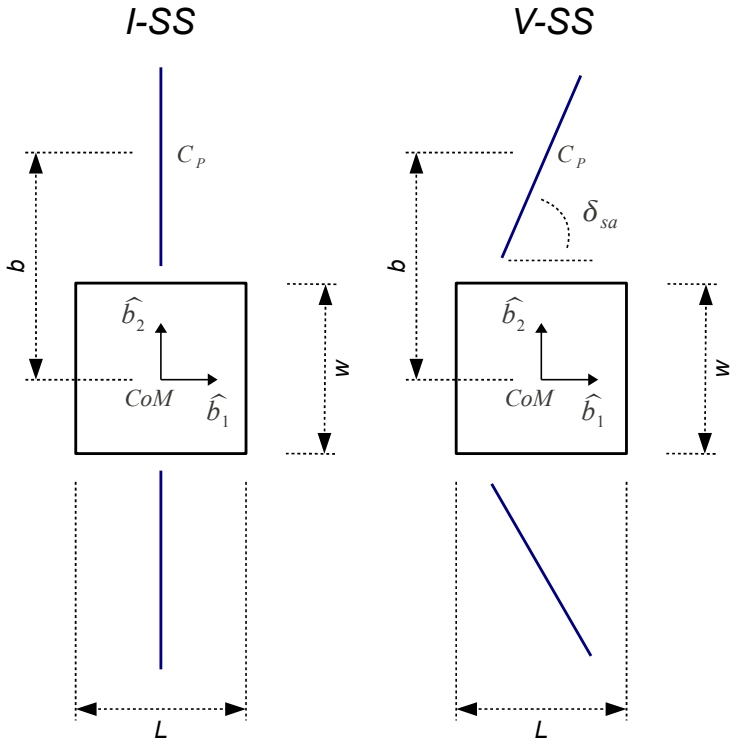

Figure 5.7: Schematic picture of the V-SS configuration.

ent torque, waiving the constrain of axisymmetric distribution of mass. For this purpose, the width of the central module can vary from 0 m (beam-

like geometry, $k_3 = 1$) to 100 m (axisymmetric geometry, $k_3 = 0$). Initially, simulations are performed for the V-SS with $\delta_{sa} = 45°$. Results shown in Table 5.3 demonstrate that the drift after one revolution of the V-SS from the periodic orbit is minimal, regardless the orbit size or the inertia ratio of the analyzed cases. This is an indirect clue that V-SS is able, at least for the examined conditions, to passively aim at Sun along the entire orbit. Therefore, all the assumptions underlying the existence of the periodic orbit are satisfied during the entire motion, and straightforwardly the dynamics respects the prediction of the model. A periodic orbit has been eventually designed fully incorporating the solar radiation pressure both in terms of orbital and attitude motion.

Table 5.3: Final Radial Displacement of the V-SS ($\delta_{sa} = 45°$) for different artificial Lyapunov orbits.

	$k_3 = 0$	$k_3 = 0.5$	$k_3 = 1$
Large	-10 m	-105 m	-153 m
Medium	-3 m	-77 m	-111 m
Small	-2.5 m	-119 m	-177 m

Despite the V-SS with $\delta_{sa} = 45°$ proves to adequately maintain both the desired trajectory and pointing, such inclination of the solar arrays is highly inefficient, as the effective area to generate electric power is considerably smaller than the actual array extension, because of the inclination itself relative to the incident radiation (directed as $\hat{b}_1$). However, δ_{sa} is reduced down to $5°$ without sensibly making things worse, as confirmed by the values of the radial displacement after one period in Table 5.4. Of course, a lower δ_{sa} reduces the promptness of control with consequent larger shift from the orbit, especially under a stronger gravity gradient (see Figure 5.8). Stated in other terms, larger attitude errors result in larger orbital errors. But again, even in the worst case faced, the orbital errors are intangible as shown in Figure 5.9.

The last part of the study aims at figuring out how the inclination of the solar arrays affects the libration dynamics around the nominal pointing condition toward the Sun. Furthermore, fixed the inclination, the response may still vary considerably according to the mass distribution topology and the orbit size. For inertially axisymmetric spacecrafts ($k_3 = 0$) the oscillations around $\alpha_b = 0°$ are guaranteed to be extremely small, regardless either the orbit size or the solar arrays tilt. Something different is observed

Table 5.4: Final Radial Displacement of the V-SS ($\delta_{sa} = 5°$) for different artificial Lyapunov orbits.

	$k_3 = 0$	$k_3 = 0.5$	$k_3 = 1$
Large	196 m	2890 m	3850 m
Medium	79 m	1510 m	2230 m
Small	68 m	2320 m	3490 m

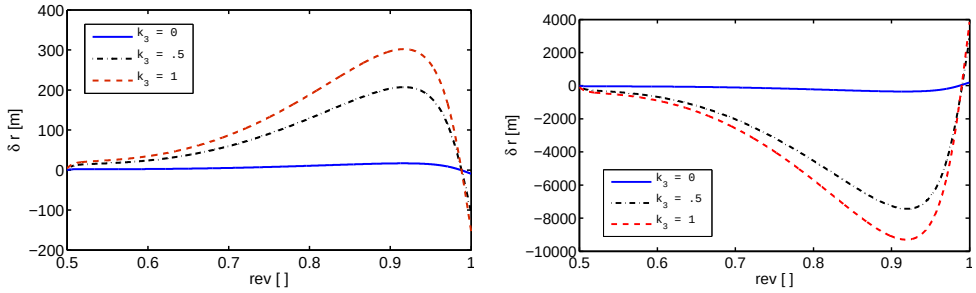

(a) $\delta_{sa} = 45°$ (b) $\delta_{sa} = 5°$

Figure 5.8: Radial Displacement of the V-SS on a large artificial Lyapunov orbit.

for truly anisotropic mass distribution ($k_3 = 1$). On small or medium size orbit the dissimilarity is meager: the oscillations are not exactly around the nominal pointing, but there is a tiny bias, function of the orbital position of the spacecraft. The more the orbit size increases or the solar array angle decreases, the more the phenomenon becomes tangible, as shown in Figure 5.10. Not surprisingly, if the control is soften because of a lower solar arrays tilt or the disturbance is strengthen because of a larger orbit, then the bias error is augmented.

Unlike for small and medium orbit sizes, the attitude response of an highly anisotropic body is characterized by a critical dependence on the solar array inclination. To begin with, it is worth to recall the behavior of an axisymmetric spacecraft. Referring to Figure 5.11-(a), the solar arrays tilt changes only the frequency and the amplitude of the pitch motion, without altering the nature of the solution. The reduction in frequency and the simultaneous amplification of the oscillation for $\delta_{sa} = 5°$ only suggests that a lower solar arrays inclination leads to a weaker and slower control. Conversely, in Figure 5.11-(b) can be noticed a totally different trend when a anisotropic space structure on a large orbit is equipped with solar array mounted at $\delta_{sa} = 5°$ or at $\delta_{sa} = 45°$. In the former case, the motion starts

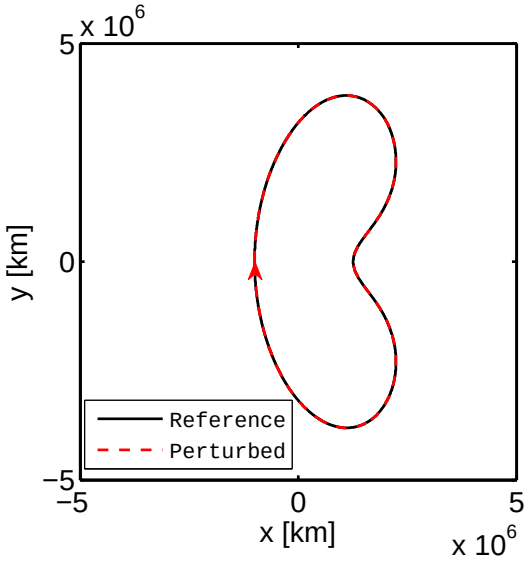

Figure 5.9: Large artificial Lyapunov orbit in the most critical configuration of the V-SS ($\delta_{sa} = 5°$, $k_3 = 1$). Configuration space on the basis of the ℓ-frame.

similarly to the other responses discussed, but at half revolution the amplitude of librations rises abruptly; in the latter case, it is instead only noticeable a perturbation of the oscillations that is rapidly reabsorbed. However, in both the circumstances the cause is the close encounter of the secondary and the P_1-P_2 line crossing. An alternative picture of the phenomenon is offered observing the phase diagrams in Figure 5.12. For $\delta_{sa} = 45°$ the phase pattern is altered but not destroyed by the events at 0.5 revolutions; on the contrary, for $\delta_{sa} = 5°$ the destruction of the initial structure of motion (shown in Figure 5.13) is evident and leads to a new cycle of oscillations.

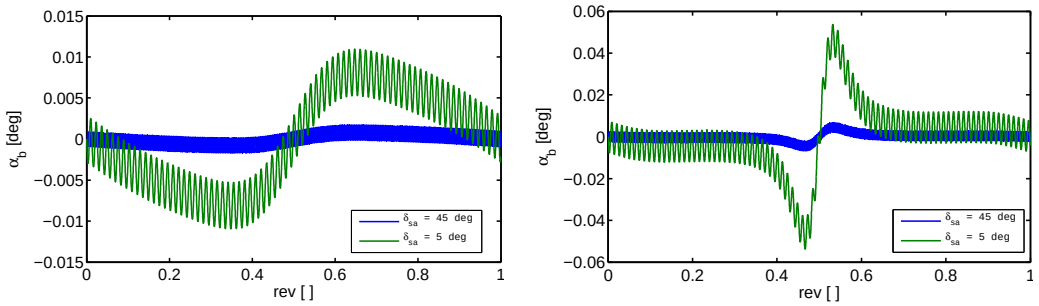

(a) Small. (b) Medium.

Figure 5.10: Attitude pointing error of an anisotropic spacecraft ($k_3 = 1$) along Lyapunov periodic orbits with different size.

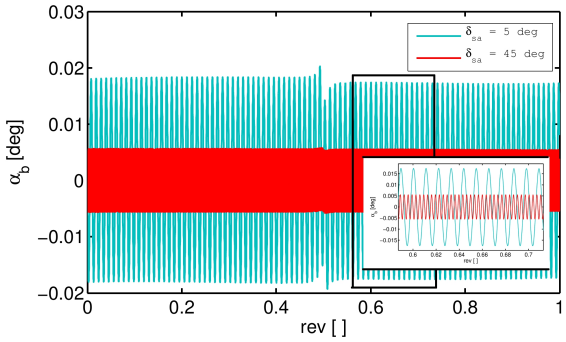

(a) Axisymmetric ($k_3 = 0$).

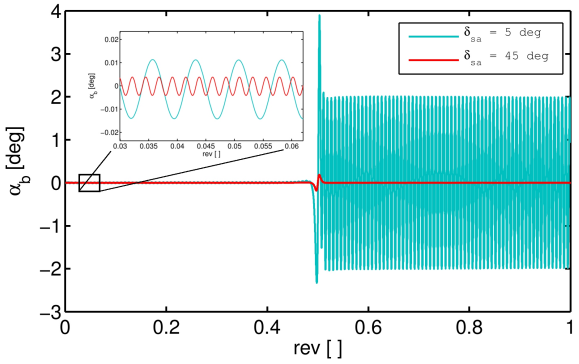

(b) Anisotropic ($k_3 = 1$).

Figure 5.11: Attitude pointing error along a large Lyapunov periodic orbit for different spacecraft topology.

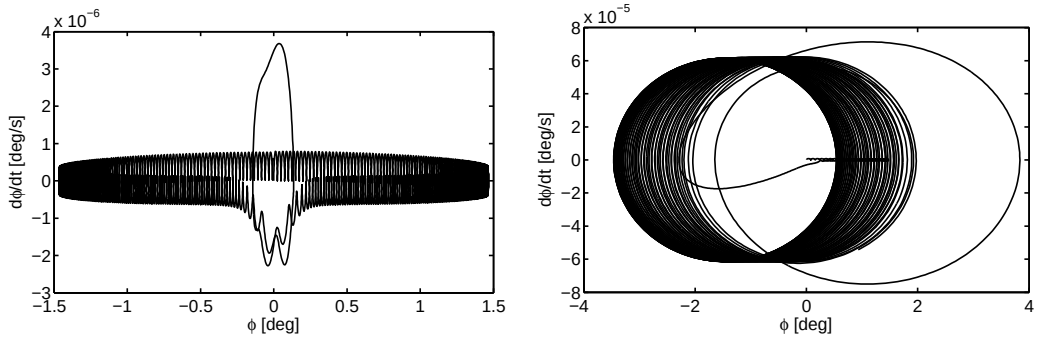

(a) $\delta_{sa} = 45°$. (b) $\delta_{sa} = 5°$.

Figure 5.12: Attitude phase portrait of an anisotropic spacecraft ($k_3 = 1$) orbiting a large Lyapunov periodic orbit, considering different solar arrays tilt.

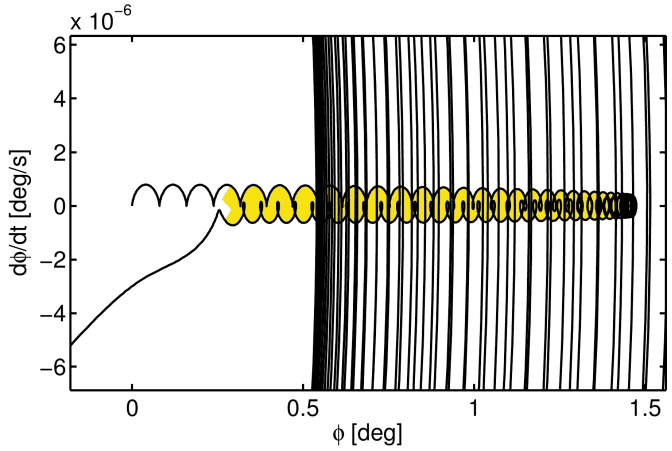

Figure 5.13: Zoom of the attitude phase portrait of an anisotropic spacecraft ($k_3 = 1$) orbiting a large Lyapunov periodic orbit, considering a solar arrays tilt $\delta_{sa} = 5°$.

5.3 The Secondary Anomaly

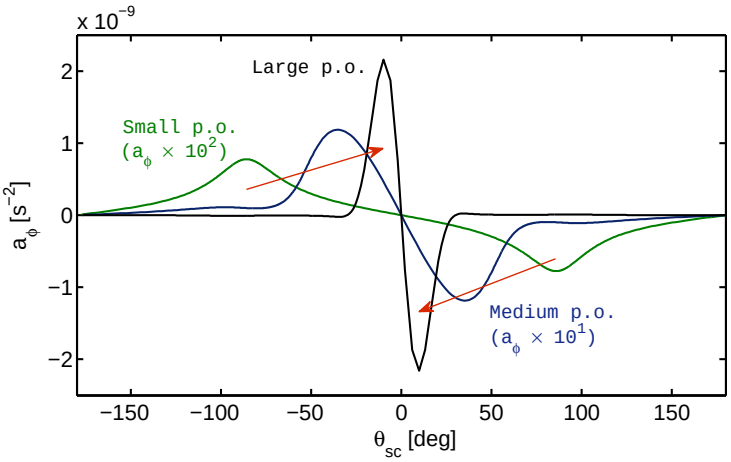

(a) L_1 family.

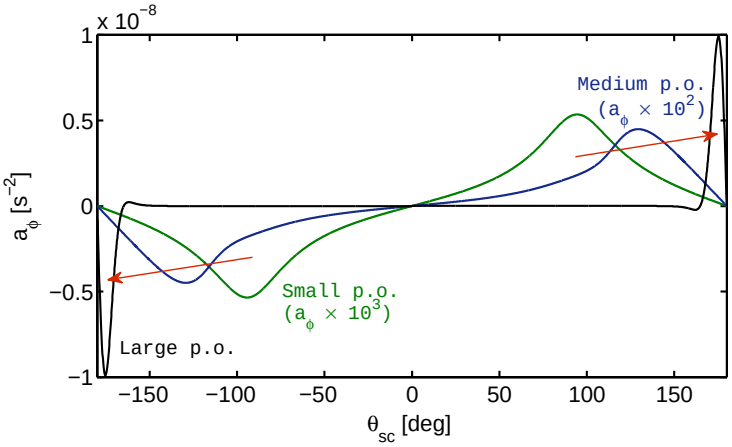

(b) L_2 family.

Figure 5.14: Evolution of the external acceleration on different Lyapunov periodic orbits.

By concluding the preceding Section, it was noticed that the attitude phase portrait related to a large Lyapunov orbit was critically altered after the crossing of the attractors line nearby P_2. As the size of the orbit increases, it is known that the orbital motion relies upon a truly nonlinear dynamics; thus, to have a deeper insight on the coupled attitude dynamics in a nonlinear regime, the angular acceleration trend due to gravity and fictitious momenta is studied along the trajectory. This acceleration is basically the action exerted by the external actions, which, recalling the eq.

(3.44), is given by

$$a_\phi = \frac{(Q_g)_\phi + (Q_\Omega)_\phi}{m_{\phi\phi}} \quad . \tag{5.13}$$

The orbital position will be identified in terms of anomaly θ_{sc}, which is defined as the spacecraft angular position relative to the ℓ-frame; specifically $\theta_{sc} = 0$ represents the vehicle on the right of the libration point and aligned with P_1 and P_2.

Regardless considering the L_1 or the L_2 family, a serious evolution of the solicitation regime is related to the orbit dimension. Along small nearly-linear orbits the a_ϕ trend experienced is characterized by a positive maximum and a negative minimum located respectively almost on $\theta_{sc} = \pm 90^\circ$, which corresponds to the maximum distance from the axis through the primary and the secondary; the trend is symmetric about the origin and the transition between the two picks is doubtlessly smooth. Enlarging the trajectory, the observed fashion undergoes a purely nonlinear mutation. Not only the singularity points strengthen their intensity, but also they move along the orbit, approaching $\theta_{sc} = 0^\circ$ in the L_1 family and $\theta_{sc} = 180^\circ$ in the L_2 family. That is, the picks shift from the point of maximum distance from the axis to the closest location to the secondary. This behavior is qualitatively displayed in Figure 5.14 for both the periodic orbits around L_1 or L_2. In particular, the plot is obtained assuming $k_3 = 1$ and $\phi = 0$ along the entire path. Furthermore, it should be noted that the curves referring to small and medium orbits are amplified in order to depict a clear visualization.

The phenomenon brought to light will be named Secondary Anomaly. More correctly, the name will be employed to address the circumstance of large Lyapunov periodic orbits where the intensity and the proximity of the singularities are such as to represent a serious and abrupt variation of the external momentum. In those cases, as a matter of fact, the solicitation changes from its maximum positive value to its negative minimum in a relatively short span of time; as shown in Figure 5.14, close to the anomaly, the slope of a_ϕ is almost vertical. The effects of a rapid mutation of the external action are assimilable to an impulsive disturbance, which is capable of transferring large amount of energy to all the oscillatory frequencies of the system. Thus, the secondary anomaly will be likely responsible for critically perturbing the spacecraft attitude and increasing the attendant control effort. Moreover, it might trigger significant vibrations of the most flexible elements of the structure too. For example, the orientation passive control by means of the solar radiation pressure, studied earlier, introduces a pseudo-elastic dynamics and the unexpected lowering of the pointing ac-

curacy is indeed due to the secondary anomaly.

5.4 Earth-Moon System

The design solution presented in the previous Section is not applicable in the Earth-Moon system. In the Earth-Moon system the dynamics is completely different from the Sun-Earth system because in the synodic frame the source of radiation is not fixed but rotates once per synodic lunar period. Mathematically, the dynamical system is no longer autonomous. To date, the only artificial periodic orbits incorporating the solar pressure in the Earth-Moon system have been identified for solar sails orbiting above the synodic plane [82]. In this Section, a particular orbit in the plane of the system will be proposed and studied for classical spacecrafts. The discovered orbit cannot be classified as periodic, but retains a surprising stability under the solar disturbance.

The intuition that will be investigated is to relate as much as possible the variation of the Sun position, which leads the system to be non-autonomous, and the spacecraft motion. To this end, the orbit with a period equal to the mean synodic lunar month is extracted from the Lyapunov periodic orbits family around L_1. Assuming in addition to neglect the inclination of the Sun above the Earth-Moon orbital plane and the annual variations of the synodic lunar month, each point of that orbit observes after a period the Sun in the same initial relative angular position $\Delta\theta$. Of course, as the orbital angular rate $\dot{\theta}_{sc}$ is not constant, $\Delta\theta$ varies along the trajectory before returning to its initial value after a revolution. This particular solution of the L_1 family will be named quasi sun-synchronous Lyapunov periodic orbit. The quasi sun-synchronous Lyapunov periodic orbit is represented in Figure 5.15, where also the meaning of some frequently recalled notation appears clearly.

Then, a further assumption is introduced: the configuration of the exposed surfaces has to be symmetrical with respect to an axis aligned with the Sun-spacecraft line throughout the motion. For convenience, the V-SS architecture (refer to the previous Section) will be initially considered. At $t = 0$ the V-SS is placed on the orbit left crossing of the P_1-P_2 axis and $\hat{b}_1$ is pointed exactly opposite to the Sun. In order to identify possible periodic orbits the difference between the initial and final state is monitored after one period T_{osc} in function of the initial solar phase $\theta_{sun}(t = 0)$. Trivially, if the discrepancy turns out to be null for a certain $\theta_{sun}(t = 0)$, it is a periodic

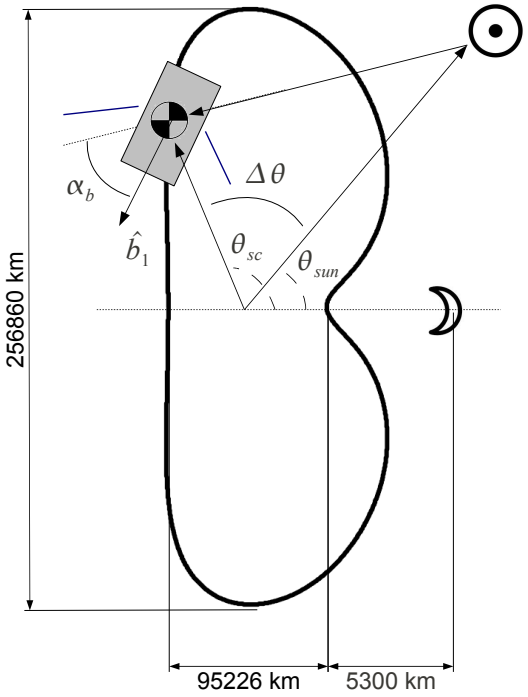

Figure 5.15: Quasi sun-synchronous Lyapunov periodic orbit from the L_1 family.

solution. The priority is given to errors in position

$$\Delta_x = x(T_{osc}) - x(0)$$

$$\Delta_y = y(T_{osc}) - y(0)$$

and velocity

$$\dot{\Delta}_x = \dot{x}(T_{osc}) - \dot{x}(0)$$

$$\dot{\Delta}_y = \dot{y}(T_{osc}) - \dot{y}(0) \quad ,$$

with x,y representing the coordinates of the spacecraft position in the configuration space; however, to address exact periodicity also the attitude and the sun position errors should be considered. Unexpectedly, a quite regular relationship between the initial Sun angular position and the errors in position and velocity appears in Figure 5.16. Moreover, all the curves seem to cross the zero in the neighborhood of two symmetric values of θ_{sun}. Unfortunately, the close inspection shown in Figure 5.17 reveals that each curve has different zeros; it means that the errors cannot be simultaneously null, implying the non-existence of periodic solutions. Despite that, the proximity of the zeros is still an excellent result. In fact, while selecting a value

of θ_{sun} to cancel one of the errors, the others will remain close to zero as well; likewise, an arbitrary objective function that weight each error may be minimized instead. Anyway, the obvious consequence of picking up a initial solar phase from the neighborhood, is the critical reduction of the station keeping effort, as all the errors to be corrected are much smaller.

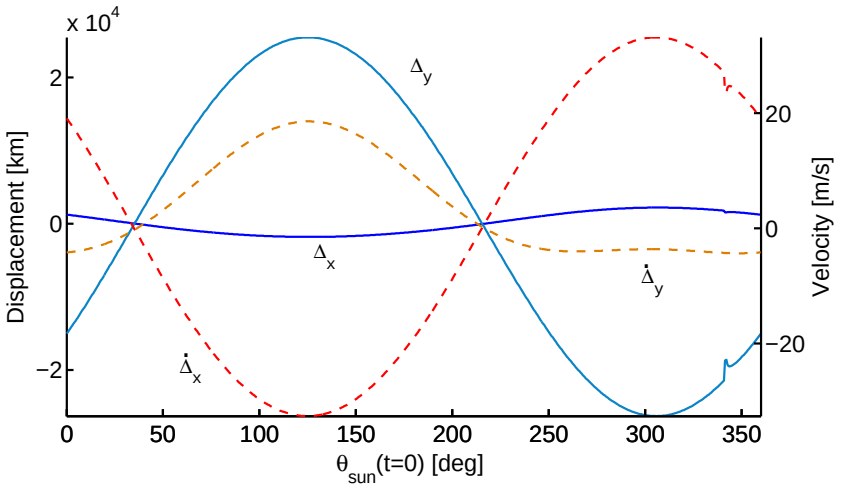

Figure 5.16: Position and velocity errors as function of the initial Sun phase.

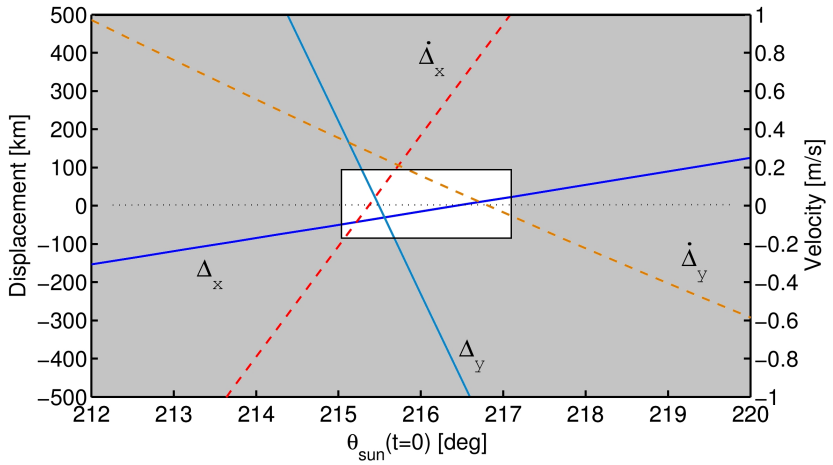

Figure 5.17: Near zero region of position and velocity errors.

It is particularly useful to express the errors at the next positive ($\dot{y} > 0$) crossing of the line joining the attractors, instead of considering one nominal period after the initial instant. Due to the disturbance of the solar

radiation the two events do not correspond as in the unperturbed dynamics. This slight change of perspective is motivated by the reason that the simplest algorithm of station keeping targets the perpendicular crossing of the axis through P_1-P_2. Therefore, monitoring the crossing in place of the nominal period offers a more meaningful picture of the strategy proposed. Hence, the new errors are defined as

$$\epsilon_x = x(\bar{t}) - x(0)$$

$$\epsilon_{vx} = \dot{x}(\bar{t})$$

$$\epsilon_{vy} = \dot{y}(\bar{t}) - \dot{y}(0) \quad ,$$

where $\bar{t}$ is the crossing temporal instant. It will also be considered the variation of the Sun angular position

$$\epsilon_{\theta_{sun}} = \theta_{sun}(\bar{t}) - \theta_{sun}(0) \quad .$$

The parallel of the crossing errors between typical periodic orbits of the L_1 family and a quasi sun-synchronous Lyapunov perturbed by the radiation pressure is reported in Table 5.5. Obviously, the initial solar phase required by the quasi sun-synchronous solution is chosen from the near-zero region of Figure 5.17. In Table 5.5 it is self-evident the effectiveness of the strategy proposed. Specifically, the solution presented is based on $\theta_{sun} = 36.01613°$. Exploiting this case, it is worth to depict in Figure 5.18 the difference between the solar and the vehicle angular position along the orbit, in order to offer a further insight of a quasi sun-synchronous Lyapunov orbit. It should be observed that even if the trend of $\Delta\theta = \theta_{sc} - \theta_{sun}$ is not constant during the orbit, it is limited and eventually returns to its initial value (within a small tolerance); also, the fashions corresponding to the upper and the lower arc of orbit are specular.

Table 5.5: Comparison between crossing errors.

	Small	**Medium**	**Large**	**Sun-Syn.**
ϵ_x [m]	1287732.10	804863.52	-198780.17	-116.62
ϵ_{vx} [m/s]	10.09	5.68	-1.27	-0.44
ϵ_{vy} [m/s]	-3.59	-2.05	0.84	-0.07
$\epsilon_{\theta_{sun}}$ [deg]	149.213	170.332	89.800	0.070

The solar phase angle $\theta_{sun} \approx 36°$, that guarantees a drop in the crossing errors on a quasi Sun-synchronous Lyapunov periodic orbit, has been discovered considering a precise vehicle configuration: the V-SS, see data

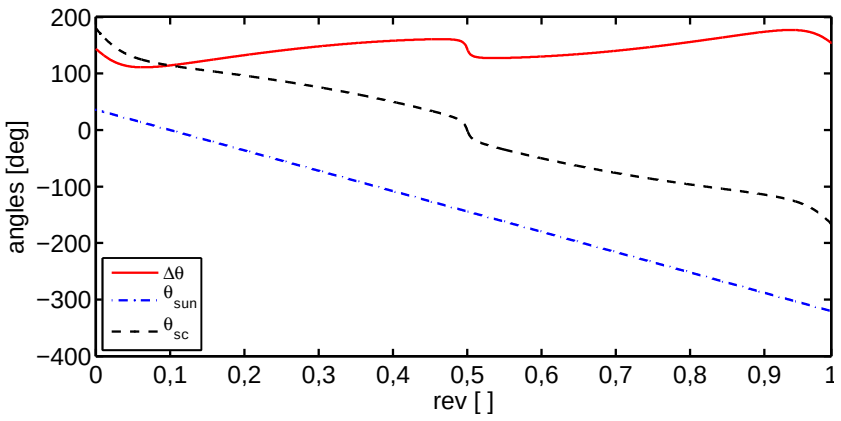

Figure 5.18: Difference between the Sun and spacecraft angular positions along a quasi sun-synchronous Lyapunov periodic orbit.

in Table 5.6. The scope of the following research is to prove the effectiveness of such mission design for a wide range of architectures. Meanwhile, the limits of this strategy will be drawn. To this end, four parameters are identified changing the dynamical response:

- The ratio of the total effective area and the total spacecraft mass A/m. This parameter controls the ratio of the solar radiation pressure over the inertia forces.
- The ratio Ab/I, where b is the distance between the spacecraft center of mass and the center of pressure of the exposed surfaces above the axis of symmetry, I is the moment of inertia about the pitch axis. This parameter controls the ratio of moments due to the solar radiation pressure and the inertia of the system.
- The solar arrays inclination δ_{sa}. This parameter affects the stability of the attitude around the equilibrium position.
- The moments of inertia ratio k_3. This parameter affects the gravity gradient torque and its disturbing impact.

Table 5.6: VSS characteristic data.

A/m [m^2/kg]	Ab/I [m/kg]	δ_{sa} [deg]	k_3
0.0228	0.0114	45	0

The first analysis evaluates the crossing errors for noteworthy variation of the parameter A/m, assuming the set of values $A/m\,[\mathrm{m}^2/\mathrm{kg}] =$

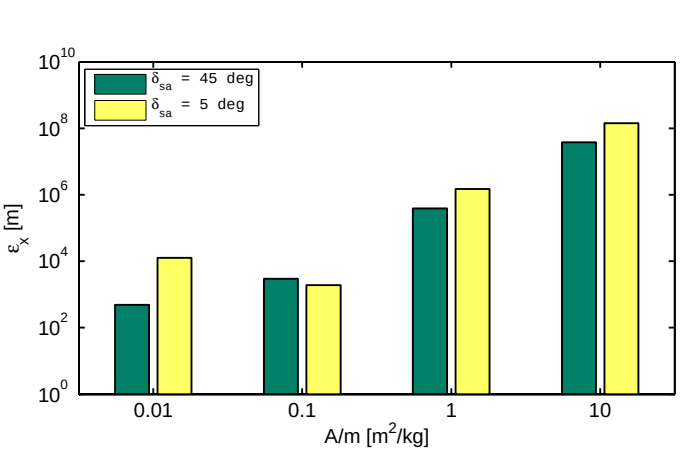

(a) Position error.

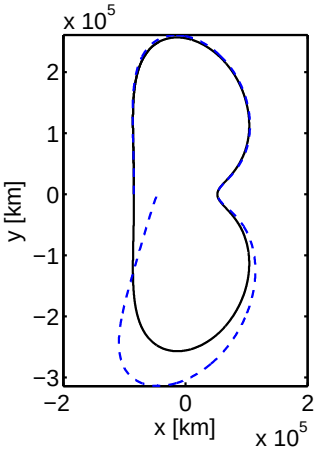

(b) Configuration space (ℓ-frame) for $A/m = 10$ m^2/kg - $\delta_{sa} = 45°$.

Figure 5.19: Sensitivity to the parameter A/m - 1.

$\{0.01,\ 0.1,\ 1,\ 10\}$. To start with, Figure 5.19-(a) shows that acceptable position errors are obtained for an order of magnitude of A/m up to $O(10^{-1})$ m^2/kg. On the contrary, for values well above the unity (*i.e.* $A/m = 10$ m^2/kg) the force exerted by the solar radiation pressure is likely comparable, or even overcomes, the translational inertia forces and the orbital motion is seriously altered, as visible in 5.19-(b). A clearer trend appears for the velocity and Sun phase errors in Figure 5.20: they both increase monotonically with the ratio A/m. Figure 5.20 confirms again that, up to the order $O(10^{-1})$ m^2/kg (which includes standard satellites or space stations), the vehicle experiences incredibly small errors of the crossing condition. The attitude motion is affected by A/m as well. In all the case addressed the motion remains oscillatory around the nominal pointing condition $\alpha_b = 0°$, but the amplitude of librations may rise quickly with A/m for configurations equipped with highly inclined solar arrays, see Table 5.7.

The second analysis investigates how the inclination angle of the solar arrays acts on the success of the strategy. Basically, Figures 5.21 and 5.22 demonstrate that for any axisymmetric distribution of mass (*i.e.* $k_3 = 0$) the only value of $\delta_{sa} \in [0°, 45°]$ leading to critical crossing errors is $\delta_{sa} = 0°$, which means no passive control on the pointing orientation. The efficacy may turn out to be weakened for low solar arrays inclinations if the spacecraft is not inertially axisymmetric; however, the same performances will likely be recovered increasing another parameter Ab/I, discussed in the

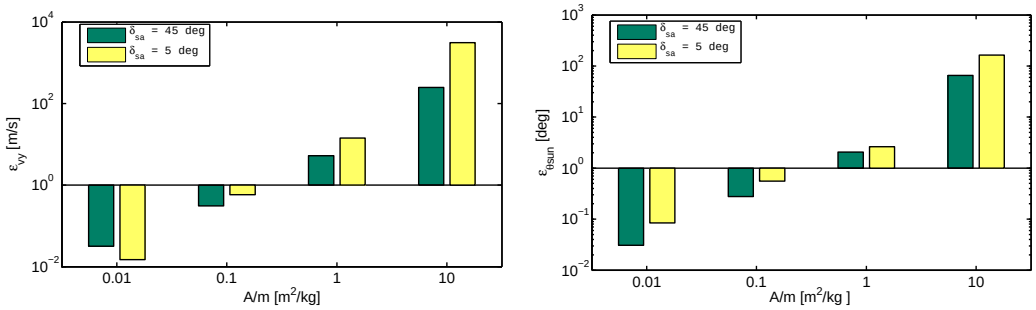

(a) Velocity errors.

(b) Solar phase error.

Figure 5.20: Sensitivity to the parameter A/m - 2.

Table 5.7: Maximum oscillation amplitude in function of A/m

A/m $[m^2/kg]$	**Maximum amplitude [deg]**	
	$\delta_{sa} = 45°$	$\delta_{sa} = 5°$
0.01	4.49	8.78
0.1	11.10	0.90
1	25.22	3.36
10	78.97	2.23

next paragraph. The results for δ_{sa} also highlight that the coupling between the attitude and the orbital dynamics cannot be neglected. In fact, as long as the desired spacecraft orientation is lost, also the orbital trajectory drifts from the designed path.

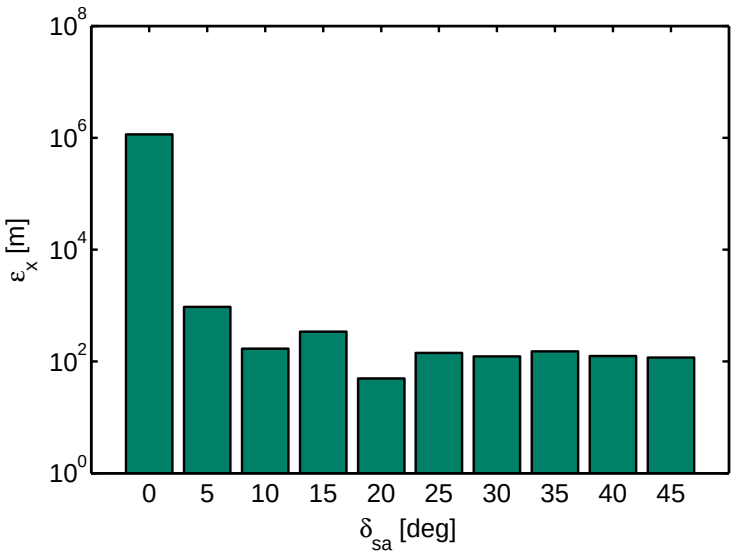

Figure 5.21: Sensitivity of the position error to the arrays inclination δ_{sa}.

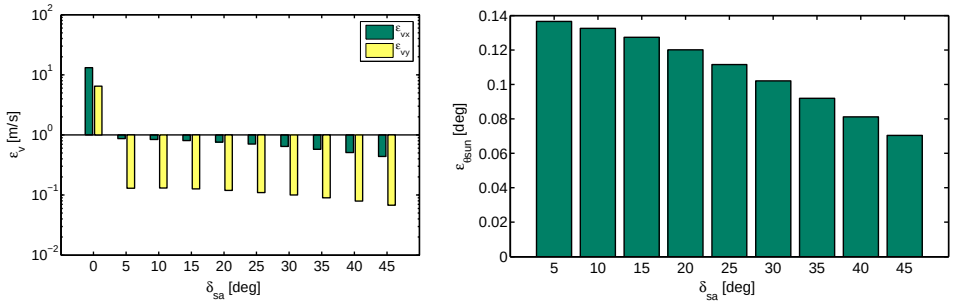

(a) Velocity errors. (b) Solar phase error.

Figure 5.22: Sensitivity of other errors to the arrays inclination δ_{sa}.

The last study aims at providing a deeper insight on the parameter Ab/I. Since this ratio controls the moment provoked by the solar pressure, or rather the moment responsible for rejecting disturbance on the pointing condition, it is worth to include in this analysis also the last parameter k_3, which affects instead the perturbation due to the gravity gradient torque. The simulations are performed for $Ab/I\,[\text{m/kg}] = \{0.01,\, 0.001,\, 0.0001\}$ and $k_3 \in [0, 1]$. As in the study of A/m, the focus is on variation of the order of magnitude of the parameter. At a first glance of the velocity crossing errors in Figure 5.23, it seems that not significant alterations of the dynamics exist. In fact, Figure 5.23 reports extremely low errors of both the velocity components ($\dot{\epsilon}_x < 0.2$ m/s, $\dot{\epsilon}_y < 0.07$ m/s) for any combination of Ab/I and k_3. From that, it can be inferred the robustness of the

orbital solution against variation of the parameters considered. On the other hand, the attitude response should be examined as well. Figure 5.24 points out the different sensitivity of the orbital and attitude motion to Ab/I and k_3 in terms Sun phase and aiming respectively. Figure 5.24-(a) shows the attitude angle relative to the Sun spacecraft-line at the crossing instant. The large values noticeable in the chart indicate that the spacecraft started to spin and rotations accumulate throughout the motion; hence, the space structure is not rotationally stable around the equilibrium condition $\alpha_b = 0°$ because of the gravity gradient torque. In fact, the mentioned cases correspond to high anisotropic distributions of mass ($k_3 \rightarrow 1$) and low values of Ab/I. Surprisingly, a divergence of the attitude motion does not correspond to a divergence of the orbital motion. Not trivially, when the spacecraft reaches a certain spin rate, the attitude dynamics becomes much faster than the orbital response. As consequence, the force exerted by the solar pressure that really affects the orbital motion is equivalent to the mean value over a certain number of spacecraft's revolutions. Eventually, the direction of the mean force is very likely to match the sun-spacecraft line, since all the transversal components tend to annihilate each other; the condition assumed to deliver the nominal solution is indeed satisfied within a reasonable tolerance.

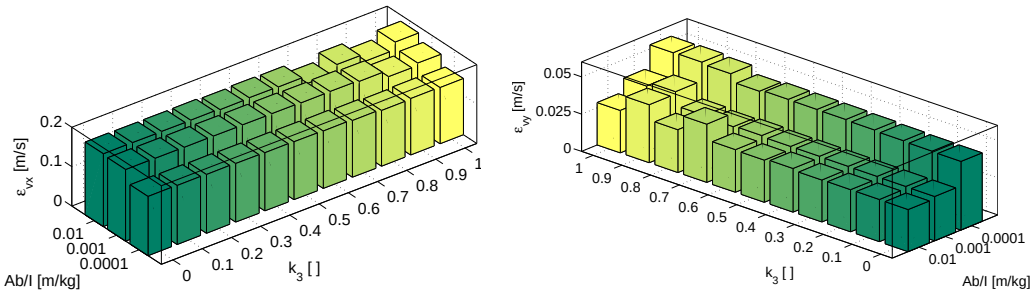

Figure 5.23: Sensitivity of the velocity errors to the parameters Ab/I and k_3.

The best insight on both orbital and attitude maintenance is probably offered by the chart of the position error in Figure 5.25. The overall trend is quite obvious: the best condition is given by the maximum value of Ab/I and $k_3 = 0$; on the contrary, the worst case is given by the minimum value of Ab/I and $k_3 = 1$. These circumstances simply represent the maximum control action coupled to the minimal disturbance and vice-versa. However, some information is hidden behind the general apparency. Despite,

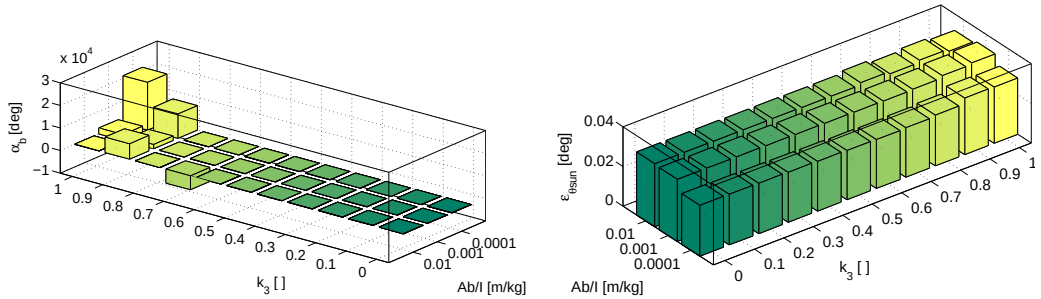

(a) Pointing angle. (b) Solar phase error.

Figure 5.24: Sensitivity of other errors to the parameters Ab/I and k_3.

as already discussed, there are not critical errors, slight discrepancies in the magnitude are sufficient to predict variations of the attitude response nature. Letters in the plot recall different attitude responses depicted in Figure 5.26. The lowest ϵ_x corresponds to the spacecraft oscillating around the equilibrium orientation $\alpha_b = 0°$ (see 5.26-(a)); conversely, the greatest ϵ_x relates to a quick divergence of α_b (see 5.26-(d)). An interesting attitude behavior emerges for $A/m = 0.01$ m^2/kg and the interval of inertia ratio $k_3 \in [0.7, 0.9]$: as shown in Figure 5.26-(b), for $k_3 = 0.7$ the spacecraft spins clockwise; for $k_3 = 0.8$ the spacecraft oscillates around $\alpha_b = 0°$; for $k_3 = 0.9$ the spacecraft spins counterclockwise. A similar bifurcation of the response nature can be noticed in Figure 5.26-(c) for $A/m = 0.001$ m^2/kg ; this time, only one turning point occurs for k_3 increasing from 0.8 to 1. The phenomenon has not been fully understood yet, so further research is required to provide a proper explanation.

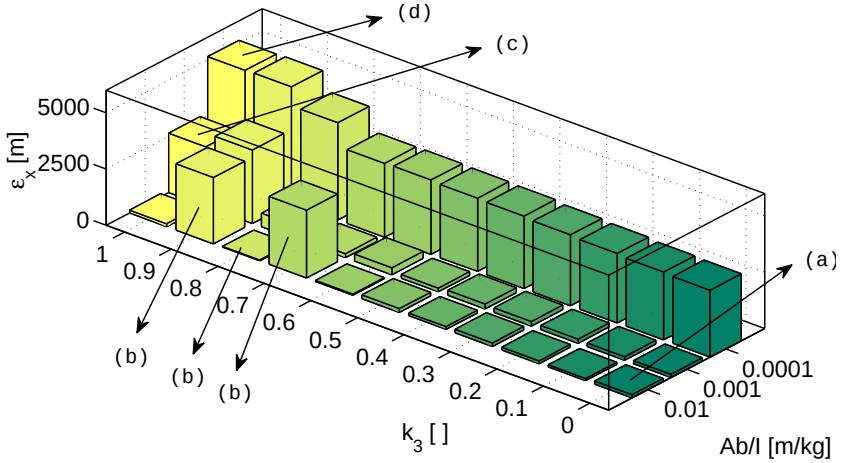

Figure 5.25: Sensitiviy of the position error to the parameters Ab/I and k_3.

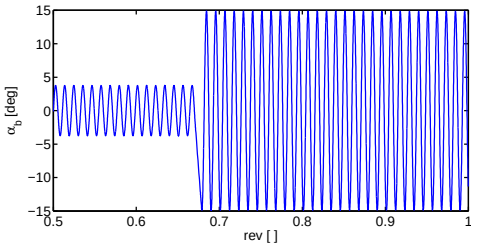

(a) $Ab/I = 0.01\,\mathrm{m/kg}\,, k_3 = 0.$

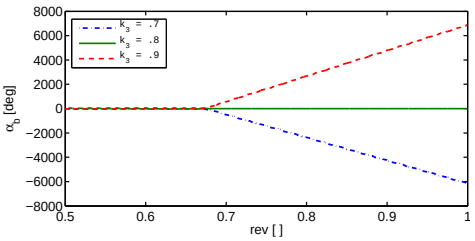

(b) $Ab/I = 0.01\,\mathrm{m/kg}\,, k_3 = 0.7, 0.8, 0.9.$

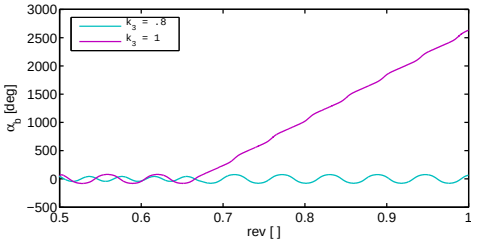

(c) $Ab/I = 0.001\,\mathrm{m/kg}\,, k_3 = 0.8, 1.$

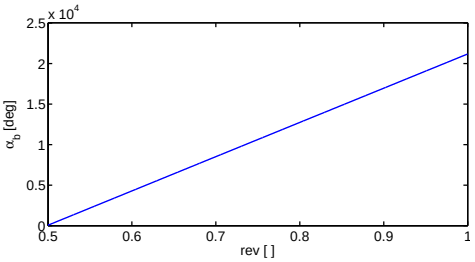

(d) $Ab/I = 0.0001\,\mathrm{m/kg}\,, k_3 = 1.$

Figure 5.26: Pointing angle history.

6 Formulation Including Flexibility

Contents

Chapter 3 has presented the formulation adopted to reproduce the planar dynamics of large rigid space structures in the vicinity of the libration points. In this Chapter the hypothesis of rigid body is dropped and the structure deformation is included in the system dynamics. In the first Section, the elastic discretization of the problem via modal shapes is described. Secondly, the kinematics necessary to introduce the elastic displacements is developed. Finally, the equations of motion incorporating the spacecraft flexibility are derived in the Euler-Lagrange form and are successively manipulated accordingly to the Encke's Method.

6.1 Elastic Discretization

When the structure becomes flexible, any infinitesimal mass point does not retain a fixed location in the local coordinate system (the b-frame) anymore. It shall be accounted the chance of a further relative displacement because of the body deformation. Thus, the position vector of an infinitesimal mass in the point P, as shown in Figure 6.1, consists of two contribu-

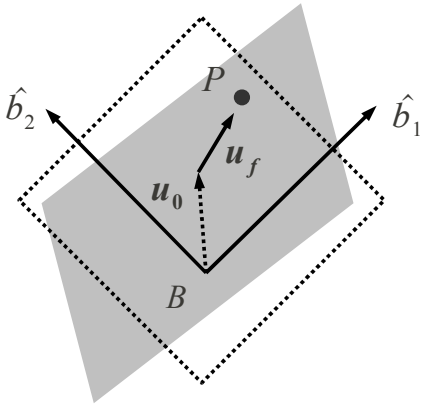

Figure 6.1: Local position vector on the deformed body.

tions

$$\boldsymbol{u} = \boldsymbol{u}_0 + \boldsymbol{u}_f \quad , \tag{6.1}$$

where $\boldsymbol{u}_0$ is the undeformed position and $\boldsymbol{u}_f$ is the elastic displacement; both vectors are written on the basis of the b-frame. Recalling the discussion in Chapter 2, the elastic dynamics of the spacecraft shall be approximated by a finite number of elastic variables. Therefore, the shape functions $[S]$ are introduced to express the elastic displacements $\boldsymbol{u}_f$ as a linear composition of known spatial functions

$$\boldsymbol{u}_f = [S]\boldsymbol{q}_f \quad , \tag{6.2}$$

where $\boldsymbol{q}_f$ is the weights vector. This representation also separates the spatial and the temporal variables of the problem and assumes *a-priori* the spatial solution through the shape functions $[S]$. Thus, $\boldsymbol{q}_f$ represents the actual elastic generalized coordinates of the dynamics, that join those employed in Chapter 3 to describe the rigid motion

$$\boldsymbol{q}_r = [\boldsymbol{R}^T \quad \phi]^T \quad , \tag{6.3}$$

where $\boldsymbol{R}$ is the position vector of the b-frame origin relative to the Lagrangian point and ϕ denotes the orientation of the former coordinates system with respect to the ℓ-frame. Hence, substituting eq. (6.2) into eq. 6.4, the overall location of P in the b-frame is given by

$$\boldsymbol{u} = \boldsymbol{u}_0 + \boldsymbol{u}_f = \boldsymbol{u}_0 + [S]\boldsymbol{q}_f \quad . \tag{6.4}$$

As mentioned in Chapter 3, the shape functions are arbitrary with the only requirement of being admissible. However, arbitrary choices also may lead to extremely poor accuracy, especially when the selected shapes are not an adequate representation of the body deformation. In this work the dynamics addressed is natural under a multi-body gravitational field. In particular, neither external concentrate loads or actions are introduced. The focus is on natural global shape changes rather than on induced local deformations. Likewise, the spacecraft is assumed being in its operative configuration, so the deployment phase, that may be necessary for a large space structure, is not presently considered. Give that, it seems reasonable adopting the assumptions of the linear elastic theory and consequently employing the normal modes of the structure as shape functions. The reasons to adopt the modal forms are several:

- Modes automatically satisfy the essential conditions.
- A proper selection of modes usually guarantees a prediction of the natural response more accurate than any other arbitrary set of functions, given the same number of elastic degrees of freedom.
- Modes are orthogonal with respect to the mass and the stiffness matrix.
- They are a representation suitable for the floating frame, as the relative displacements can be expressed referring to a single coordinate system.
- Modes can be numerically computed for any arbitrary spacecraft using a finite element model.

For the concern of this study, the modal formulation can be divided into two classes: the free-modes and the constrained-modes. The free-modes denote a modal representation of the deformed geometry where no points of the structure, observed from the b-frame, are necessary fixed. On this basis, the free-modes are able to guarantee no relative shift of the center of mass. It follows that, the three dynamics (orbital, attitude, elastic) can be inertially decoupled by placing the origin of the floating frame (*i.e.* the b-frame) in the configuration center of mass. This means that the mass matrix is diagonal, but the overall system is still fully coupled by the gravity gradient. Nonetheless, a diagonal mass matrix critically reduces the computation effort. In the current work only the free-modes will be adopted, but in further developments may be convenient to shift to the constrained counterpart. Constrained-modes are the solution of the natural elastic dynamics

obtained by imposing the displacement (usually null) of some parts of the structure. This is particularly useful to describe joints, multi-body architectures and local deformations. Despite that, the constrained-modes are not able to decouple the elastic dynamics from the rigid motions, roughly because the center of mass cannot be represented as a fixed point in the floating frame. Therefore, the numerical solution of the equations of motion might turn out to be challenging. Optionally, the floating frame can be redefined according to the mean-axis condition, which is based on the minimization of the deformation kinetic energy and leads to a weakly-coupled formulation. An insightful explanation of the mean-axes as floating frame as well as a clear comparison between free and constrained modes is delivered by Nikravesh in [68]. Besides the benefits of the modal formulation, there are drawbacks too. The major limit is the assumption of linear behavior; this implies that the method is inapplicable in circumstances which require large deformations (*e.g.* the deployment of elements of the spacecraft). The geometrically exact representation of shape change requires other approaches to the problem, such as those developed by Shabana et al. [83] or by Vu-Quoc and Simo [33]. Secondly, a relatively large number of elastic modes may be needed to accurately predict the vehicle's high flexibility.

6.2 Kinematics

The reader is strongly invited to refer to the rigid formulation developed in Chapter 3 and the attendant discussions before proceeding through the next two Sections; the general framework is the same of the preceding Chapter and, for sake of brevity, definitions and considerations already mentioned will be omitted in the followings. Conversely, the arrangements necessary to incorporate the structure flexibility in the model delivered in Chapter 3 will be highlighted.

To begin with, the local position $\boldsymbol{u}$ of an infinitesimal mass dm in the point P considers also the contribution of the elastic displacement as formulated in eq. (6.4); thus, the global position vector expressed in the ℓ-frame becomes

$$\boldsymbol{r}_P = \boldsymbol{R} + [A]\boldsymbol{u} = \boldsymbol{R} + [A](\boldsymbol{u}_0 + [S]\boldsymbol{q}_f) \quad . \tag{6.5}$$

In turn, the temporal derivative of the position vector shall consider variations of the elastic generalized coordinates $\boldsymbol{q}_f$ that describe the deformed

geometry, so

$$\dot{\boldsymbol{r}}_P = \dot{\boldsymbol{R}} + [\dot{A}]\boldsymbol{u} + [A][S]\dot{\boldsymbol{q}}_f \quad . \tag{6.6}$$

Straightforwardly, also the set of generalized coordinates is redefined to incorporate the new variables $\boldsymbol{q}_f$ as

$$\boldsymbol{q} = \begin{bmatrix} \boldsymbol{q}_r \\ \boldsymbol{q}_f \end{bmatrix} = \begin{bmatrix} \boldsymbol{R} \\ \phi \\ \boldsymbol{q}_f \end{bmatrix} \quad . \tag{6.7}$$

In Chapter 3 was anticipated that certain integrals function of the distribution of mass are a constant parameter of the motion. Given the separation of variables due to the elastic discretization, the spatial component of the elastic solution is known *a-priori*. Thus, even if the mass distribution changes in function of the elastic generalized coordinates $\boldsymbol{q}_f$, the spatial integrals can be computed in advance. The only assumption, in accordance with the linear elastic theory, is to considered the volume of integration undeformed. The possibility to solve all the integrals appearing in the equations of motion is fundamental, because integro-differential equations are transformed in a set of ordinary differential equations. Shabana [67] named the aforementioned quantities Inertia Shape Integrals. For the flexible formulation new inertia shape integrals have to be defined: firstly those that describe the inertial coupling between rigid and elastic dynamics

$$[\bar{S}] = \int_V \rho[S]dV \quad , \tag{6.8}$$

$$[I_{0f}] = \int_V \rho \boldsymbol{u}_0^T[S]dV \quad , \tag{6.9}$$

and

$$[I_0] = \int_V \rho[S]^T \boldsymbol{u}_0 dV \quad , \tag{6.10}$$

which are all equal to zero when the local frame is in the center of mass and $[S]$ are derived from the free-modes; then, those used to represent the variation of the mass matrix

$$[m_{ff}] = \int_V \rho[S]^T[S]dV \quad , \tag{6.11}$$

$$[\tilde{S}] = \int_V \rho[S]^T[\tilde{I}][S]dV \quad , \tag{6.12}$$

with

$$[\tilde{I}] = \begin{bmatrix} 0 & 1 \\ -1 & 0 \end{bmatrix} \quad , \tag{6.13}$$

and

$$[\tilde{S}_0] = \int_V \rho \boldsymbol{u}_0^T [\tilde{I}][S] dV \quad . \tag{6.14}$$

If $[S]$ is computed on the modal basis, eq. (6.11) is equivalent to the matrix of the modal masses of the deformable system.

6.3 Dynamics

In the analogous Section of Chapter 3 the fully-coupled equations of motion for a spacecraft orbiting in the vicinity of the libration points are delivered via the Lagrangian procedure. Here, all the energies have to be rewritten to account the body deformation and consequently new terms add to the equations of motion.

The gravitational potential is rearranged to incorporate the geometry changes of the spacecraft as well

$$\begin{aligned} U_x(\boldsymbol{R}_x) \;=\; & -\mu_x \left[\frac{m}{|\boldsymbol{R}_x|} - \frac{1}{|\boldsymbol{R}_x|^2} \boldsymbol{l}_x^T ([I_1] + [\tilde{S}]\boldsymbol{q}_f) \right. \\ & -\frac{1}{2}\frac{1}{|\boldsymbol{R}_x|^3}(I_{00} + 2[I_{0f}]\boldsymbol{q}_f + \boldsymbol{q}_f^T [m_{ff}]\boldsymbol{q}_f) \\ & \left. +\frac{3}{2}\frac{1}{|\boldsymbol{R}_x|^3} \boldsymbol{l}_x^T \left([JJ_{00}] + \sum_i^{n_e} ([JJ_{0i}] + [JJ_{i0}]) q_i + \sum_i^{n_e}\sum_j^{n_e} [JJ_{ij}] q_i q_j \right) \boldsymbol{l}_x \right] \end{aligned} \tag{6.15}$$

where $q_{i/j}$ stand for the ith/jth components of the vector $\boldsymbol{q}_f$, n_e is the number of elastic degrees of freedom and three new inertia shape integrals are defined as

$$[JJ_{0i}] = \int_V \rho \boldsymbol{u}_0 \boldsymbol{S}_i^T \, dV \quad , \tag{6.16}$$

$$[JJ_{i0}] = \int_V \rho \boldsymbol{S}_i \boldsymbol{u}_0^T \, dV \quad , \tag{6.17}$$

$$[JJ_{ij}] = \int_V \rho \boldsymbol{S}_i \boldsymbol{S}_j^T \, dV \quad . \tag{6.18}$$

Similarly, the elastic displacements contribute toward the fictitious potential due to the centrifugal force

$$\begin{aligned} T_1 &= \frac{1}{2}m\boldsymbol{v}(O')^T\boldsymbol{v}(O') + m\boldsymbol{v}(O')^T[\tilde{\omega}]\boldsymbol{R} + \boldsymbol{v}(O')^T[\tilde{\omega}][A](I_1 + [\bar{S}]\boldsymbol{q}_f) \\ &+\frac{1}{2}\Omega^2 m\boldsymbol{R} + \Omega^2\boldsymbol{R}^T[A](I_1 + [\bar{S}]\boldsymbol{q}_f) \\ &+\frac{1}{2}\Omega^2(I_{00} + 2[I_{of}]\boldsymbol{q}_f + \boldsymbol{q}_f^T[m_{ff}]\boldsymbol{q}_f) \end{aligned} \tag{6.19}$$

and due to the Coriolis force

$$\begin{aligned} T_2 &= m\dot{\boldsymbol{R}}^T\boldsymbol{v}(O') + m\dot{\boldsymbol{R}}^T[\tilde{\omega}]\dot{\boldsymbol{R}} + \dot{\boldsymbol{R}}^T[\tilde{\omega}][A](I_1 + [\bar{S}]\boldsymbol{q}_f) \\ &+(I_1 + [\bar{S}]\boldsymbol{q}_f)^T[\dot{A}]^T(\boldsymbol{v}(O') + [\tilde{\omega}]\boldsymbol{R}) + \Omega\dot{\phi}(I_{00} + 2[I_{of}]\boldsymbol{q}_f + \boldsymbol{q}_f^T[m_{ff}]\boldsymbol{q}_f) \\ &+\dot{\boldsymbol{q}}_f^T[\bar{S}]^T[A]^T(\boldsymbol{v}(O') + [\tilde{\omega}]\boldsymbol{R}) + \Omega([\tilde{S}_0] + \boldsymbol{q}_f^T[\tilde{S}])\dot{\boldsymbol{q}}_f \quad . \end{aligned} \tag{6.20}$$

Also the relative kinematic energy with respect to an observer on the ℓ-frame should be recomputed, however it can be easily derived from the definition given in eq. (3.15) adopting the augmented version of the generalized coordinates in eq. (6.7) and the mass matrix reported later in this Section.

Additionally, the deformation energy shall be included in the Lagrangian function eq. (3.7). It appears as

$$U_f = \frac{1}{2}\int_V \boldsymbol{\sigma}^T\boldsymbol{\varepsilon}dV \quad , \tag{6.21}$$

where $\boldsymbol{\varepsilon}$ are the structural strain defined via the matrix differential operator $[D]$ as

$$\boldsymbol{\varepsilon} = [D]\boldsymbol{u}_f = [D][S]\boldsymbol{q}_f \quad . \tag{6.22}$$

The structural stress $\boldsymbol{\sigma}$ are written in function of the elastic coordinates too, assuming a linear-elastic costitutive relation

$$\boldsymbol{\sigma} = [E]\boldsymbol{\varepsilon} = [E][D][S]\boldsymbol{q}_f \quad , \tag{6.23}$$

where $[E]$ is the stiffness tensor. Substituting eq. (6.22) and eq. (6.23) into eq. (6.21), it yields to

$$U_f = \frac{1}{2}\int_V \boldsymbol{q}_f^T([D][S])^T[E][D][S]\boldsymbol{q}_f dV \quad . \tag{6.24}$$

The former equation is rearranged as

$$U_f = \frac{1}{2}\boldsymbol{q}_f^T[K_{ff}]\boldsymbol{q}_f \tag{6.25}$$

in order to make esplicit the elastic stiffness matrix

$$[K_{ff}] = \int_V ([D][S])^T [E][D][S] dV \quad , \tag{6.26}$$

which can actually be considered a inertial shape integral in a broad sense, since it is an integral that can be computed in advance of the system solution.

Once the Lagrangian function is known for the deformable system too, the equations of motion can be obtained in the Euler-Lagrange form as in Chapter 3. For convenience, they are presented in matrix fashion

$$[M]\ddot{\boldsymbol{q}} + [K]\boldsymbol{q} = \boldsymbol{Q}_\nu + \boldsymbol{Q}_g + \boldsymbol{Q}_\Omega \quad , \tag{6.27}$$

where the mass matrix is augmented

$$[M] = \begin{bmatrix} m_{RR} & m_{R\phi} & m_{Rf} \\ & m_{\phi\phi} & m_{\phi f} \\ \text{symmetric} & & m_{ff} \end{bmatrix} \tag{6.28}$$

including new terms

$$\begin{aligned} m_{\phi\phi} &= [I_{00}] + 2[I_{0f}]\boldsymbol{q}_f + \boldsymbol{q}_f^T [m_{ff}]\boldsymbol{q}_f \quad , \\ m_{R\phi} &= [A]_{/\phi}([I_1] + [\bar{S}]\boldsymbol{q}_f) \quad , \\ m_{Rf} &= [A][\bar{S}] \quad , \\ m_{\phi f} &= [\tilde{S}_0] + \boldsymbol{q}_f^T [\tilde{S}] \quad , \end{aligned}$$

and system stiffness matrix is given by

$$[K] = \begin{bmatrix} 0 & 0 & 0 \\ 0 & 0 & 0 \\ 0 & 0 & [K_{ff}] \end{bmatrix} \quad . \tag{6.29}$$

Also the right-hand terms of eq. (6.27) are defined consistently with the introduction of the elastic variables $\boldsymbol{q}_f$

$$\boldsymbol{Q}_\nu = \begin{bmatrix} (Q_\nu)_R \\ (Q_\nu)_\phi \\ (Q_\nu)_f \end{bmatrix} = [M]\ddot{\boldsymbol{q}} - \frac{d}{dt}\left(\frac{\partial T_{rel}}{\partial \dot{\boldsymbol{q}}}\right) + \frac{\partial T_{rel}}{\partial \boldsymbol{q}} \quad , \tag{6.30}$$

$$\boldsymbol{Q}_g = \begin{bmatrix} (Q_g)_R \\ (Q_g)_\phi \\ (Q_g)_f \end{bmatrix} = -\frac{\partial U}{\partial \boldsymbol{q}} \quad , \tag{6.31}$$

$$\boldsymbol{Q}_\Omega = \begin{bmatrix}(Q_\Omega)_R\\(Q_\Omega)_\phi\\(Q_\Omega)_f\end{bmatrix} = +\frac{\partial T_1}{\partial \boldsymbol{q}} + \frac{\partial T_2}{\partial \boldsymbol{q}} - \frac{d}{dt}\left(\frac{\partial T_2}{\partial \dot{\boldsymbol{q}}}\right) \quad . \tag{6.32}$$

The notation $(V)\bullet$ simply stands for the components of $\boldsymbol{V}$ related to the equations describing the dynamics $\bullet$, where $\bullet = R$ denotes the orbital motion, $\bullet = \phi$ the attitude motion and $\bullet = f$ the elastic motion.

This last paragraph provides detailed developments of the equations of motion (6.27). Each dynamics is presented separately. Firstly, the Encke's method is recalled from Chapter 3 to formulate the orbital motion in terms of drift $\boldsymbol{\delta}$ from a reference trajectory

$$[m_{RR}]\ddot{\boldsymbol{\delta}} + [m_{R\phi}]\ddot{\phi} + [m_{Rf}]\ddot{\boldsymbol{q}} = (\boldsymbol{\delta Q}_\nu)_R + (\boldsymbol{\delta Q}_g)_R + (\boldsymbol{\delta Q}_\Omega)_R \quad . \tag{6.33}$$

Terms in the preceding equation have the following expressions:

$$(\delta Q_\nu)_R = \dot{\phi}^2[A]([\bar{S}]\boldsymbol{q}_f + [I_1]) - 2\dot{\phi}[A]_{/\phi}[\bar{S}]\dot{\boldsymbol{q}}_f \quad ; \tag{6.34}$$

$$(\delta Q_g)_R = -\left(\frac{\partial U_1}{\partial \boldsymbol{R}} - \frac{\partial U_1^0}{\partial \boldsymbol{R_0}}\right) - \left(\frac{\partial U_2}{\partial \boldsymbol{R}} - \frac{\partial U_2^0}{\partial \boldsymbol{R_0}}\right) \quad , \tag{6.35}$$

where

$$\left(\frac{\partial U_x}{\partial \boldsymbol{R}} - \frac{\partial U_x^0}{\partial \boldsymbol{R_0}}\right) = \mu_x \frac{m}{|\boldsymbol{R}_x^0|^3}(\boldsymbol{\delta} + f(h)\boldsymbol{R}_x) + \boldsymbol{a}_P^x \quad , \tag{6.36}$$

with

$$f(h) = h\frac{3 + 3h + h^2}{1 + (1+h)^{3/2}} \quad , \tag{6.37}$$

$$h = \frac{\boldsymbol{\delta}^T\boldsymbol{\delta} - 2\boldsymbol{\delta}^T\boldsymbol{R}_x}{|\boldsymbol{R}_x|^2} \quad , \tag{6.38}$$

and

$$\begin{aligned}
\boldsymbol{a}_P^x \;=\; & -\mu_x\left[\frac{2}{|\boldsymbol{R}_x|^3}\frac{\partial|\boldsymbol{R}_x|}{\partial \boldsymbol{R}}\boldsymbol{l}_x^T([I_1] + [\bar{S}]\boldsymbol{q}_f)\right. \\
& -\frac{1}{|\boldsymbol{R}_x|^2}\left(\frac{\partial \boldsymbol{l}_x}{\partial \boldsymbol{R}}\right)^T([I_1] + [\bar{S}]\boldsymbol{q}_f) \\
& +\frac{3}{2}\frac{1}{|\boldsymbol{R}_x|^4}\frac{\partial|\boldsymbol{R}_x|}{\partial \boldsymbol{R}}(I_{00} + 2[I_{of}]\boldsymbol{q}_f + \boldsymbol{q}_f^T[m_{ff}]\boldsymbol{q}_f) \\
& -\frac{9}{2}\frac{1}{|\boldsymbol{R}_x|^4}\frac{\partial|\boldsymbol{R}_x|}{\partial \boldsymbol{R}}\boldsymbol{l}_x^T\left([JJ_{00}] + \sum_i^{n_e}([JJ_{0i}] + [JJ_{i0}])q_i + \sum_i^{n_e}\sum_j^{n_e}[JJ_{ij}]q_iq_j\right)\boldsymbol{l}_x \\
& \left.+3\frac{1}{|\boldsymbol{R}_x|^3}\boldsymbol{l}_x^T\left([JJ_{00}] + \sum_i^{n_e}([JJ_{0i}] + [JJ_{i0}])q_i + \sum_i^{n_e}\sum_j^{n_e}[JJ_{ij}]q_iq_j\right)\frac{\partial \boldsymbol{l}_x}{\partial \boldsymbol{R}}\right] \quad ;
\end{aligned} \tag{6.39}$$

$$(\delta Q_\Omega)_R = \left(\frac{\partial T_1}{\partial \boldsymbol{R}} - \frac{\partial T_1^0}{\partial \boldsymbol{R_0}}\right) + \left(\frac{\partial T_2}{\partial \boldsymbol{R}} - \frac{\partial T_2^0}{\partial \boldsymbol{R_0}}\right) - \left(\frac{d}{dt}\left(\frac{\partial T_2}{\partial \dot{\boldsymbol{R}}}\right) - \frac{d}{dt}\left(\frac{\partial T_2^0}{\partial \dot{\boldsymbol{R}}_{\boldsymbol{0}}}\right)\right) \quad , \tag{6.40}$$

where

$$\left(\frac{\partial T_1}{\partial \boldsymbol{R}} - \frac{\partial T_1^0}{\partial \boldsymbol{R_0}}\right) = \Omega^2[A]([I_1] + [\bar{S}]\boldsymbol{q_f}) + \Omega^2 m\boldsymbol{\delta} \quad , \tag{6.41}$$

$$\left(\frac{\partial T_2}{\partial \boldsymbol{R}} - \frac{\partial T_2^0}{\partial \boldsymbol{R_0}}\right) = m[\tilde{\omega}]^T\dot{\boldsymbol{\delta}} + [\tilde{\omega}]^T[A][\bar{S}]\dot{\boldsymbol{q}}_{\boldsymbol{f}} + [\tilde{\omega}]^T[\dot{A}]([I_1] + [\bar{S}]\boldsymbol{q_f}) \tag{6.42}$$

and

$$\frac{d}{dt}\left(\frac{\partial T_2}{\partial \dot{\boldsymbol{R}}}\right) - \frac{d}{dt}\left(\frac{\partial T_2^0}{\partial \dot{\boldsymbol{R}}_{\boldsymbol{0}}}\right) = m[\tilde{\omega}]\dot{\boldsymbol{\delta}} + [\tilde{\omega}][A][\bar{S}]\dot{\boldsymbol{q}}_{\boldsymbol{f}} + [\tilde{\omega}][\dot{A}]([I_1] + [\bar{S}]\boldsymbol{q_f}) \quad . \tag{6.43}$$

The equations describing the attitude dynamics are simply extracted from the system (6.27)

$$[m_{R\phi}]^T\ddot{\boldsymbol{R}} + [m_{\phi\phi}]\ddot{\phi} + [m_{\phi f}]\ddot{\boldsymbol{q}} = (\boldsymbol{Q}_\nu)_\phi + (\boldsymbol{Q}_g)_\phi + (\boldsymbol{Q}_\Omega)_\phi \tag{6.44}$$

and the various right-hand active components are made explicit:

$$(Q_\nu)_\phi = -2\dot{\phi}\boldsymbol{q_f}^T([m_{ff}]\boldsymbol{q_f} + [I_0]) \quad ; \tag{6.45}$$

$$(Q_g)_\phi = -\frac{\partial U_1}{\partial \phi} - \frac{\partial U_2}{\partial \phi} \quad , \tag{6.46}$$

where

$$\frac{\partial U_x}{\partial \phi} = -\mu_x\left[-\frac{1}{|\boldsymbol{R_1}|^2}\left(\frac{\partial \boldsymbol{l_x}}{\partial \phi}\right)([I_1] + [\bar{S}]\boldsymbol{q_f}) + \frac{3}{|\boldsymbol{R_x}|^3}\boldsymbol{l_x}^T\left([JJ_{00}] + \sum_i^{n_e}([JJ_{0i}] + [JJ_{i0}])q_i + \sum_i^{n_e}\sum_j^{n_e}[JJ_{ij}]q_iq_j\right)\frac{\boldsymbol{l_x}}{\partial \phi}\right] \quad ; \tag{6.47}$$

$$(Q_\Omega)_\phi = \frac{\partial T_1}{\partial \phi} + \frac{\partial T_2}{\partial \phi} - \frac{d}{dt}\left(\frac{\partial T_2}{\partial \dot{\phi}}\right) \quad , \tag{6.48}$$

where

$$\frac{\partial T_1}{\partial \phi} = \boldsymbol{v}^T(O')[\tilde{\omega}][A]_{/\phi}([I_1] + [\bar{S}]\boldsymbol{q_f}) + \Omega^2\boldsymbol{R}^T[A]_{/\phi}([I_1] + [\bar{S}]\boldsymbol{q_f}) \quad , \tag{6.49}$$

$$\frac{\partial T_2}{\partial \phi} = \dot{\boldsymbol{R}}^T[\tilde{w}][A]_{/\phi}([I_1] + [\bar{S}]\boldsymbol{q_f}) + ([I_1] + [\bar{S}]\boldsymbol{q_f})^T[\dot{A}]^T_{/\phi}(\boldsymbol{v}(O') + [\tilde{\omega}]\boldsymbol{R}) + \dot{\boldsymbol{q}}_{\boldsymbol{f}}^T[\bar{S}]^T[A]^T_{/\phi}(\boldsymbol{v}(O') + [\tilde{\omega}]\boldsymbol{R}) \quad , \tag{6.50}$$

$$\frac{d}{dt}\left(\frac{\partial T_2}{\partial \dot{\phi}}\right) = ([I_1]+[\bar{S}]\boldsymbol{q_f})^T \frac{d}{dt}\left([\dot{A}]_{/\dot{\phi}}\right)^T (\boldsymbol{v}(O')+[\tilde{\omega}]\boldsymbol{R}) \quad (6.51)$$
$$+([I_1]+[\bar{S}]\boldsymbol{q_f})^T[\dot{A}]_{/\dot{\phi}}[\tilde{\omega}]\dot{\boldsymbol{R}}+\dot{\boldsymbol{q}}_{\boldsymbol{f}}{}^T[\bar{S}]^T[\dot{A}]^T_{/\dot{\phi}}(\boldsymbol{v}(O')+[\tilde{\omega}]\boldsymbol{R}) \quad .$$

Finally, the dynamics of the generalized elastic coordinates is governed by

$$[m_{Rf}]^T\ddot{\boldsymbol{R}}+[m_{\phi f}]^T\ddot{\phi}+[m_{ff}]\ddot{\boldsymbol{q}}_{\boldsymbol{f}}+[k_{ff}]\boldsymbol{q_f}=(\boldsymbol{Q}_\nu)_f+(\boldsymbol{Q}_g)_f+(\boldsymbol{Q}_\Omega)_f \quad . \quad (6.52)$$

Terms in the preceding equation have the following expressions:

$$(Q_\nu)_f=\dot{\phi}^2([m_{ff}]\boldsymbol{q_f}+[I_0])+2\dot{\phi}[\tilde{S}]\dot{\boldsymbol{q}}_{\boldsymbol{f}} \quad ; \quad (6.53)$$

$$(Q_g)_f=-\frac{\partial U_1}{\partial \boldsymbol{q_f}}-\frac{\partial U_2}{\partial \boldsymbol{q_f}} \quad , \quad (6.54)$$

where

$$\frac{\partial U_x}{\partial \boldsymbol{q_f}}=\begin{bmatrix}\partial U_x/\partial q_1\\ \partial U_x/\partial q_2\\ \vdots\\ \partial U_x/\partial q_i\\ \vdots\\ \partial U_x/\partial q_{n_e}\end{bmatrix} \quad (6.55)$$

and

$$\frac{\partial U_x}{\partial q_i}=-\mu_x\left[-\frac{1}{|\boldsymbol{R_x}|^2}\boldsymbol{l_x}^T[\bar{S}]\frac{\partial \boldsymbol{q_f}}{\partial q_i}-\frac{1}{|\boldsymbol{R_x}|^3}([I_{0f}]+\boldsymbol{q_f}^T[m_{ff}])\frac{\partial \boldsymbol{q_f}}{\partial q_i}\right.$$
$$\left.+\frac{3}{|\boldsymbol{R_x}|^3}\boldsymbol{l_x}^T\left(\frac{1}{2}([JJ_{0i}]+[JJ_{i0}])+\sum_j^{n_e}([JJ_{ij}]+[JJ_{ji}])q_i\right)\boldsymbol{l_x}\right] \quad ; \quad (6.56)$$

$$(Q_\Omega)_f=\frac{\partial T_1}{\partial \boldsymbol{q_f}}+\frac{\partial T_2}{\partial \boldsymbol{q_f}}-\frac{d}{dt}\left(\frac{\partial T_2}{\partial \dot{\boldsymbol{q}}_{\boldsymbol{f}}}\right) \quad , \quad (6.57)$$

where

$$\frac{\partial T_1}{\partial \boldsymbol{q_f}}=[\bar{S}]^T[A]^T[\bar{\omega}]^T\boldsymbol{v}(O')+\Omega^2[\bar{S}]^T[A]^T\boldsymbol{R}+\Omega^2[I_{0f}]^T+\Omega^2[m_{ff}]\boldsymbol{q_f} \quad , \quad (6.58)$$

$$\frac{\partial T_2}{\partial \boldsymbol{q_f}} = [\bar{S}]^T[A]^T[\tilde{\omega}]^T\dot{\boldsymbol{R}}+[\bar{S}]^T[\dot{A}]^T(\boldsymbol{v}(O')+[\tilde{\omega}]\boldsymbol{R})$$
$$+2\Omega\dot{\phi}[I_{0f}]^T+2[m_{ff}]\Omega\dot{\phi}\boldsymbol{q_f}+\Omega[\tilde{S}]\dot{\boldsymbol{q}}_{\boldsymbol{f}} \quad , \quad (6.59)$$

$$\frac{d}{dt}\left(\frac{\partial T_2}{\partial \dot{\boldsymbol{q}}_{\boldsymbol{f}}}\right) = [\bar{S}]^T[\dot{A}]^T(\boldsymbol{v}(O') + [\tilde{\omega}]\boldsymbol{R}) + [\bar{S}]^T[A]^T[\tilde{\omega}]\dot{\boldsymbol{R}} + \Omega(\dot{\boldsymbol{q}}_{\boldsymbol{f}}{}^T[\tilde{S}])^T \quad . \tag{6.60}$$

If the free-modes are employed to discretize the elastic problem, the eq. (6.44) results strongly simplified. In fact, $[m_{Rf}]$ and $[m_{\phi f}]$ are null while $[m_{ff}]$ and $[k_{ff}]$ are diagonal matrix, where their i-th diagonal terms $(m_{ff})_i$, $(k_{ff})_i$ represent respectively the modal mass and stiffness of the i-th shape. On this bases, it also easy to introduce a modal damping matrix $[c_{ff}]$ to emulate energy dissipations due to the internal elastic motion of the structure. It yields to

$$[m_{ff}]\ddot{\boldsymbol{q}}_{\boldsymbol{f}} + [c_{ff}]\dot{\boldsymbol{q}}_{\boldsymbol{f}} + [k_{ff}]\boldsymbol{q}_{\boldsymbol{f}} = (\boldsymbol{Q}_\nu)_f + (\boldsymbol{Q}_g)_f + (\boldsymbol{Q}_\Omega)_f \quad . \tag{6.61}$$

where the matrix $[c_{ff}]$ is diagonal and the damping related to each modal shape $(c_{ff})_i$ is expressed through the nondimensional damping factor ξ_i as

$$(c_{ff})_i = 2\xi_i\sqrt{(m_{ff})_i(k_{ff})_i} \quad .$$

7 Analysis of the Dynamics of Flexibile Configurations

Contents

In the previous Chapter, the rigid fully-coupled formulation has been extended to integrate the elastic motion with the translational and rotational dynamics. In this Chapter, the effects of flexibility will be discussed. The first Section presents the two main concerns of simulating elastic motion in the vicinity of the Lagrangian points. The following Sections report the most interesting outcomes from the investigation of two basic configurations: a dumbbell and a cross satellite.

7.1 Two main issues

There are two main concerns that should be considered before simulating the motion of flexible space structures in orbit around the libration equilibria: the frequency of the elastic dynamics and the magnitude of the spacecraft deformations. The former is purely a numerical challenge while the latter will suggest also a physical conclusion.

Since the scope of this work is to study the coupling effects between dif-

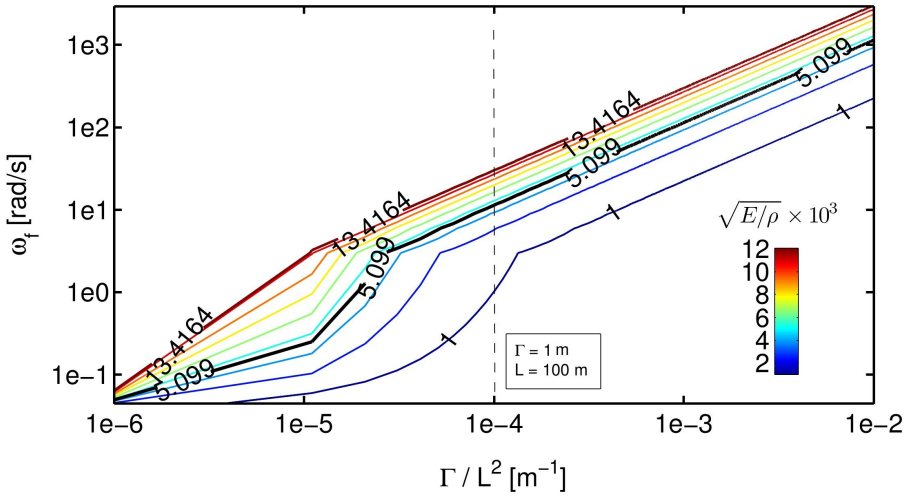

Figure 7.1: Natural angular frequency of the first mode for a free-free beam.

ferent dynamics, the integration of motion shall consider the characteristic velocity of each part included. In order to understand the range of frequencies typical of the elastic response, let us consider the angular frequency of the first normal mode of a free-free uniform beam

$$\omega_f = \lambda_1^2 \sqrt{\frac{E}{\rho}} \frac{\Gamma}{L^2} \quad , \tag{7.1}$$

where $\lambda_1 = 4.73$ is a parameter associated to the first mode, E and ρ denote respectively the Young's module and the density of the material, Γ is the inertia radius of the cross-section and L represents the beam length. In Figure 7.1 the angular frequency is plotted versus the beam topology (expressed by the ratio Γ/L^2) for a spectrum of $\sqrt{E/\rho}$ that reasonably covers the existing materials. In the contour, the value of $\sqrt{E/\rho}$ for the aluminum is highlighted in black. Likewise, the vertical dashed line shows the possible frequencies for beam a 100 m long with unitary Γ. Generally, the angular frequency of the first mode never goes below a rate of 10^{-2} rad/s. On the contrary, the frequency of the orbital motion is well smaller than this value; in Table 7.1, a low Earth orbit (LEO) may get close to it, but the gap between the natural frequencies of the elastic and orbital dynamics grows larger on a geostationary orbit (GEO) and becomes enormous for the Lyapunov periodic orbits. From the numerical perspective, as long as the two motions have to be solved together, the time step of the numerical

integration is determined by the faster dynamics. This means that, the integration step is reduced to the order of seconds (or even below) in order to correctly predict the elastic response. On the other hand, to investigate the coupling with the orbital motion, the simulation shall run at least for a time span comparable to the orbit period. Since the time span will be measured in days and the time step in seconds, it is straightforward to see that a critical numerical effort is required, in terms of the both memory request and computational time. Moreover, the distance between the frequencies shyly suggests that, under the natural dynamics, the rigid response will be likely decoupled from the elastic one; this would make badly used the computational resources required to simulate the coupled motion.

Table 7.1: Typical orbital angular frequencies.

Orbit Type	ω_{orb} **[rad/s]**
LEO	1.20×10^{-3}
GEO	7.27×10^{-5}
L_1 Earth-Moon, Large	3.28×10^{-6}
L_1 Earth-Moon, Small	6.20×10^{-6}
L_1 Sun-Earth, Large	2.27×10^{-7}
L_1 Sun-Earth, Small	4.08×10^{-7}

The structure deformations affect the orbital motion because changes in the mass distribution alter the resultant gravitational force. Thus, determining the order of the elastic displacements is useful to get a clue about their level of influence on the rigid dynamics. The stress and then the deformations (assuming a linear elastic relationship) are provoked by the gravity gradient over the space structure. For example, let us consider a dumbbell satellite, consisting of two equal masses at initial distance L; in addition, the two masses are located on the line through P_1-P_2. Considering each attractor by one, the two massive tips of the spacecraft undergo a different gravitational force, since they are not at the same distance from the source; expressing the force gradient in a first order series of the distance, it yields to

$$\Delta F \propto 2\mu_i \frac{L}{r_i^3} \quad , \tag{7.2}$$

where μ_i is the planetary constant of P_i and r_i is the radius measured from P_i. Of course, the same fashion of eq. (7.2) holds true for both the primary and the secondary. As depicted in Figure 7.2, the gravity gradient fields generated by P_1 and P_2 are either added or subtracted, but the neighbor-

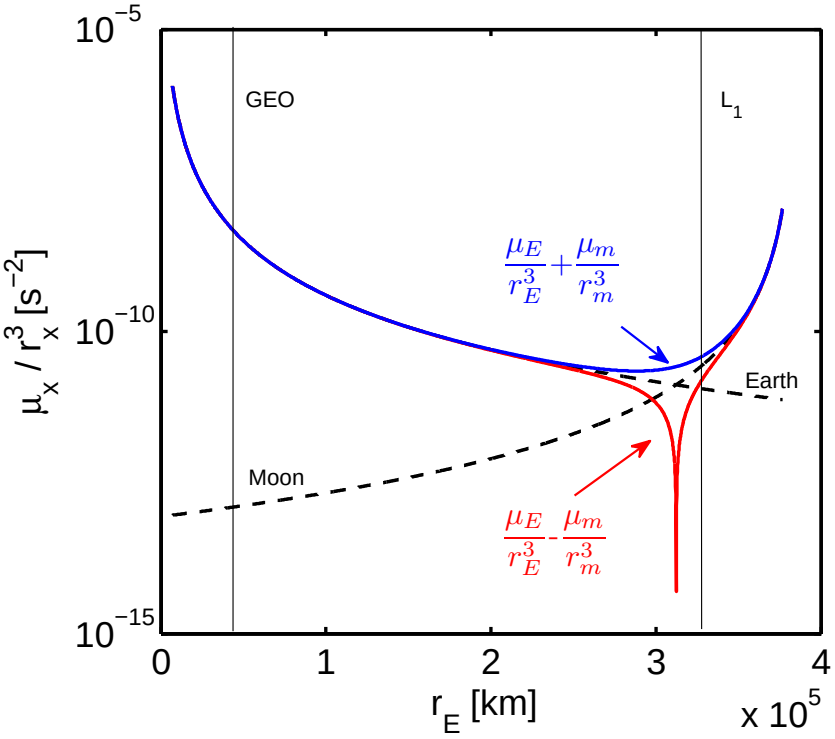

Figure 7.2: Trend of the gravity gradient magnitude.

hood of L_1 always represents a zone of minimal gravitational stress. For example, the solicitations exerted by the variation of the gravity field over the body extension in GEO are at least 100 times stronger than those experienced in vicinity of L_1. Additionally, this consideration can be applied to the gravity gradient torque, which is inversely proportional to the radius cubed as well as ΔF. As consequence, it is likely to predict small deformations of the vehicle, even if large space structure are addressed. Firstly, this leads the numerical problem to be ill-conditioned. In fact, the elastic displacements will be in the order of centimeters (or even smaller), while the orbital variables in the order of thousand of kilometers and the both belong to the same system of coupled equations supposed to be numerically integrated. However, this issue is partially solved employing the Encke's formulation of the orbital dynamics: integrating only the drift from the osculating trajectory, the orbital variables result adequately close to the elastic variables in terms of magnitude. Secondly, despite numerical difficulties of the coupled dynamics may be overcome, deformations of the mass distribution apparently remain too small to affect the rigid motions in vicinity of the libration equilibria.

In conclusion, arguments in this Section demonstrated that, the rigid and the elastic dynamics in vicinity of the Lagrangian points take place on critically different scales, from the both temporal and spatial perspectives. Thus, the coupling, that exists theoretically, could be practically ineffective. For this reason, the continuation of the work drops the plan of studying actual space structures and instead focus on investigating the dynamics of very flexible and very simple configurations. Since it has been realized that the gravitational stress is minimal in the area of the Lyapunov orbits, an extremely low level of stiffness (not sustainable nearby Earth) can be introduced in a structure orbiting inside that zone. Thus, the values of stiffness that will assumed next do not clearly refer to any existing materials or typical concrete structure. Alternatively, they can be interpreted as the preliminary model of some mechanism or control action; moreover, the structure itself does not necessarily correspond to an unique vehicle, but may represent a flying formation as well. The choice of elementary architectures is instead motivated to have a more meaningful insight, focusing on the main peculiarities of the phenomenon, without the complication of a arbitrary topology.

7.2 Dumbbell Configuration

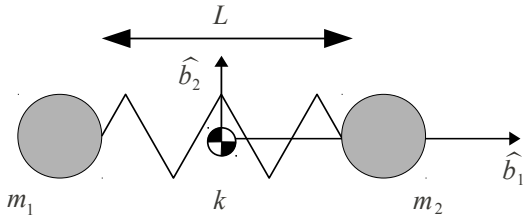

Figure 7.3: Skecth of the dumbbell satellite.

Figure 7.3 shows the simplest flexible configuration: two masses joined by a spring, the well-known dumbbell satellite. Because of the lack of sophistication, the results are more easily interpretable, making this pattern ideal to start a novel investigation. In addition, its shape variation can be fully described by a linear field of elastic displacements, which respects the assumptions of the formulation developed in Chapter 6, without any sort of approximation. It means that, large variation of shape can be studied without violating the model. Specifically, the deformation is axial and corresponds to vary the configuration characteristic length.

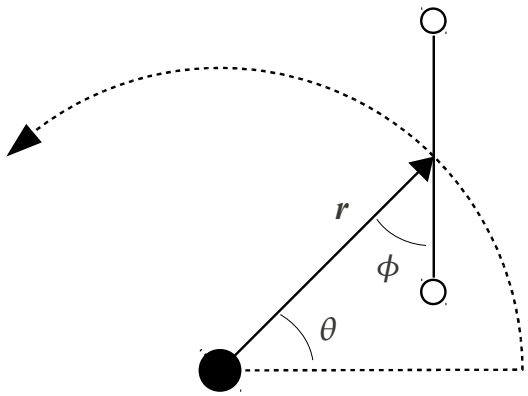

Figure 7.4: Kinematic scheme in the R2BP.

The dumbbell is already common in the Restricted Two-body Problem (R2BP), since it was the basic model for tether satellites. This configuration was particularly used to experiment new forms of control that exploit the interaction between shape and orbital dynamics [84, 85], shape and attitude dynamics [86] or all three dynamics coupled [87]. Adopting the Lagrangian formulation, the fully-coupled equations of motion in the R2BP can be derived with few algebra. To this end, the generalized coordinates are defined as depicted in Figure 7.4: r is the radial distance from the celestial body, θ is the true anomaly, ϕ is the angle relative to the radial, positive when counterclockwise. The elastic degree of freedom is denoted with l, so that $2l$ is the length of the dumbbell. Given these generalized coordinates, the Lagrangian function of the system is

$$\mathcal{L} = m(\dot{r}^2 + \dot{l}^2 + l\dot{\phi}^2 + 2l^2\dot{\phi}\dot{\theta} + (r^2 + l^2)\dot{\theta}^2) - U_g - 2k(l - l_0)^2 \quad , \tag{7.3}$$

where $m = m_2 = m_2$ stands for the tip mass and l_0 is defined such that $2l_0$ is the initial length of the dumbbell; the gravitational potential is

$$U_g = -\frac{\mu m}{\sqrt{l^2 + r^2 - 2lr\cos\phi}} - \frac{\mu m}{\sqrt{l^2 + r^2 + 2lr\cos\phi}} \quad , \tag{7.4}$$

with μ being the planetary constant. It should be noticed that

$$\frac{\partial \mathcal{L}}{\partial \theta} = 0 \quad , \tag{7.5}$$

then the angular momentum

$$p = \frac{\partial \mathcal{L}}{\partial \dot{\theta}} = 2m(l^2\dot{\phi} + (r^2 + l^2)\dot{\theta}) \tag{7.6}$$

is conserved. Hence, the equations of motion can be written, after some math, in the reduced form as [86]

$$\begin{aligned}\ddot{r} &= \frac{rl^4}{(r^2+l^2)^2}\dot{\theta}^2 + \frac{p^2 r}{4m^2(r^2+l^2)^2} - \frac{rl^2 p}{m(r^2+l^2)^2}\dot{\phi} \\ &\quad -\mu\frac{r - l\cos\phi}{2(r^2+l^2-2lr\cos\phi)^{3/2}} \\ &\quad -\mu\frac{r + l\cos\phi}{2(r^2+l^2-2lr\cos\phi)^{3/2}}\end{aligned} \tag{7.7}$$

$$\begin{aligned}\ddot{\phi} &= \frac{2(l^3\dot{r} + r^3\dot{l})}{rl(r^2+l^2)}\dot{\phi} - \mu\frac{(r^2+l^2)\sin\phi}{2lr(r^2+l^2-2lr\cos\phi)^{3/2}} \\ &\quad +\mu\frac{(r^2+l^2)\sin\phi}{2lr(r^2+l^2+2lr\cos\phi)^{3/2}} - \frac{p(r\dot{l} - l\dot{r})}{mrl(r^2+l^2)}\end{aligned} \tag{7.8}$$

$$\begin{aligned}\ddot{l} &= \frac{r^4 l}{(r^2+l^2)^2}\dot{\phi}^2 + \frac{p^2 l}{4m^2(r^2+l^2)^2} + \frac{r^2 pl}{m(r^2+l^2)^2}\dot{\phi} \\ &\quad -\mu\frac{q - r\cos\phi}{2(r^2+l^2-2lr\cos\phi)^{3/2}} - \mu\frac{q + r\cos\phi}{2(r^2+l^2+2lr\cos\phi)^{3/2}} \\ &\quad -\frac{2k}{m}(l - l_0) \quad .\end{aligned} \tag{7.9}$$

The numerical solution of eq. (7.7), (7.8), (7.9) can be compared to the results obtained from the general algorithm developed in the previous Chapter. For instance, consider a dumbbell spacecraft defined by $m_1 = m_2 = 200$ kg, initial length 100 m and spring stiffness 10 N/m, flying on a circular orbit with semi-major axis $a = 7000$ km and possessing an initial angular velocity $\dot{\phi}_0 = -\dot{\theta}_0$. Figure 7.5 reports a satisfactory agreement between the two responses produced. Note that the elastic motion is plotted as length variation relatively to the undeformed geometry $q_f = l - l_0$.

Recently, a lot of interest has risen for dumbbell or tether spacecrafts in the R3BP as well. They are sought as possible alternatives to formation flight missions that require an extremely accurate formation control, such as interferometry missions [88, 89]. So far, many of the papers published have focused on demonstrating the feasibility and improving the performance of varying-length tether systems to control the unstable nature of the collinear Lagrangian points [90]. Others have investigated the deployment and the station-keeping of dumbbells at L_2, in a fully coupled regime

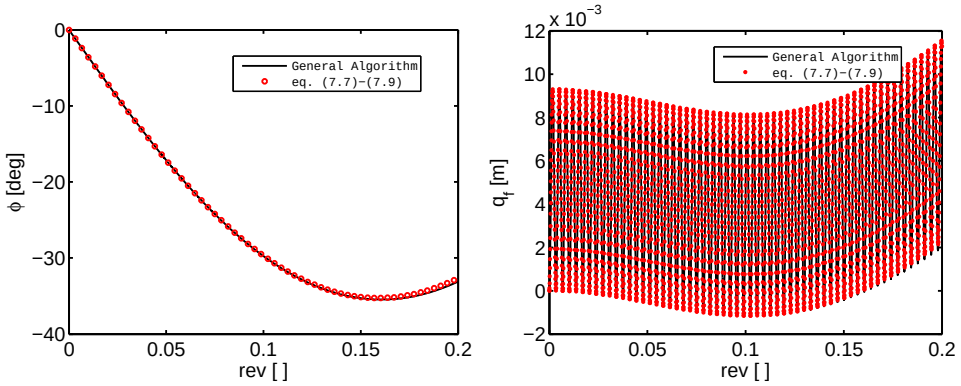

(a) Attitude (b) Shape

Figure 7.5: Comparison of attitude and elastic motions of a dumbbell satellite in Earth orbit.

using approximations of the orbital motion [90]. In this work, it will be addressed the natural dynamics of a very flexible dumbbell architecture describing the orbital motion without simplifications of the CR3BP.

First of all, it is necessary to express the elastic deformation in terms of displacement from the undeformed geometry using the normal modes. Trivially, the dumbbell has only one elastic degree of freedom q_f (which physically represents the distance variation between the two masses) and the displacement of m_1 results, on the basis of the b-frame, as

$$\boldsymbol{u_f} = [S_1]q_f = \begin{bmatrix} -\dfrac{m_2}{m_1+m_2} \\ 0 \end{bmatrix} q_f \quad , \tag{7.10}$$

while for the other mass m_2

$$\boldsymbol{u_f} = [S_2]q_f = \begin{bmatrix} \dfrac{m_1}{m_1+m_2} \\ 0 \end{bmatrix} q_f \quad . \tag{7.11}$$

As done before, a reference configuration is convenient to identify the most distinguishing behaviors of a dumbbell structure on Lyapunov periodic orbits. Then, the parameters of the configuration will vary to study the novel mechanisms revealed. The staring parameters of the dumbbell are reported in Table 7.2. There, k refers to the stiffness of the connection between the masses m_1, m_2 and ξ denotes the damping factor of the unique modal shape of this structure.

L [km]	m_1 [kg]	m_2 [kg]	k [N/m]	ξ [ndim]
500	300	300	1×10^{-4}	0.001

Table 7.2: Parameters of the reference dumbbell configuration.

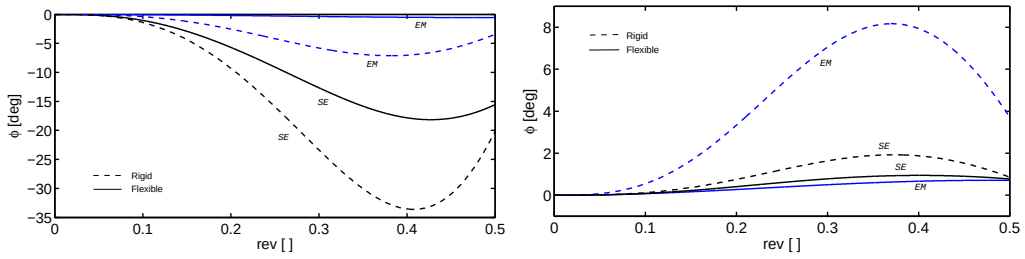

(a) from L_1 family. (b) from L_2 family.

Figure 7.6: Attitude of a flexible dumbbell satellite on a small Lyapunov orbit.

The first analysis explores the operative environment. On large Lyapunov orbits, it is noticed that the reference spacecraft cannot withstand the angular acceleration provoked by the gravity gradient torque and the elastic part diverges (the distance between the two mass grows toward infinity). Conversely, on small size orbits the elastic response is oscillatory with bounded amplitude around a mean elongation trend. The overall stretching of the dumbbell causes the damping of the attitude motion as consequence of the Coriolis effect, as shown in Figure 7.6. This mechanism appears in both the Sun-Earth (SE) and Earth-Moon (EM) system, regardless the family the orbit is picked up from. Now as later, the only concern is on the coupling between attitude and elastic dynamics, since in none of the simulations performed the orbital motion seems to be noticeably affected by flexibility, even for significant shape variation (elongations $\sim$ km).

To proceed further, the attitude damping discovered on small Lyapunov orbits is examined as function of the dumbbell stiffness. The equilibrium point L_2 of the Sun-Earth system is selected for this study, because largely indicated as the ideal location of binary flight formations to observe the universe, such as the O-labeled baseline of the Terrestrial Planet Finder [91]. Secondly, the values of stiffness used in this analysis are related neither to any existing material nor monolithic structure, but instead can be interpreted as the gain of a proportional controller, that employs electric thruster to keep the length of a binary flying formation within a certain tolerance (assuming no transversal errors). For example, the NASA Next

thruster offers a maximum force of 200 mN [92], that reasonably matches the gains here assumed. As appears in Figure 7.7, the lower is the stiffness, the greater is the damping. The stiffness regulates the distribution of energy between the attitude and the elastic motion: softer architectures store more easily energy in the shape axial deformation rather than in rigid rotation. The mutual influence of attitude and length variation of the dumbbell should be keep in mind while designing the configuration and could be exploited as a possible tool of passive control (at least from the attitude perspective). It is also worth to notice in Figure 7.7 that, for $k = 0.01$ N/m the curve is practically indistinguishable from the rigid solution. Such stiffness is undoubtedly much smaller than any value attributable to a concrete classic structure. Therefore, it is justified the choice of stepping back on structures in the narrow sense of the word, since the coupling effects of the natural dynamics, associated to their equivalent stiffness, would be extremely faint. On the other hand, this also means that Large Space Structures do not really need an elastic coupled analysis, as long as common stiffness and structures are considered.

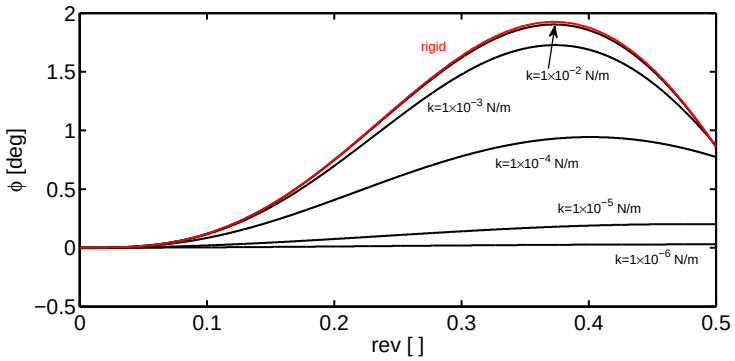

Figure 7.7: Attitude of a dumbbell satellite on a small Lyapunov orbit varying the internal stiffness.

Hence, it is verified that parameters such the dumbbell length or the mass ratio between the two tips do not trigger radical changes of the response nature. Of course, they affect the elastic motion, but those variation have slight repercussions on the rigid solution. Actually, the unique alteration of the pitch response, related to modifications of the initial distance between m_1 and m_2, is observed when the dumbbell departs from the nominal orbit as consequence of its extension (see Figure 7.8-(a) and its inset). The ratio among masses m_1/m_2 has limited effects on the attitude solution as well. Close curves can be observed in Figure 7.8-(b). More interesting is noticing that, despite the substantial initial length (*i.e.* 500 km), the

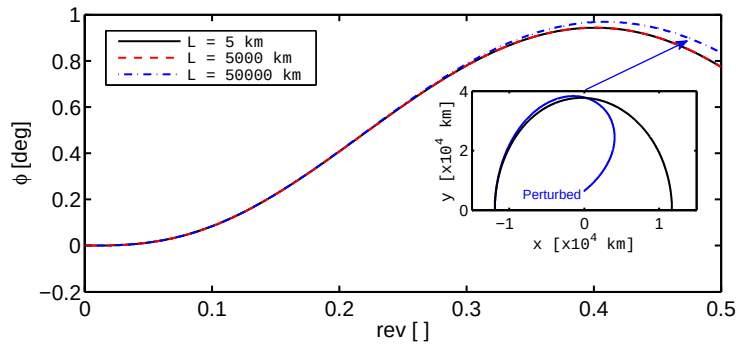

(a) Initial length L.

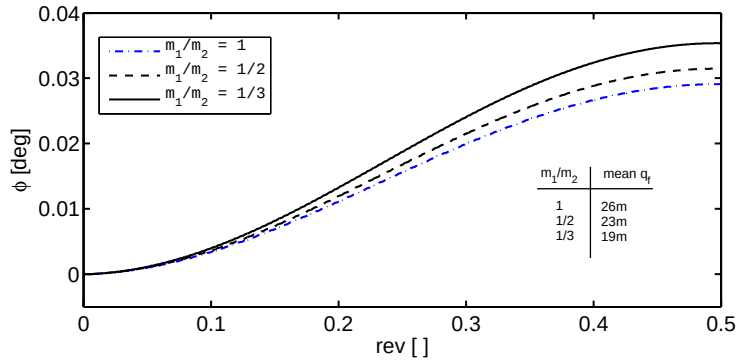

(b) Mass ratio m_1/m_2.

Figure 7.8: Attitude of a dumbbell satellite on a small Lyapunov orbit varying the configuration parameters.

mean elongations are about few dozen of meters, reinforcing the assumption of small deformations. All considered, the dynamics of a dumbbell configuration offers a good robustness to the both initial length and mass distribution, that can be exploited as design flexibility. In other words, the qualitative dynamics of the dumbbell can be predicted quite reliably, even if the exact details of the architecture are not known at that point of the design process.

In Chapter 4, it has been shown that a distribution of mass extended in a single direction ($k_3 = 1$) undergoes a divergence of the pitch angle along large Lyapunov orbits. The dumbbell falls within this category. Thus, the last part of this study is aimed at understanding whether is possible or not to exploit the coupling between the attitude and elastic dynamics as a mean to limit the spacecraft rotational motion on a large Lyapunov periodic orbit. The idea follows the observation of the attitude damping effects on smaller orbits; in that case, the stiffness demonstrated an effec-

tive parameter to tune the phenomenon. Therefore, the dumbbell is made progressively more flexible as reported in Figure 7.9. The general trend does not differ from that discovered on small Lyapunov orbits: an increase level of damping corresponds to a softening of the stiffness. Honestly, the rigid divergence is avoided, but the resultant solution cannot be really considered as bounded. A better insight may be offered by a longer period of integration. Unfortunately, it is not possible to lower the stiffness any further to get a stronger damping effect, because the aforementioned elastic divergence appears. Trivially, if the bond between the two masses is too weak, it cannot withstand the solicitations generated during the motion.

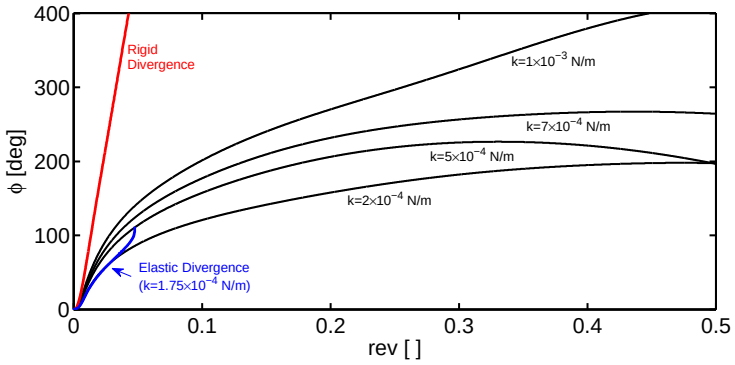

Figure 7.9: Attitude of a dumbbell satellite on a large Lyapunov orbit varying the internal stiffness.

A last attempt with the same purpose is made acting on the internal damping factor of the dumbbell. However, the internal damping proves an ineffective parameters for the stated intention. In fact, the desired objective is not achieved even exploring a large range of ξ. On the contrary, Figure 7.10 demonstrates that large variations may lead to undesired behaviors or be simply useless. On one hand, a damping factor too low cause the motion to diverge, on the other, above a certain limit, ξ does not alter the response anymore. Both the phenomena are clearer in the inset of Figure 7.10, that depicts the elongations of the dumbbell. It should be noted as the oscillations amplitude increases indefinitely for $\xi = 0.0001$, while it is quickly damped down for $\xi = 0.01$. In the latter, the initial transitory is a marginal part of the response, so greater levels of internal damping can only make this component of the solution more marginal. This is the reason why no modifications of the coupling effects appear above a certain threshold of ξ.

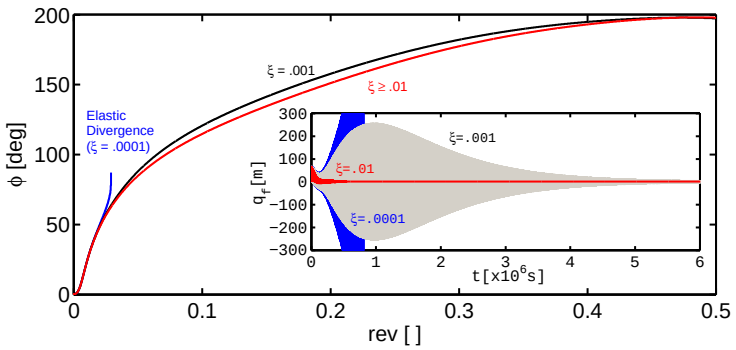

Figure 7.10: Attitude of a dumbbell satellite on a large Lyapunov orbit varying the internal damping.

7.3 Cross Configuration

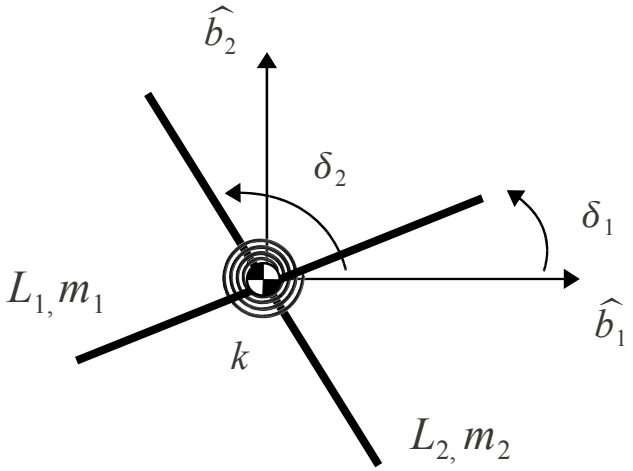

Figure 7.11: Skecth of the cross satellite.

The cross-satellite is the second elementary configuration selected after the dumbbell topology. The dumbbell has been chosen because of its sensitivity to the gravity gradient force in the positions space (it can be demonstrated that, for a given structure, the maximum axial solicitation exerted by spatial gravity gradient is much stronger than the maximum transversal action); likewise, the cross shape is ideal to test relative rotations between parts of the structure which are subject to a different gravity gradient. In fact, each component undergoes a distinct torque according to its orientation and so an own motion, if it is free to rotate. Hence, the architecture shown in Figure 7.11 is employed: two uniform branches with mass m_1, m_2 and length L_1,L_2 respectively, that are joined in their centers of mass

Table 7.3: Parameters of the reference cross configuration.

L_1 [m]	L_2 [m]	m_1 [kg]	m_2 [kg]	δ_1 [deg]	δ_2 [deg]	k [Nm]	ξ [ndim]
50	50	100	100	0	90	0.001	0

by a torsional spring k. Eventually, it will also be accounted an internal dissipation of the joint, that is expressed through the damping factor ξ of the unique modal shape of this structure. The b-frame is located as usual in the center of mass of the spacecraft and the position of the two segment of the cross is determined by the angles δ_1, δ_2. For convenience, the reference configuration detailed in Table 7.3 is selected ; when not explicitly stated, the simulation assumes the data presented in the latter Table. The nominal cross has no internal damping. Furthermore, the satellite at the time $t = 0$ is conventionally aligned to the ℓ-frame, with null angular velocity and placed at the crossing of the P_1-P_2 line, on the left of the libration point. To incorporate shape changes of the body in the formulation developed in Chapter 6, it is necessary to express the elastic displacements in the linear form using the normal modes; thus, written in the b-frame they appear as

$$\boldsymbol{u_f} = [S_1]q_f = -\frac{1}{\chi}\begin{bmatrix} -\sin\delta_1 \\ \cos\delta_1 \end{bmatrix} s\, q_f \tag{7.12}$$

for the first branch and

$$\boldsymbol{u_f} = [S_2]q_f = \left(1 - \frac{1}{\chi}\right)\begin{bmatrix} -\sin\delta_2 \\ \cos\delta_2 \end{bmatrix} s\, q_f \tag{7.13}$$

for the second branch, where s is the arc length along the axis of each single segment and

$$\chi = 1 + \frac{m_1 L_1^2}{m_2 L_2^2} \quad . \tag{7.14}$$

The generalized elastic coordinate q_f is physically the relative rotation between the cross branches $q_f = \Delta\delta_2 - \Delta\delta_1$, where $\Delta\delta_1$, $\Delta\delta_2$ are the tilt changes of each segment relatively to the undeformed geometry. It should be noticed that, in this representation, elastic rotations are linearized and therefore its applicability is limited to small angles.

The first analysis addresses the operative environment in the Earth-Moon system. In this scenario, the most fascinating outcome is the evolution of the elastic behavior summarized in Figure 7.12. The solution of the internal rotation, along a small Lyapunov orbit, presents clearly two superposed oscillations, regardless the belonging to the L_1 or L_2 family:

one global fluctuation follows the orbital motion, the other represents the local elastic transitory. Starting with orbits around L_1, the size increase initially leads the global component to overcome distinctly the amplitude of the local transitory oscillations. It is evident from Figure 7.12-(c) that, the deformation acts in accordance with the fashion of the gravity gradient torque (discussed in Chapter 5). In fact, the peaks of q_f are larger and closer than those reported in the previous case (*i.e.* small Lyapunov), in agreement with the evolution of the gravitational momentum trend. However, a further enlargement of the orbit provokes a new alteration of the solution nature: the secular component is dominant in the first half of the orbital path, while the local transitory prevails in the second half. The secondary anomaly triggers sudden elastic oscillations, whose amplitude is surprisingly greater than the other observed so far. Actually, since no damping is accounted, referring to this component as transitory part of the solution is misleading, because these fluctuations remain throughout the subsequent motion. To understand this mechanism, it is worth to recall the secondary anomaly. In this work has been discovered (see Chapter 5) that, the gravity gradient torque has a truly non linear trend along large periodic orbits; specifically, its maximum and minimum values are both extremely close to the crossing of the attractors axis, in vicinity of the secondary. This means that the solicitation varies from the peak to the gorge in a small span of time, to the extend that the curve slope almost approaches the 90 degrees. This instantaneous local variation excites the vibrations to a level much greater than the mean global motion does, so they become the only visible trend after the critical event. A similar outcome appears also on the L_2 family with some slight diversity. In this case, the peaks move toward the sides of the plots simply because the initial position is the closest to the secondary; hence, oscillations due to the secondary anomaly start immediately, rather than at half revolution. In addition, it is noticed that their amplitude is one order of magnitude larger than the equivalent reported for the orbit around L_1.

The reference cross configuration is axisymmetric (*i.e.* $k_3 = 0$), so the attitude is not of any concern for the first part of this study. The gravity moment is null on the undeformed spacecraft: its orientation is actually perturbed by the small shape changes, but always remains in close proximity of the initial orientation. The current focus is on the coupling between the orbital and elastic motion. It is worth to remark that the influence is mostly directed from the orbital dynamics to the elastic dynamics; it holds true the conclusion of the previous section: no real alterations of the orbital motion are discovered in relationship with the spacecraft flexibility among

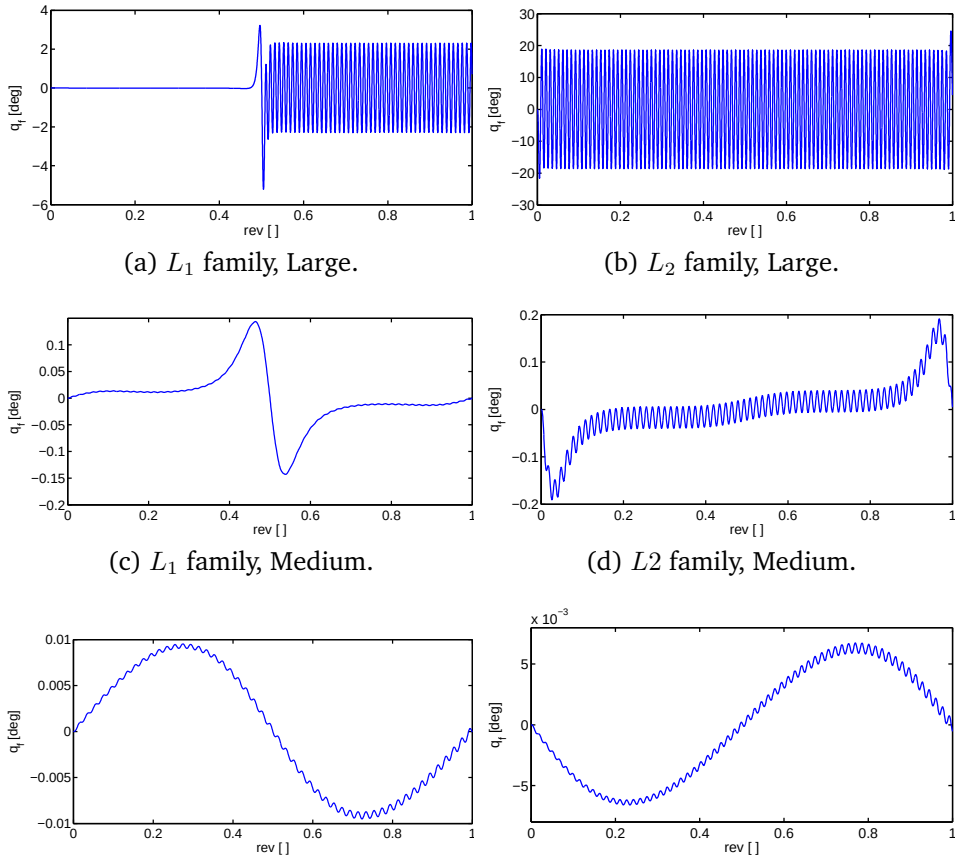

(a) L_1 family, Large.

(b) L_2 family, Large.

(c) L_1 family, Medium.

(d) $L2$ family, Medium.

(e) $L1$ family, Small.

(f) $L2$ family, Small.

Figure 7.12: Cross satellite. Elastic coordinate along Lyapunov orbits differing by size and family.

the large number of cases examined. In the following, it is demonstrated that the opposite coupling (*i.e.* orbital input on elastic response) changes nature during the stiffness increase. The phenomenon appears clearly on a small Lyapunov orbit. As discussed earlier, the solution is composed by global and local oscillations, the former related to the orbital motion, the latter related to the elastic transitory. In a highly flexible structure the amplitude of the global fluctuation prevails on the local oscillations. It is observed in Figure 7.13 that as the joint between the cross branches becomes stiffer, the ratio will be inverted. For example, in the first shift of stiffness form $k = 0.001$ Nm/[rad] to $k = 0.1$ Nm/[rad], the orbital driven fluctuation is still faintly visible in the transitory oscillations, but it disappears in the next increase to $k = 10$ Nm/[rad]. Figure 7.13 also shows the effects of stiffness variations on a large Lyapunov orbit. Here, form $k = 0.001$

Nm/[rad] to $k = 0.1$ Nm/[rad] the librations triggered by the secondary anomaly are critically reduced, but the peaks remain evident and eventually, for $k = 10$ Nm/[rad], the anomaly vanishes too.

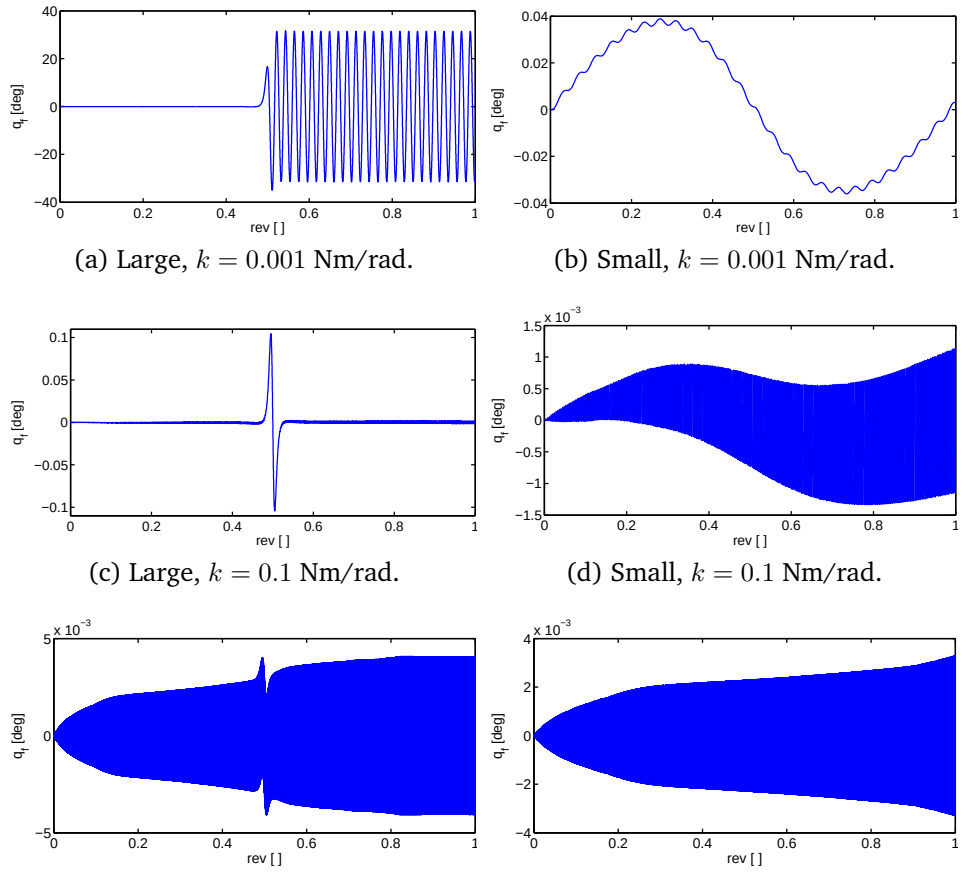

(a) Large, $k = 0.001$ Nm/rad.

(b) Small, $k = 0.001$ Nm/rad.

(c) Large, $k = 0.1$ Nm/rad.

(d) Small, $k = 0.1$ Nm/rad.

(e) Large, $k = 10$ Nm/rad.

(f) Small, $k = 10$ Nm/rad.

Figure 7.13: Cross satellite. Influence of the internal stiffness on the elastic coordinate along Lyapunov orbits from the L_1 family.

Introducing a non-axisymmetric distribution of mass, the secondary anomaly has unexpected consequences on a flexible cross-satellite. Specifically, on a large Lyapunov orbit from the L_1 family, the anomaly excites wide elastic vibrations of the structure, that in turn freeze the spacecraft spin. Figure 7.14 surely describes better what occurs to the attitude motion for several values of k_3 (k_{crit} refers to the resonant value of a rigid body, when the orbit is linearly approximated, see Chapter 4). The energy seems to be suddenly transfered to the elastic dynamics. The phenomenon is not completely understood yet, and further studies are encouraged. Pre-

liminarily, it may be advanced the hypothesis that the angular momentum relocates from rigid rotations into relative rotations and deformation energy. It can be inferred observing the rigid response in Figure 7.14 that, the system prefers to allocate the energy into the elastic dynamics rather than inverting the spin direction (suggested by the curve slope). The next Figure 7.15 shows that this mechanism exists for any arbitrary topology with $k_3 \neq 0$, but the nature of the solution changes again with $k_3 \to 1$: subsequently to the anomaly the motion neither inverts the direction nor freezes. On the contrary, the response curve retains an opposite concavity and the pitch motion diverges. Not surprisingly, the elastic dynamics, depicted in the inset of Figure 7.15, is mutated too.

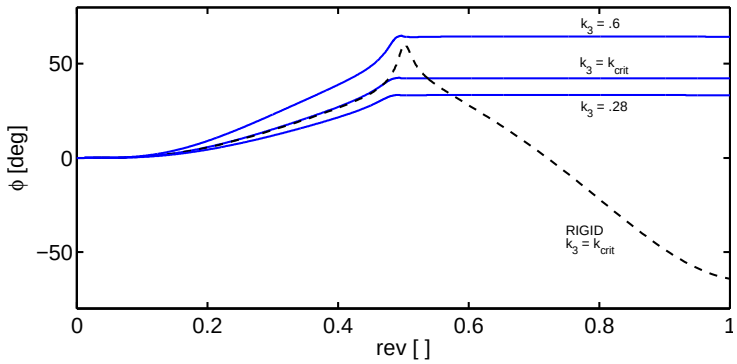

Figure 7.14: Cross satellite. Pitch angle along a large periodic orbit about L_1 for different inertia ratios.

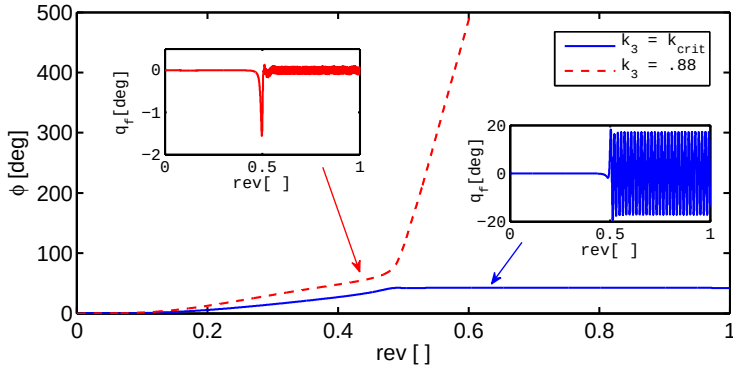

Figure 7.15: Cross satellite. Pitch angle along a large periodic orbit about L_1 for $k_3 = 0.88$.

Given a specific value of k_3, the joint stiffness of the cross controls the qualitative fashion of the solution as well. It is meaningful to observe the

same general behaviors noticed varying k_3 with k fixed. Since k_3 determines the frequency of the attitude natural dynamics and k the frequency of the elastic vibrations, discovering the same mechanisms is a further proof of the mutual coupling and also leads to aim new studies at characterizing the response as function of the ratio between the aforementioned frequencies. Presently, the two parameters are addressed separately. For example, Figure 7.16 reports the different rotational motions for a structure defined by $k_3 = 0.28$ and variations of the stiffness level. In the case of $k = 0.1$ Nm/[rad] the trend is extremely close to the rigid response; it confirms that, the stiffness required to essentially reproduce the dynamics of a rigid body is far smaller than the effective stiffness of any common monolithic spacecraft. One order of magnitude below, the dynamics changes again and the pitch angle departs toward infinity after the secondary anomaly (notice the parallel to $k_3 \to 1$). A further downgrade to $k = 0.001$ Nm/[rad] makes the plateau to reappear, which means that the orientation of the spacecraft remains practically constant in the ℓ-frame, once past the P_2 closest encounter. In summary, three different dynamics, which depend on both the spacecraft topology and internal stiffness, may take place due to the secondary anomaly:

1. the vehicle continues to spin in the same direction.
2. the vehicle inverts the direction of spin.
3. the vehicle stops spinning.

It is not still known if other possible dynamics exist in the transition between those mentioned. So far, the investigation focused on varying the order of magnitude of the governing parameters, but the exact identification of the bifurcation points of the dynamics would be certainly important.

It should be noticed from Figure 7.16 that the simulations run for a period long enough to allow at least two close passages nearby the secondary. The effects of the multiple encounters on the attitude dynamics are already manifest in Figure 7.16. In particular, when the cross-satellite freezes its orientation because of the first passage, the pitch angle remains constant even after the subsequent one. Considering this case, it would be interesting to figure out the evolution of the elastic deformations. Thus, chosen $k_3 = 0.28$, the elastic solution is offered by Figure 7.17. The oscillations of the undamped system alternate between increase and decrease of their amplitude each time the spacecraft passes through the secondary anomaly. However, this conclusion cannot be extend beyond the example presented; as matter of fact, also subsequent increases of the amplitude are detected

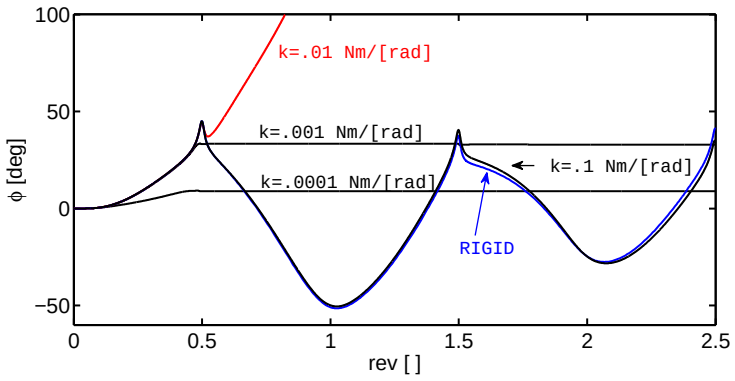

Figure 7.16: Cross satellite. Effect of the internal stiffness on the pitch angle along a large periodic orbit about L_1 for $k_3 = 0.28$.

for other inertial ratios. A more predictable scenario is obtained introducing a damping of the elastic rotation; if the oscillations are sufficiently smoothed between two consecutive passages, the secondary anomaly alway boosts up the vibrations.

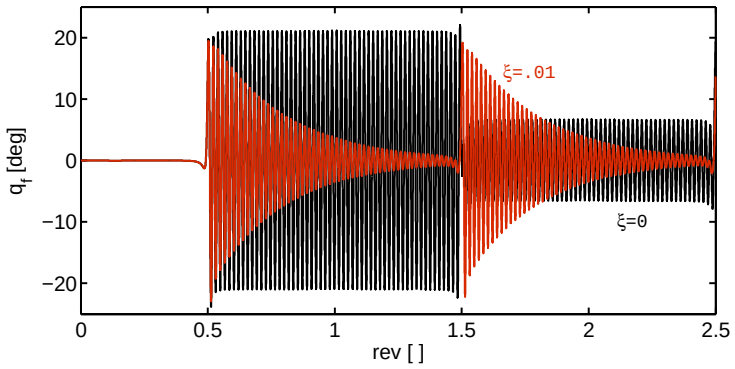

Figure 7.17: Cross satellite. Elastic coordinates along a large periodic orbit about L_1 for $k_3 = 0.28$ and $k = 0.001$ Nm/[rad].

So far, the two branches of the cross have been assumed orthogonal. Thus, it is worth to investigate other relative angular positions of the cross segments. To this end, the angle δ_2 will vary and δ_1 will remain equal to zero. Looking at Figure 7.18, δ_2 reveals to be a powerful parameter to target a desired frozen pitch angle after the secondary anomaly. Additionally, despite the fact that no evidence are shown for sake of brevity, it is observed that the structure vibrations are not any more around the undeformed geometry, but instead there is a mean trend to reduce the angle between the two branches, in order to align every components of the architecture along

the stable direction of the gravity gradient torque.

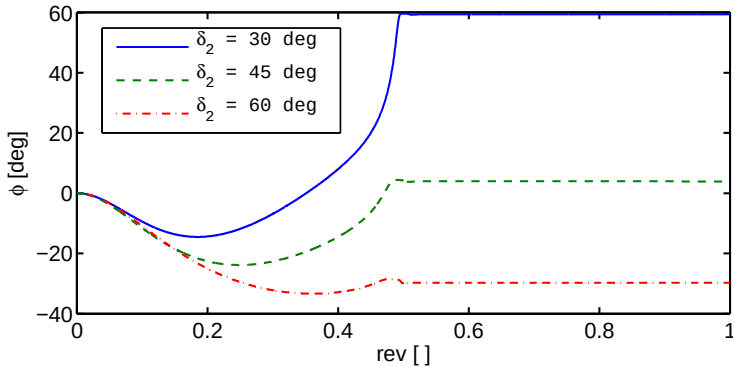

Figure 7.18: Cross satellite. Pitch angle along a large periodic orbit about L_1 for different cross shapes.

Finally, it is discussed the most relevant outcome of an analogous analysis campaign in the L_2 family of Lyapunov periodic orbits. The result concerns the attitude dynamics along a large orbit and is obvious in Figure 7.19: the introduction of a sufficient degree of flexibility is able to convert the pitch solution from diverging to bounded. Even if not appreciable on the axis scale of Figure 7.19, the motion is restrained within ± 20 degrees for $k = 0.001$ Nm/[rad]. On one hand, this is another clear proof that the elastic dynamics is mutually coupled to the rigid dynamics (at least to the rotational component); on the other, it suggests novel means of passive stabilization of the vehicle orientation, based on the elastic oscillation of elements of the structure itself. To demonstrate that the oscillations are really responsible for keeping the attitude stable, a damping factor is added in the response presented Figure 7.20. The comparison shows beyond doubt that, as long as the vibrations are extinguished enough rapidly, the pitch angle returns to grow indefinitely.

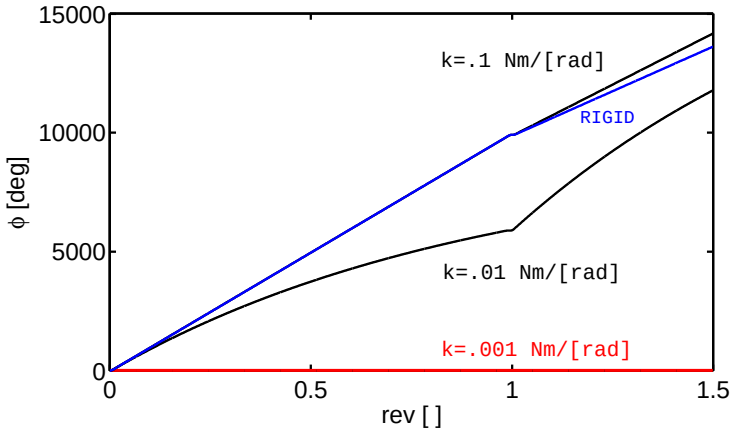

Figure 7.19: Cross satellite. Effect of the internal stiffness on the pitch angle along a large periodic orbit about L_2 for $k_3 = 0.88$.

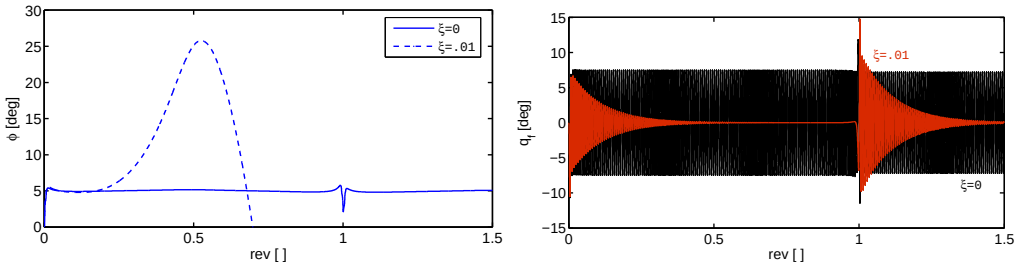

(a) Pitch angle. (b) Elastic coordinate.

Figure 7.20: Cross satellite. Response along a large periodic orbit about L_2 for $k_3 = 0.88$ and different damping.

8 Conclusions

Contents

Many of the future missions to move up in space exploration are proposed in vicinity of the Lagrangian points of the both Earth-Moon and Sun-Earth systems. The breakthrough would be placing long-life large structures in such locations to serve as fertile points of observation of the universe or as space dock for missions in the Solar System. In this scenario, the dynamics is highly nonlinear and characterized by high sensitivity to initial conditions, so even small perturbations may force the spacecraft to depart from the nominal trajectory. Furthermore, the attitude response in such an environment is not yet fully and systematically portrayed. Therefore, a deeper insight into the natural dynamics will surely improve the design of the aforementioned missions and will be eventually able to advance new design and control strategies. Large Space Structures are by definition architectures of considerable extension. Thus, the effects of the gravity gradient over the mass distribution are included in the dynamics formulation. This leads the orbital and attitude dynamics to mutually interact. Similarly, the area of the exposed surfaces to the solar radiation pressure is likely greater than other cases. At this point, the solar radiation pressure is included into the model as well. Then, astute solutions of the fully-coupled dynamics under the solar radiation pressure are proposed. These solutions

significantly abate the control effort on both the orbital and attitude motions to the extent that it may not be even required in some circumstances. Finally, Large Space Structures likely possess a higher level of flexibility either as a whole or because of some components. Hence, the elastic dynamics are added to the differential equations of motion. Since the stress provoked by the gravity field is minimal in the neighborhood of the first two libration points, the deformations are consequently small and do not apparently alter the rigid-body solution of the classic structure. However, very flexible and very simple configurations are employed to explore this scenario. Such configurations may represent formation flying vehicles as well as interconnected systems. The results show some unexpected mutual interactions between orbital, attitude and elastic motions and suggest possible novel ways to exploit shape changes as effective tools to control the spacecraft orientation.

8.1 Rigid Fully-Coupled Motion

A novel study on the gravity gradient over the spacecraft mass distribution in the Planar Circular Restricted Three-Body Problem is reported in this work. Expanding the gravitational potential in Taylor series up to (at least) the second order terms supplies the key to develop a more accurate dynamical model. The gravity gradient not only affects both the orbital and attitude motion, but also coupled two dynamics usually addressed independently. Its effects on Lyapunov periodic orbits are observed for the first time. Unlike in the Restricted Two-Body Problem, this perturbation is able to push the spacecraft away from the nominal trajectory within a relatively short span of time, comparable to a few orbit periods. This perturbation is analyzed in the Earth-Moon and Sun-Earth systems, resulting stronger in the former. Additionally, the final radial displacements observed on periodic orbits of the L_2 family are greater than those reported on the L_1 counterpart. However, the final drift is not a monotonic function of the orbit size. Thus, the minimum does not correspond neither to the largest nor smallest orbit of the family. It is also displayed that the spacecraft orientation, angular velocity and shape have sensible consequences on the orbital perturbation. In particular, highly anisotropic structures amplify the disturbance; conversely, it could be minimized, but not canceled, by adopting an axisymmetric mass distribution. These considerations draw a new picture of the dynamics in a multi-body gravitational environment, that might prove useful in the design of large spacecraft missions. Surprisingly, this picture reveals a fractal geometry of the response. The displacement

from the reference Lyapunov orbit seems to possess the proprieties named as auto-similarity and cross-similarity. The former means that the solution repeats itself on different scales as the time increase; the latter means that the same trend is observed on different scales depending on the spacecraft characteristic length. The auto-similarity confirms that it is sufficient to wait a certain time period to see the drift amplified to the point when the Lyapunov orbit is shortly left. Furthermore, thanks to the cross-similarity, this holds true regardless the spacecraft size, which acts only as an amplifying factor. Specifically, it is demonstrated that, within a certain maximum value, the final radial displacement is proportional to the square of the spacecraft characteristic length.

Recently, interest in the attitude dynamics in three-body gravitational field has risen as well. In this context, this work follows the path paved by the last papers published, which stress the importance of accounting a fully-nonlinear representation of the Lyapunov periodic orbits. Non-linearities in the orbital motion make the difference also in the attitude dynamics. As a matter of fact, the pitch response on nearly linear orbits is oscillatory and the amplitude of libration limited. The only circumstance leading to divergence of the pitch angle is the resonant condition. On the other hand, it is easy for a spacecraft to start spinning indefinitely along a truly nonlinear orbit. This behavior is mainly governed by the orbit size and the body inertia ratio. The investigation demonstrates that, when selecting the orbit size, the inertia ratio can be decreased to obtain bounded librations. Vice versa, given the inertia ratio, the orbit amplitude reduction achieves the same purpose. In the scenario of spacecrafts flying about the Lagrangian point, this result is a valuable understanding for the vehicle design and orbit selection.

8.2 Rigid Fully-Coupled Motion under Solar Radiation Pressure

The solar radiation pressure is the dominant environmental disturbance in the regions near the equilibrium points. Combined to the intrinsic instability of Lyapunov periodic orbits, it guarantees the departure from the nominal trajectory in few, perhaps not even one, revolutions. Nonetheless, a more thoughtful design of the reference orbit can totally or at least partially solve this issue. Including the solar radiation into the dynamical model, two strategies are proposed to address completely different scenarios: a spacecraft about the L_1 Sun-Earth point and another vehicle about

the L_1 Earth-Moon point. In the former, the orbit design is based on the solar sails theory. In the Sun-Earth system, a solar sail can fly along an artificial Lyapunov orbit that is simply displaced from the natural solution. Of course, this holds true under a precise set of assumptions. Not obviously, a standard solar-arrays-powered spacecraft can emulate the aforementioned dynamics of flat and perfectly reflective solar sails. Of course, some arrangements need to be considered. Among them, it is required to point toward the Sun. To this end, the solar arrays are tilted (they can be pictured as a V shape) in order to obtain a passive stabilization of the desired orientation. The robustness of the solution presented is verified varying the critical parameters of the system. Specifically, its validity is preserved even for fully anisotropic structures and reasonable inclinations of the solar arrays, in order to prevent critical reduction of the electric power supplied. During this investigation, it is also identified an abrupt variation of the gravity gradient torque along large periodic orbits, that will be referred as secondary anomaly because of its correlation with the vicinity to P_2. The secondary anomaly introduces a sudden and intense disturbance of the attitude motion.

A strategy not derived from any other previous theory is advanced in the Earth-Moon system to maintain a spacecraft orbiting around L_1. This approach starts with the extraction from the L_1 family of an orbit with period equal to one synodic month. For evident reasons, this orbit is rightfully named quasi sun-synchronous Lyapunov orbit. As second step, the spacecraft is assumed to constantly aim at the sun. Upon these conditions, an initial solar phase is discovered that guarantees extremely small errors of the periodic orbit at the crossing condition, despite the presence of the solar radiation pressure. This technique alone is not sufficient to preserve the nominal trajectory on the long period, but the attendant station keeping effort is surely reduced. Then, the robustness of the identified solution is verified for a satisfactorily wide range of the dominant system parameters. In other words, an adequate project flexibility is offered to the analyst. In conclusion, as in the earlier strategy, the natural fully-coupled dynamics under the solar radiation pressure are mastered to provide new helpful tools to design the future missions toward the libration points.

8.3 Dynamics of Flexible Configurations

The structure flexibility is incorporated in the dynamical formulation via the modal representation of the shape variations. Considering the pro-

prieties of standard spacecrafts, no visible alterations of the natural flight mechanics predicted with the rigid body model are observed. It is realized that the neighborhood of the equilibria corresponds to a general minimum of the environmental load on the structure; in turn, the deformations are not sufficiently large to practically interact with the translational and rotational dynamics. From the reverse perspective, it means that highly deformable architectures, not feasible near Earth, can instead withstand the solicitations in those regions. Hence, two elementary and highly flexible configurations are adopted to preliminarily understand the fully-coupled response, including the elastic dynamics. The analysis confirms that low levels of stiffness, well below the levels of classical structures, guarantee a rigid behavior in terms of orbital and attitude motion. Otherwise, if the configuration is deformable enough, the interplay of the dynamics emerges. Actually, only visible mutual interactions between the attitude and elastic components are reported. Conversely, the orbital path affects the elastic solution, but not vice versa. The first configuration investigated is a dumbbell satellite. Different results are reported and discussed. In particular, the elastic vibrations of the dumbbell seem to stabilize the spacecraft orientation. On small periodic orbits, the more the stiffness is decreased, the more the attitude oscillations are damped. Similarly, on large orbits, the pitch divergence of the equivalent rigid configuration can be limited by introducing a certain degree of flexibility. However, it also observed that, if the link is too weak, the dumbbell blows up (the distance between the tip masses grows quickly toward infinity). Secondly, a cross satellite is studied. Here, the system is sensitive to the extend that the major system parameters, such as the internal stiffness or the body inertia ratio, can alter the nature of the solution itself. Specifically, the effects of the secondary anomaly can be totally different: the spacecraft might increase its spin velocity, reverse the rotation direction as well as arrest its angular motion. In the latter circumstance, the secondary anomaly even triggers a critical transfer of energy from the attitude to the elastic dynamics. Each of the previous attitude responses is paired off with a specific elastic dynamics as well. Additionally, it is discovered that, on large Lyapunov orbits belonging to the L_2 family, the oscillations of the cross branches are able to stabilize the vehicle initial orientation; otherwise, the pitch angle along the trajectory would quickly depart from the initial condition. In conclusion, several mechanisms underlying the very elastic body dynamics are brought to light. Besides providing a deeper insight, with further studies they may serve as novel means to maneuver and control distributed architectures, in the broad sense of the term, including formation flights or multi-body systems with elastic joints.

8.4 Recommendations for Future Works

Given that the present thesis concerns many novel phenomena and presents a number of results addressed for the first time, any further in-depth analysis of those topics will be strongly encouraged. However, some directions deserve a greater consideration:

- *Investigate the spatial dynamics*. The current study is limited to the orbital plane of the two attractors. Besides the planar Lyapunov family, many other types of periodic or quasi periodic orbits exist in the out-of-plane regions. Furthermore, not only the fully spatial representation of the spacecraft attitude is mandatory for any practical purposes, but also the yaw and roll dynamics may reveal interesting behaviors in a multi-body gravitational field.

- *Develop a theoretical framework of the fractal response*. It has been shown that the orbital drift from the reference orbit induced by the gravity gradient may possess a fractal geometry. The quasi auto-similarity and quasi cross-similarity should be more rigorously confirmed by developing theoretical basis of the phenomenon and cogent demonstrations of these proprieties.

- *Systematic analysis of the rigid body attitude dynamics*. The orbit size and the inertia ratio proves to be the main governing parameters of the pitch dynamics. A threshold between bounded and unbounded solution has been partially delineated as a function of the aforementioned variables, but a refinement of that borderline would be recommended. It is also suggested to develop stronger theoretical basis of the phenomenon. Considering bounded solutions, would be also nice to seek for any sort of periodicity in attitude response. To this end, maps of the trajectories of the attitude states could be as useful as they are in the orbital dynamics.

- *Introduce an active Station Keeping*. So far, the strategies proposed to more easily keep the nominal trajectory under the solar radiation pressure are passively controlled. They are completely based on the natural dynamics. Especially in the solutions advanced in the Earth-Moon system, the introduction of an active station keeping policy is essential to maintain the orbit for a long period. In the event, standard actuators may be employed, otherwise the solar pressure itself might be exploited to generate the desired thrust. Finally, it is also suggested to compare the costs of novel and standard mission design.

- *Investigate the dynamics of more complex elastic configurations*. Two elementary architectures are addressed in this study. This paved the way to more sophisticated systems that can be a closer representation of the mission concept as well as can bring to light unexpected dynamical behaviors. In turn, a new manner to control and maneuvre the system might be founded on geometry mutations.

Symbols and Notations

Symbols	Meaning
α_b	Angle between the versor $\hat{b}_1$ and $\hat{\boldsymbol{s}}$.
α_i	Angle between the i-th surface normal $\hat{\boldsymbol{n}}_{\boldsymbol{i}}$ and the radiation incident direction.
β	Spacecraft lightness factor.
$\boldsymbol{\delta}$	Drift from the nominal trajectory.
$\delta r(t)$	Radial displacement at time t relative to the nominal trajectory.
δr_f	Final radial displacement relative to the nominal trajectory.
δ_{sa}	Solar arrays tilt.
ϵ_x	Position crossing error in terms of the coordinate along $\hat{\ell}_1$.
ϵ_{vx}	Velocity crossing error in terms of the coordinate along $\hat{\ell}_1$.
ϵ_{vy}	Velocity crossing error in terms of the coordinate along $\hat{\ell}_2$.
$\epsilon_{\theta_{sun}}$	Solar phase error after a period.
θ_{sun}	Solar phase.
θ_{SC}	Spacecraft angular position in the ℓ-frame.
μ	Mass parameter of the P_1-P_2 system.
μ_x	Gravitational planetary constant of the attractor P_x.

Continued on next page.

Continued from previous page.

Symbols	Meaning
ϕ	Spacecraft attitude angle in the orbital plane (also referred as pitch angle).
ξ_i	Modal damping of the i-th shape (subscript omitted in the event of a single mode).
$\Delta\theta$	Angular phase of the spacecraft relative to the Sun.
Δ_x	Position error after a period in terms of the coordinate along $\hat{\ell}_1$.
Δ_y	Position error after a period in terms of the coordinate along $\hat{\ell}_2$.
$\boldsymbol{\omega}$	Angular velocity vector of the ℓ-frame observed in the I-frame.
ω_0	Spacecraft initial angular velocity.
ω_{osc}	Angular frequency of the nominal Lyapunov orbit
$[\Phi(t_1, t_0)]$	State transition matrix between the initial time t_0 and the final time t_1.
Ω	Angular velocity of the P_1-P_2 system.
$\boldsymbol{a}_P^x$	Perturbation force due to the gravity gradient related to the attractor P_x.
b	Distance between the solar array center of pressure and the spacecraft center of mass for the I-SS and V-SS configurations.
b-frame	Local coordinate system to track the spacecraft position and orientation.
$(\hat{b}_1, \hat{b}_2, \hat{b}_3)$	tern of versor defining the b-frame.
$\boldsymbol{b}_i$	Position vector center of pressure of the i-th surface relative to the spacecraft center of mass.
k_3	Out-of-plane inertia ratio.
k_{crit}	Critical inertia ratio on quasi-linear Lyapunov periodic orbit.
k_i	Modal stiffness of the i-th shape (subscript omitted in the event of a single mode).
$\boldsymbol{l}_x$	cosine directors of $\boldsymbol{R}_x$ in the b-frame.
ℓ-frame	Global non-inertial coordinate system fixed on the Lagrangian point L_i.
$(\hat{\ell}_1, \hat{\ell}_2, \hat{\ell}_3)$	tern of versor defining the ℓ-frame.
m	Spacecraft total mass.

Continued on next page.

Continued from previous page.

Symbols	Meaning
$\hat{\boldsymbol{n}}_{\boldsymbol{i}}$	Normal of the i-th surface exposed to the solar radiation pressure.
$\boldsymbol{r_1}$	Location of P_3 relative to P_1.
$\boldsymbol{r_2}$	Location of P_3 relative to P_2.
$\boldsymbol{r}_P$	Position vector of the mass point P in the ℓ-frame.
$\boldsymbol{r}_x$	Location of the mass point P relative to the attractor P_x.
$\boldsymbol{q}$	Vector of generalized coordinates.
q_i	i-th generalized coordinates.
$\boldsymbol{q}_f$	Vector of elastic generalized coordinates.
$\boldsymbol{q}_r$	Vector of rigid generalized coordinates.
t	time variable.
$\hat{\boldsymbol{s}}$	Direction of the incident solar radiation.
$\boldsymbol{u}_0$	Position vector of the mass point P in the b-frame.
$\boldsymbol{u}_f$	Elastic displacement of the mass point P relative to the undeformed position in the b-frame.
$\boldsymbol{v}_T$	Velocity vector of a mass point P, fixed in the ℓ-frame, when observed from the I-frame.
$\boldsymbol{v}(O')$	Translational velocity vector of O'.
w	Spacecraft width.
x, y	Coordinates of the configuration space.
A	Total spacecraft cross-sectional area exposed to the solar radiation.
$[A]$	Rotation matrix from the b-frame to the ℓ-frame.
B	Origin of the b-frame.
$[C_{ff}]$	Modal damping matrix.
$\boldsymbol{F}_i^{SRP}$	Force exerted by the solar radiation pressure on the i-th surface.
$\mathcal{H}$	Hamiltonian function.
I	Spacecraft moment of inertia around the spin axis.
I-frame	Inertial coordinate system fixed on the center of mass of the P_1-P_2 system.
$(\hat{I}_1, \hat{I}_2, \hat{I}_3)$	tern of versor defining the I-frame.
I_{ii}	Moment of inertia about the i-th principal inertia axis.
L	Spacecraft length.
$[K]$	Stiffness matrix.

Continued on next page.

Continued from previous page.

Symbols	Meaning
JC	Jacobi constant.
$\mathcal{L}$	Lagrangian function.
$\mathcal{M}$	Poincaré map.
$[M]$	Mass matrix.
$\boldsymbol{M}_i^{SRP}$	Moment on the space center of mass exerted by the solar radiation pressure on the i-th surface.
O	Origin of the I-frame.
O'	Origin of the ℓ-frame.
P	Arbitrary mass point belonging to the spacecraft.
P_1	Primary attractor.
P_2	Secondary attractor.
P_3	Body representing the spacecraft.
P_x	Primary attractor for $x = 1$, secondary attractor for $x = 2$.
$\boldsymbol{Q}_\nu$	Quadratic velocity vector.
$\boldsymbol{Q}_\Omega$	Generalized action provoked by fictitious forces.
$\boldsymbol{Q}_g$	Generalized action provoked by the gravitational field.
$\boldsymbol{R}$	Position vector of B in the ℓ-frame.
$\boldsymbol{R}_0$	Position vector of B in the ℓ-frame along the reference trajectory.
$\boldsymbol{R}_x$	Location of B relative to the attractor P_x in the ℓ-frame.
$[S]$	Shape functions matrix.
T_{rel}	Kinetic relative energy observed in the ℓ-frame.
T_1	Generalized potential of the centrifugal force.
T_2	Generalized potential of the Coriolis force.
T_{osc}	Period of the nominal Lyapunov orbit.
U_x	Gravitational potential of the attractor P_x.

Ended from previous page.

List of Figures

List of Tables

Bibliography

[1] M. Balas. Trends in large space structure control theory: Fondest hopes, wildest dreams. *IEEE Transactions on Automatic Control*, ac-27:522–535, 1982.

[2] H. Poincaré. Sur les équations de la dynamique et le problème des trois corps. *Acta Math.*, 13:1–270, 1890.

[3] Philip Holmes. Poincare, celestial mechanics, dynamical-systems theory and chaos. *Physics Reports*, 3(3):137–163, 1990.

[4] S.H. Strogatz. *Nonlinear dynamics and chaos: With applications to physics, biology, chemistry, and engineering*. Westview Pr, 1994.

[5] J.A. Serret J.L. Lagrange. *Oeuvres de Lagrange*. Tome V, Gauthier-Villars, Imprimeur-Librarie, Paris, 1780.

[6] GN Duboshin. The differential equations of translational-rotational motion of mutally attracting rigid bodies. *Soviet Astronomy*, 2:239, 1958.

[7] J.P. Moran. Effects of plane librations on the orbital motion of a dumbbell satellite. *ARS Journal*, 31(8):1089–1096, 1961.

[8] D.B. Debra. *The large attitude motions and stability, due to gravity, of a satellite with passive damping in an orbit of arbitrary eccentricity about an oblate body*. Division of Engineering Mechanics, 1962.

[9] EY Yu. Long-term coupling effects between the librational and orbital motions of a satellite. *AIAA journal*, 2(3):553–555, 1964.

[10] S.N. Mohan. Orbital perturbations due to attitude libration of an arbitrary rigid body moving in a central newtonian field. Technical report, DTIC Document, 1970.

[11] S.N. Mohan, J.V. Lange, and B.O. Lange. Interaction between attitude libration and orbital motion of a rigid body in a near keplerian orbit of low eccentricity. *Celestial Mechanics and Dynamical Astronomy*, 5(2):157–173, 1972.

[12] GB Sincarsin and PC Hughes. Gravitational orbit-attitude coupling for very large spacecraft. *Celestial Mechanics and Dynamical Astronomy*, 31(2):143–161, 1983.

[13] B. Lange. Linear coupling between orbital and attitude motions of a rigid body. *Journal of the Astronautical Sciences*, 18:150, 1970.

[14] L. Meirovitch. On the effects of higher-order inertia integrals on the attitude stability of earth-pointing satellites. *Journal of the Astronautical Sciences*, 15:14, 1968.

[15] BE Schutz. The mutual potential and gravitational torques of two bodies to fourth order. *Celestial Mechanics and Dynamical Astronomy*, 24(2):173–181, 1981.

[16] VJ Modi, A Ng, A. Suleman, and Y. Morita. Dynamics of orbiting multibody system: A formulation with application. In *AIAA/ASME/ASCE/AHS/ASC Structures, Structural Dynamics, and Materials Conference, 32 nd, Baltimore, MD*, pages 2817–2830, 1991.

[17] AK Misra and VJ Modi. The influence of satellite flexibility on orbital motion. *Celestial Mechanics and Dynamical Astronomy*, 17(2):145–165, 1978.

[18] T.M. Wasfy and A.K. Noor. Computational strategies for flexible multibody systems. *Applied Mechanics Reviews*, 56:553, 2003.

[19] A.A. Shabana. Flexible multibody dynamics: review of past and recent developments. *Multibody system dynamics*, 1(2):189–222, 1997.

[20] W.W. Hooker and G. Margulies. The dynamical attitude equations for an n-body satellite(dynamical attitude equations for rotational motion of set of n rigid bodies interconnected by dissipative elastic joints and subjected to arbitrary forces and torques). *Journal of the Astronautical Sciences*, 12:123–128, 1965.

[21] JYL Ho. The direct path method for deriving the dynamic equations of motion of a multibody flexible spacecraft with topological tree configuration. In *AIAA Mechanics & Control of Flight Conference, Anaheim, Calif*, 1974.

[22] JYL Ho. Direct path method for flexible multibody spacecraft dynamics (originally schedulled for publication in the aiaa journal). *Journal of Spacecraft and Rockets*, 14:102, 1977.

[23] JYL Ho and DR Herber. Development of dynamics and control simulation of large flexible space systems. In *Guidance and Control Conference, San Diego, CA*, pages 367–378, 1982.

[24] W.W. Hooker. Equations of motion for interconnected rigid and elastic bodies: A derivation independent of angular momentum. *Celestial Mechanics and Dynamical Astronomy*, 11(3):337–359, 1975.

[25] P.W. Likins. Dynamic analysis of a system of hinge-connected rigid bodies with nonrigid appendages. *International Journal of Solids and Structures*, 9(12):1473–1487, 1973.

[26] PC Hughes. Dynamics of a chain of flexible bodies. *Journal of the Astronautical Sciences*, 27:359–380, 1979.

[27] W. Jerkovsky. The structure of multibody dynamics equations. *Journal of Guidance and Control, vol. 1, May-June 1978, p. 173-182.*, 1:173–182, 1978.

[28] VK Kumar and PM Bainum. Dynamics of a flexible body in orbit. In *AIAA, Astrodynamics Conference*, volume 1, 1978.

[29] R. A. Laskin, P. W. Likins, and R. W. Longman. Dynamical equations of a free-free beam subject to large overall motions (for flexible spacecraft). *American Astronautical Society and American Institute of Aeronautics and Astronautics, Astrodynamics Specialist Conference, Lake Tahoe, NV; United States; 3-5 Aug.1981*, page AAS 21, Aug 03 1981.

[30] JC Simo and L. Vu-Quoc. On the dynamics of flexible beams under large overall motions—the plane case: Part i. *Journal of Applied Mechanics*, 53:849, 1986.

[31] KW Lips and VJ Modi. Dynamics of spacecraft with deploying flexible appendages. In *In: Dynamics and control of large flexible spacecraft; Proceedings of the Second Symposium, Blacksburg, Va., June 21-23, 1979.(A80-31656 12-18) Blacksburg, Va., Virginia Polytechnic Institute and State University, 1979, p. 625-639. National Research Council of Canada*, volume 1, pages 625–639, 1979.

[32] KW Lips and VJ Modi. General dynamics of a large class of flexible satellite systems. *Acta Astronautica*, 7(12):1349–1360, 1980.

[33] L. Vu-Quoc and JC Simo. Dynamics of earth-orbiting flexible satellites with multibody components. *Journal of Guidance, Control, and Dynamics*, 10(6):549–558, 1987.

[34] JC Simo and L. Vu-Quoc. A three-dimensional finite-strain rod model. part ii: Computational aspects. *Computer methods in applied mechanics and engineering*, 58(1):79–116, 1986.

[35] J.C. Simo and L. Vu-Quoc. On the dynamics in space of rods undergoing large motions–a geometrically exact approach. *Computer methods in applied mechanics and engineering*, 66(2):125–161, 1988.

[36] L. Meirovitch. A new method of solution of the eigenvalue problem for gyroscopic systems(using state vectors). In *(National Congress of Applied Mechanics, 7 th, Boulder, Colo., June 3-7, 1974.) AIAA Journal,*, volume 12, pages 1337–1342, 1974.

[37] L. Meirovitch. A modal analysis for the response of linear gyroscopic systems. *Journal of Applied Mechanics*, 42:446, 1975.

[38] L. Meirovitch and AL Hale. Synthesis and dynamic characteristics of large structures with rotating substructures. In *Dynamics of Multibody Systems*, volume 1, pages 231–244, 1978.

[39] L. Meirovitch and RD Quinn. Equations of motion for maneuvering flexible spacecraft. *AIAA - J.Guidance*, 1987.

[40] VJ Modi. Attitude dynamics of satellites with flexible appendages- a brief review. In *AIAA 12 th Aerospace Sciences Meeting*, 1974.

[41] VJ Modi and AM Ibrahim. A general formulation for librational dynamics of spacecraft with deploying appendages. *Journal of Guidance, Control, and Dynamics(ISSN 0731-5090)*, 7:563–569, 1984.

[42] VJ Modi and AC Ng. Dynamics of interconnected flexible members in the presence of environmental forces: a formulation with applications. *Acta Astronautica*, 19(6-7):561–571, 1989.

[43] VJ Modi, AC Ng, and F. Karray. A general formulation for the nonlinear dynamics and control of orbiting flexible structures. *Computational mechanics*, 13(3):204–230, 1993.

[44] TR Kane. Partial rates of change of position and of orientation. *Bulletin of Mechanical Engineering Education*, 2:17, 1960.

[45] TR Kane. Dynamics of nonholonomic systems. *Journal of Applied Mechanics*, 28:574, 1961.

[46] TR Kane and CF Wang. On the derivation of equations of motion. *Journal of the Society for Industrial and Applied Mathematics*, 13(2):487–492, 1965.

[47] T.R. Kane and D.A. Levinson. Formulation of equations of motion for complex spacecraft. *Journal of Guidance and Control, vol. 3, Mar.-Apr. 1980, p. 99-112. Research supported by the Lockheed Missiles and Space Independent Research Program*, 3:99–112, 1980.

[48] A.K. BANERJEE. Contributions of multibody dynamics to space flight: a brief review. *Journal of guidance, control, and dynamics*, 26(3):385–394, 2003.

[49] RP Singh, RJ VanderVoort, and PW Likins. Dynamics of flexible bodies in tree topology- a computer oriented approach. In *Structures, Structural Dynamics and Materials Conference, 25 th, Palm Springs, CA*, pages 327–337, 1984.

[50] T.R. Kane and E.L. Marsh. Attitude stability of a symmetric satellite at the equilibrium points in the restricted three-body problem. *Celestial Mechanics*, 4:78–90, 1971.

[51] W.J. Robinson. The restricted problem of three bodies with rigid dumb-bell satellite. *Celestial Mechanics*, 8:323–330, 1973.

[52] W.J. Robinson. Attitude stability of a rigid body placed at an equilibrium point in the restricted problem of three bodies. *Celestial Mechanics*, 10:17–33, 1974.

[53] I.V. Barkin. Motion of a spacecraft about its center of mass when the latter is located at a libration point of the earth-moon system. *Kosmicheskie Issledovaniia*, 18:191–206, 1980.

[54] A. Abad, M. Arribas, and A. Elipe. On the attitude of a spacecraft near a lagrangian point. *House of the Czechoslovak Academy of Sciences*, 40(1988), 1989.

[55] Eytan Brucker and Pini Gurfil. Analysis of gravity-gradient- perturbed rotational dynamics at the collinear lagrange points. *The Journal of the Astronautical Sciences*, 55(3):271–291, 2007.

[56] B. Wong, R. Patil, and A. Misra. Attitude dynamics of rigid bodies in the vicinity of lagrangian points. *Journal of guidance, control, and dynamics*, 31(1):252–256, 2008.

[57] A.J. Knutson and K.C. Howell. Application of kane's method to incorporate attitude dynamics into the circular restricted three body problem. In *22nd AAS/AIAA Space Flight Mechanics Meeting*, 2012.

[58] H. Curtis. *Orbital mechanics for engineering students*. A Butterworth-Heinemann Title, 2009.

[59] A.E. Roy. *Orbital motion*. Taylor & Francis, 2004.

[60] W.S. Koon, M.W. Lo, J.E. Marsden, and S.D. Ross. *Dynamical systems, the three-body problem and space mission design*. World Scientific, 2006.

[61] V. Szebehely. Theory of orbits: the restricted problem of three bodies. Technical report, DTIC Document, 1967.

[62] K.C. Howell et al. Families of orbits in the vicinity of the collinear libration points. *Journal of the Astronautical Sciences*, 49(1):107–126, 2001.

[63] D.L. Richardson. Analytic construction of periodic orbits about the collinear points. *Celestial Mechanics and Dynamical Astronomy*, 22(3):241–253, 1980.

[64] K. Connor Howell. Three-dimensional, periodic,'halo'orbits. *Celestial Mechanics and Dynamical Astronomy*, 32(1):53–71, 1984.

[65] M. Canistro. Il problema dei tre corpi ristretto: connessioni delle varietà invarianti per trasferimenti interplanetari a basso costo. Master's thesis, Politecnico di Milano, 2005/2006.

[66] AA Shabana. Finite element incremental approach and exact rigid body inertia. *Journal of Mechanical Design*, 118:171, 1996.

[67] A.A. Shabana. *Dynamics of multibody systems*. Cambridge Univ Pr, 2005.

[68] P Nikravesh. Understanding mean-axis conditions as floating reference frames. *Advances in computational multibody systems*, pages 185–203, 2005.

[69] A.A. Shabana and R.A. Wehage. A coordinate reduction technique for dynamic analysis of spatial substructures with large angular rotations. *Journal of Structural Mechanics*, 11(3):401–431, 1983.

[70] JC Simo. A finite strain beam formulation. the three-dimensional dynamic problem. part i. *Computer methods in applied mechanics and engineering*, 49:55–70, 1985.

[71] M. Geradin, A. Cardona, DB Doan, and J. Duysens. Finite element modeling concepts in multibody dynamics. *Computer-aided analysis of rigid and flexible mechanical systems*, pages 233–284, 1994.

[72] AA Shabana. An absolute nodal coordinate formulation for the large rotation and deformation analysis of flexible bodies. *Report, Mechanical Engineering, University of Illinois at Chicago*, 1996.

[73] JL Escalona, HA Hussien, and AA Shabana. Application of the absolute nodal coordinate formulation to multibody system dynamics. Technical report, DTIC Document, 1997.

[74] H. Schaub and J.L. Junkins. *Analytical mechanics of space systems*, volume 1, chapter 11. Aiaa, 2003.

[75] J.R. Wertz and W.J. Larson. *Space mission analysis and design*, volume 8, chapter 6. Kluwer Academic Publishers, 1999.

[76] A.I.S. McInnes. *Strategies for solar sail mission design in the circular restricted three-body problem*. PhD thesis, Purdue University, 2000.

[77] C.R. McInnes, A.J. McDonald, J.F.L. Simmons, and E.W. MacDonald. Solar sail parking in restricted three-body systems. *Journal of Guidance Control Dynamics*, 17:399–406, 1994.

[78] A. Farrés and À. Jorba. Periodic and quasi-periodic motions of a solar sail close to sl 1 in the earth–sun system. *Celestial Mechanics and Dynamical Astronomy*, 107(1):233–253, 2010.

[79] CR MCINNES. Passive control of displaced solar sail orbits. *Journal of guidance, control, and dynamics*, 21(6):975–982, 1998.

[80] S. Gong, J. Li, and H. Baoyin. Passive stability design for the solar sail on displaced orbits. *Journal of Spacecraft and Rockets*, 44:1071–1080, 2007.

[81] SN Kirpichnikov, ES Kirpichnikova, EN Polyakhova, and AS Shmyrov. Planar heliocentric roto-translatory motion of a spacecraft with a solar sail of complex shape. *Celestial Mechanics and Dynamical Astronomy*, 63(3):255–269, 1995.

[82] J. Simo and C.R. McInnes. Solar sail orbits at the earth-moon libration points. *Communications in Nonlinear Science and Numerical Simulation*, 14(12):4191–4196, 2009.

[83] AA SHABANA, HA HUSSIEN, and JL ESCALONA. Application of the absolute nodal coordinate formulation to large rotation and large deformation problems. *Journal of mechanical design*, 120(2):188–195, 1998.

[84] M. Martinez-Sanchez and S.A. Gavit. Orbital modifications using forced tether-length variations. *Journal of Guidance Control Dynamics*, 10:233–241, 1987.

[85] G.A. Landis. Reactionless orbital propulsion using tether deployment. *Acta Astronautica*, 26(5):307–312, 1992.

[86] C. Rui, I.V. Kolmanovsky, and N.H. McClamroch. Nonlinear attitude and shape control of spacecraft with articulated appendages and reaction wheels. *Automatic Control, IEEE Transactions on*, 45(8):1455–1469, 2000.

[87] A.K. Sanyal, J. Shen, and N.H. McClamroch. Control of a dumbbell spacecraft using attitude and shape control inputs only. In *American Control Conference, 2004. Proceedings of the 2004*, volume 2, pages 1014–1018. IEEE, 2004.

[88] D.A. Quinn and D.C. Folta. A tethered formation flying concept for the specs mission. In *Guidance and control 2000: proceedings of the annual AAS Rocky Mountain Guidance and Control Conference held February 2-6, 2000, Breckenridge, Colorado*, volume 104, page 183. American Astronautical Society, 2000.

[89] M. Kim and C.D. Hall. Dynamics and control of tethered satellite systems for nasas specs mission. *Advances in the Astronautical Sciences*, 116:489–508, 2003.

[90] M. Sanjurjo-Rivo, F.R. Lucas, J. Peláez, C. Bombardelli, E.C. Lorenzini, D. Curreli, D.J. Scheeres, and M. Lara. On the dynamics of a tethered system near the collinear libration points. In *Astrodynamics Specialist Conference, 18-21 August 2008, Honolulu, Hawaii, USA*, pages 2008–7380. American Astronautical Society, 2008.

[91] W. Traub, S. Shaklan, and P. Lawson. Terrestrial planet finder. *University of California-Berkeley*, 4:8, 2007.

[92] M.J. Patterson, S.W. Benson, and NASA Glenn Research Center. Next ion propulsion system development status and capabilities. Technical report, National Aeronautics and Space Administration, Glenn Research Center, 2008.

[93] J.M. Hedgepeth. Critical requirements for the design of large space structures. Technical report, NASA, 1981.